Ultra-wideband Channel Estimation with Application towards Time-of-Arrival Estimation

by

Ted C.-K. Liu

B.A.Sc., Simon Fraser University, 2006

Dip., British Columbia Institute of Technology, 2001

A Dissertation Submitted in Partial Fulfillment of the

Requirements for the Degree of

MASTER OF APPLIED SCIENCE

in the Department of Electrical and Computer Engineering

Ultra-wideband Channel Estimation with Application towards Time-of-Arrival Estimation

by

Ted C.-K. Liu

B.A.Sc., Simon Fraser University, 2006

Dip., British Columbia Institute of Technology, 2001

Supervisory Committee

Dr. Xiaodai Dong, Supervisor

(Department of Electrical and Computer Engineering)

Dr. Wu-Sheng Lu, Departmental Member

(Department of Electrical and Computer Engineering)

Supervisory Committee

Dr. Xiaodai Dong, Supervisor
(Department of Electrical and Computer Engineering)

Dr. Wu-Sheng Lu, Departmental Member
(Department of Electrical and Computer Engineering)

ABSTRACT

Ultra-wideband (UWB) technology is the next viable solution for applications in wireless personal area network (WPAN), body area network (BAN) and wireless sensor network (WSN). However, as application evolves toward a more realistic situation, wideband channel characteristics such as pulse distortion must be accounted for in channel modeling. Furthermore, application-oriented services such as ranging and localization demand fast prototyping, real-time processing of measured data, and good low signal-to-noise ratio (SNR) performance. Despite the tremendous effort being vested in devising new receivers by the global research community, channel-estimating Rake receiver is still one of the most promising receivers that can offer superior performance to the suboptimal counterparts. However, acquiring Nyquist-rate samples costs substantial power and resource consumption and is a major obstacle to the feasible implementation of the asymptotic maximum likelihood (ML) channel estimator.

In this thesis, we address all three aspects of the UWB impulse radio (UWB-IR), in three separate contributions. First, we study the *a priori* dependency of the CLEAN deconvolution with real-world measurements, and propose a high-resolution,

multi-template deconvolution algorithm to enhance the channel estimation accuracy. This algorithm is shown to supersede its predecessors in terms of accuracy, energy capture and computational speed. Secondly, we propose a *regularized* least squares time-of-arrival (ToA) estimator with wavelet denoising to the problem of ranging and localization with UWB-IR. We devise a threshold selection framework based on the Neyman-Pearson (NP) criterion, and show the robustness of our algorithm by comparing with other ToA algorithms in both computer simulation and ranging measurements when advanced digital signal processing (DSP) is available. Finally, we propose a low-complexity ML (LC-ML) channel estimator to fully exploit the multipath diversity with Rake receiver with sub-Nyquist rate sampling. We derive the Cramér-Rao Lower Bound (CRLB) for the LC-ML, and perform simulation to compare our estimator with both the ℓ_1-norm minimization technique and the conventional ML estimator.

Contents

List of Tables

List of Figures

List of Abbreviations

FCC	Federal Communications Committee
UWB(-IR)	ultra-wideband (impulse radio)
IEEE	Institute of Electrical and Electronics Engineers
DSP	digital signal processing
WPAN	wireless personal area network
BAN	body area network
WSN	wireless sensor network
TX/RX	transmitter/receiver
DSO	digital sampling oscilloscope
CIR	channel impulse response
SNR	signal-to-noise ratio
TN/RN	target node/reference node
ToA	time-of-arrival
MPC('s)	multipath component(s)
DP	direct path
ED	energy detector
MRC	maximum ratio combining
CSI	channel state information
(LC-)ML(E)	(low-complexity) maximum likelihood (estimator)

DA	data-aided
MIMO	multiple-input and multiple-output
(R)LS	(regularized) least squares
NP	Neyman-Pearson
CRLB	Cramér-Rao Lower Bound
FIR	finite impulse response
(N)LOS	(non)-line-of-sight
(R)MSE	(root) mean-squared error
Ao(A/E)	angle-of-(arrival/elevation)
MF	matched filter
AWGN	additive white Gaussian noise
PSD	power spectral density
PDB	peak-detection-based algorithm
CS	compressed sensing
MP	matching pursuit
A-PAM	antipodal pulse amplitude modulation
LNA	low-noise amplifier
WSS	wide-sense stationary
GPIB	General Purpose Interface Bus
WD	wavelet denoising
DWT	discrete-time wavelet transform
CFA	constant false alarm
i.i.d.	independent and identically distributed
p.d.f.	probability density function
c.d.f.	cumulative distribution function
BER	bit error rate

ACKNOWLEDGEMENTS

First and foremost, I would like to express my deepest gratitude to my supervisor Dr. Xiaodai Dong. This thesis would not have been possible without her strong enthusiasm, constant motivation, invaluable guidance, and ample support. I would like to express my sincere gratitude to my committee member Prof. Wu-Sheng Lu for his insightful guidance and constructive comments, and to Dr. Jianping Pan for being as the external examiner.

Besides the committee members from UVic, I would like to express my gratitude for Prof. Dong In Kim of Sungkyunkwan University and Prof. Rodney Vaughan of Simon Fraser University. The first contribution of this thesis would have been impossible without their guidance and support. Furthermore, the work of this thesis was made possible by the generous financial support from NSERC.

I would like to thank both my colleagues and staffs from UVic and SFU. From UVic, thanks go to Zhonghua, Shuai, Yuzhe, Ruonan, and Lebing for giving me an opportunity to witness how to conduct research the Chinese style. From SFU, thanks go to Maryam, Rob, Serhat, Naeem, and Wanjong.

Besides my colleagues, I would like to thank friends from Vancouver and abroad, Farhan, Daniel, Salman, Nima, Claude and his brother Jack. The people from VCCEF have also played a pivotal role in supporting me spiritually. Thank you Robin, Joyce, Dan, Adam, Carson, Joshua and Ling for quenching and refreshing my soul every Friday night.

Most importantly, this work would not have been possible without my parents and my brother Gary. Thank you all for being there when I was in need. Without your love, patience, encouragement, understanding and care, I would not have been where I am today.

DEDICATION

To my dearest parents

Chapter 1

Introduction

The groundbreaking *unlicensed* spectrum allocation mandate put forth by the United States (U.S.) Federal Communications Committee (FCC) in 2002 [1] has spawned an exponential growth in ultra-wideband (UWB) technology research. Conceptually, UWB is characterized by a transmission with an instantaneous spectrum in excess of 500 MHz, or a fractional bandwidth[1] (BW) of more than 20%. The ideal of periodically sending ultra-short duration pulses is nothing new and can be dated back to 1887 when Hertz experimented with the spark gap, which was later incorporated into the telegraph by Guglielmo Marconi [2, 3]. However, when deployed in a communications context, UWB technology with its ultra-wide BW, i.e., the 3.1–10.6 GHz FCC spectrum allocation [1, 2], can enable many attractive features [2–6] which conventional narrowband would otherwise fail to provide, features such as:

- fine time resolution. The timing resolution is inversely proportional to the signal BW, so the tremendous BW offered by UWB means extremely fine time resolution;

[1] The fractional bandwidth is defined as B/f_c [1, 2], where $B := f_H - f_L$ is the -10 dB bandwidth, $f_c := (f_H + f_L)/2$ is the center frequency, and f_H and f_L are the upper and lower -10 dB frequencies, respectively.

- resistance to multipath fading. The transmission of ultra-short duration pulses lessens the possibility of pulses overlapping and canceling, thus improves the overall wireless link reliability by enriching the channel with multipath diversity;

- resistance to jamming and interference. The ultra-wide BW and low power emission incapacitate the capacity of the interferer and allows covert communication since there will always be a portion of the spectrum unaffected by jamming and interference;

- easier material penetration. The possibility of the entire pulse spectrum been attenuated due to the presence of objects is greatly reduced due to the frequency-selective nature of the electromagnetic propagation mechanisms.

Furthermore, the classical UWB impulse radio (IR), i.e., transmission by sending ultra-short duration pulses, can ease the cost of implementation since it does not require the expensive up/down conversion, typically an integral part of the narrowband modulation/demodulation stage. Altogether, these unique features, coupled with the eminent advancement in both digital signal processing (DSP) and communications, has spawned many potential applications for UWB, such as:

- short-range (< 10 m) communications with extremely high data rates, e.g., communication in a wireless personal area network (WPAN) and/or body area network (BAN);

- wireless sensor network (WSN), where low rate communications are combined with precise ranging and geolocation [7];

- radar systems, with the extremely high spatial resolution and obstacle penetration capabilities.

1.1 Motivation

As more efforts are put forth in the design of UWB-specific applications, more work also needs to be concentrated on the selection of the design parameters, such as pulse shaping, transmitter/receiver (TX/RX) design, multiple-access technique, and antenna selection, all of which are influenced by the wireless propagation channel. The IEEE 802.15.3a channel model [8] (and the latest IEEE 802.15.4a version [9]) devised recently for UWB models the multipath channel as a tapped-delay-line such that the received signal would simply be comprised of delayed and scaled replicas of a pulse template. However, this model is too optimistic since it ignores the pronounced frequency-dependent pulse distortion [6, 10–12] that arises owing to the ultra-wide spectral support of the transmitting pulse. Hence, new channel characterization must be conducted to ensure that the future channel model can account for the realistic propagation behaviors of a true wideband channel. One of the most popular channel characterization method is via the time-domain technique [13] in which the channel is measured with a digital sampling oscilloscope (DSO). Depending on the desired resolution, the channel impulse response (CIR) can be extracted from the received signal by high-resolution algorithms [6], such as the CLEAN algorithm [14].

The result of a good channel model can facilitate accurate performance analysis and system design on potential UWB applications. One application particularly of interest is in ranging and localization applications, which the impulsive UWB system can enable centimeter accuracy with a minimum cost on the signal-to-noise ratio (SNR) [7]. High precision localization is a desirable feature in emergency applications such as search and rescue operations, and non-emergency applications in logistics, inventory and personnel tracking in both public and private sectors [3, 7, 15]. However, when locating many items in a system of interconnected networks, e.g., estimating the unknown positions of the many target nodes (TN's) in a WSN with a few ref-

erence nodes (RN's) of known positions [16], the complexity of both the localization and ranging algorithms must be minimized to foster real-time operation. Depending on the network topology and given a set of range measurements, the localization algorithm must pinpoint the location of the TN in a timely manner. Since the data processing cannot begin until all of the measurements are collected, rapid localization *hinges* on minimizing the amount of measurement time. Taking advantage of its wide spectral support, range estimates derived from time-of-arrival (ToA) measurements is the most suitable approach in UWB-based positioning system. Unfortunately, many existing UWB ranging algorithms are either highly complex [17, 18], or do not perform well in low SNR [19], even if means of advanced DSP are available [20]. Therefore, part of the ongoing research in UWB ranging is to devise low-complexity algorithm that is capable of online operation, and to demonstrate the feasibility of the algorithm in a real-world application.

Apart from re-examining the validity of the existing channel model or devising a new low-complexity ranging scheme, the ultimate target application of the UWB technology is in communications [2–4]. Although the ultra-wide spectrum of impulsive UWB can enable many attractive features as aforementioned, deploying UWB-IR in a communications context is quite challenging. Particularly troublesome is the dispersion of the transmitted energy due to multipath propagation, c.f., Fig. 1.1, an effect which is more pronounced as the overall system BW is increased [2–5, 13, 21]. Due to the energy dispersion, a robust receiver that is capable of collecting the rich multipath must be designed to mitigate performance degradation. Ideally, the Rake receiver [22] which has been widely adopted in spread spectrum systems can be used to collect the multipath components (MPC's). However, a Rake receiver relies on the maximum ratio combining (MRC) of accurate channel state information (CSI) to produce reliable decision statistics. Therefore, it is important to devise an accurate

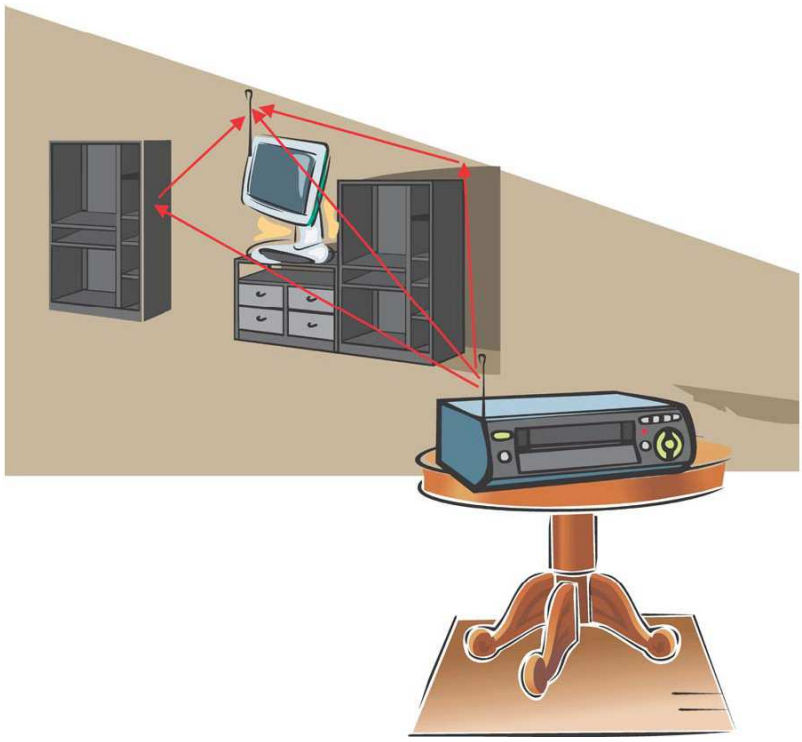

(a) Rich multipath diversity [6]

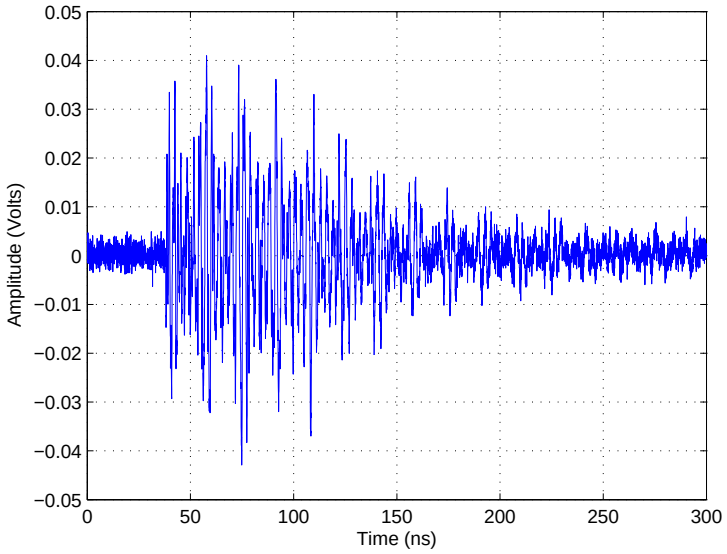

(b) A typical received signal for UWB-IR [5]

Figure 1.1: The rich multipath diversity and its impact on the received signal for UWB-IR.

channel estimator. For that, Win and Scholtz, and Lottici *et al.* proposed a maximum likelihood (ML) channel estimator for an isolated pulse and data-aided (DA) pilot symbol transmission in [5] and [23], respectively. Unfortunately, both require operating at the formidable Nyquist sampling frequency. Since then, many other variants of the estimator [24–27] and new receiver types [28–31] have been proposed to reduce the complexity. Suboptimal receivers such as energy detectors and autocorrelation receivers generally take a power penalty to achieve similar performance to the coherent counterpart [32]. Recently, there has been a renewed interest in the use of Rake receivers for UWB applications, e.g., multiple-input and multiple-output (MIMO) systems [33], BAN [34] and cooperative BAN [35], and prerake systems [30]. In addition, the use of accurate CSI, e.g., multipath delay (and amplitude) estimates, is also indispensable for precision asset localization and tracking with UWB-IR [7, 36]. As shown in [36], when delays of the MPC's are known *a priori*, accurate channel estimates can greatly improve the performance of the ToA positioning algorithm. In essence, the design or enhancement of accurate channel estimator must not be overlooked for impulsive UWB technology.

1.2 Contributions

The contributions of this thesis are three-fold.

First of all, we summarize the use of the CLEAN algorithm in UWB channel characterization, including a discussion on the *a priori* assumption, enhancements made to the basic algorithm, and the effect of the *a priori* assumption has on the perceived channel characteristics. We then study the *a priori* dependence with real-world measurements to demonstrate the shortcomings of the single-template CLEAN. Finally, we propose a high-resolution, multi-template deconvolution algorithm to enhance

the channel estimator performance. This algorithm incorporates realistic frequency-dependent pulse distortions, and we compare our algorithm to its predecessors in terms of accuracy, energy capture and computational speed.

Secondly, to improve ranging accuracy when localizing with UWB-IR, we propose a *regularized* least squares (RLS) approach with wavelet denoising to improve the estimator accuracy at low SNR. Our approach estimates the ToA as a by-product of the RLS channel estimation based on a thresholding technique, which is simple and can enable online processing applicable to real-time application. In addition to the meticulous selection of a threshold based on the Neyman-Pearson (NP) criterion, we demonstrate the robustness of our algorithm by comparing with the existing algorithms in computer simulation when advanced DSP is available, then applying the algorithms to a realistic situation of range estimation via the UWB-IR.

Thirdly, to fully exploit the multipath diversity with channel estimating Rake receiver without acquiring the formidable Nyquist-rate samples, we propose a low-complexity ML (LC-ML) channel estimator which combines the compression framework of compressed sensing for sampling rate reduction while retaining the noise statistics formulation of ML to achieve a reliable performance. Compressed sensing is an emerging theory that outlines a novel strategy to jointly compress and detect a sparse signal with fewer sampling resources than the traditional Nyquist sampling. On top of deriving the Cramér-Rao Lower Bound (CRLB) for the LC-ML, we perform simulation to compare our estimator with the conventional ML estimator and the ℓ_1-norm minimization technique typically used in compressed sensing.

We would like to stress that although the contributions do not abide by the latest IEEE 802.15.4a standard [37], they are novel in ways such that we have either improved upon and/or extended the work of recent literatures. Ultimately, these improvements can be incorporated as a part of the existing standard if needed.

1.3 Thesis Outline

The rest of this thesis is organized as follows:

Chapter 2 provides background information and literature reviews. Specifically, it first introduces UWB channel characterization via deconvolution techniques. Then, it discusses ToA estimation with UWB-IR, including the CRLB on ranging and the fusion of data for positioning. Finally, channel estimation with UWB-IR is discussed together with the use of CSI in MRC Rake receiver.

Chapter 3 studies the *a priori* dependence with real-world measurements to demonstrate the limitations of the CLEAN algorithm. Thereafter, we propose a high-resolution, multi-template deconvolution algorithm that incorporates realistic frequency-dependent pulse distortions. We compare our algorithm to its predecessors in terms of accuracy, energy capture and computational speed.

Chapter 4 proposes the RLS ToA estimator with wavelet denoising, including the system model, wavelet denoising and an outline of the threshold selection strategy based on the NP criterion. This chapter then illustrates the robustness of our estimator in two respects: first comparing with the existing high-resolution ToA algorithms in computer simulation, then comparing all of the algorithms in a realistic situation of range estimation via the UWB-IR.

Chapter 5 proposes the LC-ML channel estimator, including the system model, the derivation of the LC-ML estimator, the derivation of the CRLB, and a discussion on the implementation issues. Then, we validate the derived CRLB by numerical example, and compare the LC-ML with the ℓ_1-norm minimization estimator and the conventional ML estimator in system performance.

Chapter 6 concludes the thesis and suggests possible future work.

Chapter 2

Background and Related Work

In this chapter, we provide background information and literature reviews for the thesis. Section 2.1 introduces UWB channel characterization via deconvolution techniques by discussing the *a priori* assumption, enhancements made to the basic algorithm, possible pulse distortion and its implication on the algorithm. Section 2.2 discusses ToA estimation with UWB-IR, including the CRLB on ranging and the fusion of data for positioning. Finally, Section 2.3 discusses channel estimation with UWB-IR together with the use of CSI in MRC Rake receiver.

2.1 Channel Characterization via Deconvolution Techniques

UWB-IR technology has attracted tremendous attention among the global communications research community [2, 6]. With the potential for high data rate, multiple access capacity, high resistance to multipath, low probability of detection and interception, and material penetration, it is a candidate for many commercial and military applications, such as short-range high-speed wireless communications, covert network-

ing, precision asset localization, ground-penetrating radar, and through-wall imaging [2].

Before the final selection of UWB design parameters, such as pulse shaping, multiple-access techniques, and antenna designs, the channel behavior must be understood through channel characterization. In general, there are three basic techniques to characterize the channel [13], namely: time-domain, frequency-domain, and with sliding correlator. Although the time-domain technique has a limited dynamic range and is challenging in high-energy impulse generation, measurement signal triggering, and sensitive to impulsive and narrowband interference [6], its simplicity, together with versatility and high-resolution capability makes it one of the most widely used characterization techniques. To date, there have been many measurement campaigns with time-domain ultra-wide BW impulse sounding technique, e.g., [5, 12, 21, 35, 38–42]. In these, the goal is to analyze and understand the ultra-wide BW channel, and to propose potentially new UWB communications techniques and applications. With a proper measurement apparatus setup, it can be straightforward to obtain both the large-scale and small-scale channel parameters, e.g., the path loss and delay spread, respectively. However, if high-resolution channel modeling is required, a deconvolution algorithm, such as the CLEAN algorithm [14], must be used to obtain the details of CIR.

The CLEAN deconvolution algorithm was first used to enhance the radio astronomical imaging of the sky. Since then, it has been widely used in both narrowband [14] and UWB [21, 38–46] communications, in faulty cable detection with UWB pulses [47], UWB biomedical imaging [48] and BAN applications [35]. The algorithm processes data by serially canceling (i.e., cleans) the similarity between a dirty map, e.g., the measurement, and the *a priori* information, e.g., the template, and reconstructs the clean map (i.e., CIR) based on these detected similarities [14]. However, CLEAN

inherently assumes the channel to be non-dispersive, i.e., there is no pulse distortion, so the resultant CIR is simply a summation of amplitude-scaled and time-shifted versions of the *a priori* information. For time-domain UWB channel sounding, this assumption must be carefully considered when it involves probing the channel with sub-nanosecond impulses.

2.1.1 The CLEAN Deconvolution Algorithm

Basic Algorithm

The CLEAN algorithm is an iterative, high-resolution, subtractive deconvolution procedure that is capable of resolving dense MPC's which are usually unresolvable by conventional inverse filtering [6]. However, it circumvents any path dependent pulse distortion by assuming the received signal is simply a summation of delayed and scaled versions of the *a priori* information, usually taken from a line-of-sight (LOS) reference measurement, as [6, 14]

$$y(\tau) \approx h(\tau) \otimes p(\tau) = \sum_{i=1}^{N} \alpha_i p(\tau - \tau_i)\,, \tag{2.1}$$

where $h(\tau) := \sum_{i=1}^{N} \delta(\tau - \tau_i)$ is the CIR, $p(\tau)$ is the received pulse shape which is known *a priori*, $\otimes$ is the convolution operation, $\delta(\cdot)$ is the Dirac-Delta function, N is the number of MPC's, α_i and τ_i are the amplitudes and relative delays of the i-th MPC, respectively, and we have ignored the effect of noise in (2.1). This assumption must be revised if the CIR is to contain path-dependent distortion. The dominant feature of CLEAN is that it models the estimated CIR $\hat{h}(\tau)$ as a discrete finite impulse response (FIR) filter, which can then be easily used to characterize and model delay spread, path loss, Rake energy capture, and the propagation channel, as in [38, 41].

The basic algorithm to process narrowband channel was first introduced in [14]

from image processing to estimate the details of the ToA. As shown in Table 2.1, this implementation involves the computation of the correlation coefficient function, and the removal and the reconstruction of detected similarity on both the dirty and the clean maps, respectively, for each iteration.

1.	initialize the dirty map $d_0(t)$ with the received waveform $y(t)$ as $d_0(t) = y(t)$ and the clean map with $c_0(t) = 0$;
2.	form the normalized cross-correlation functions $R_{dp}(\tau) = d_n(t) \odot p(t)$ ($\odot$ denotes correlation);
3.	compute $\hat{\tau}_n = \arg\max_\tau \lvert R_{dp}(\tau) \rvert$ and $\hat{\alpha}_n = R_{dp}(\hat{\tau}_n)$;
4.	if $\hat{\alpha}_n <$ threshold, go to step 8;
5.	clean the dirty map by $d_n(\tau) = d_{n-1}(\tau) - \hat{\alpha}_n p(\tau - \hat{\tau}_n)$;
6.	update the clean map as $c_n(\tau) = c_{n-1}(\tau) + \hat{\alpha}_n p(\tau - \hat{\tau}_n)$;
7.	go to step 2;
8.	the impulse response is then $\hat{h}(t) = c_n(t)$.

Table 2.1: Basic CLEAN deconvolution algorithm.

This approach for narrowband signal assumes that, since the signal BW is relatively small, the variation of the pulse distortion would be small. For UWB communications, a variant of the basic CLEAN was first introduced in [21], and has since been widely adopted on many of the subsequent works in channel characterization and modeling [38–46]. In [45], it was used to propose a scattering model for the propagation channel. However, the channel was measured in the frequency-domain, and the *a priori* was an ideal Gaussian doublet of 2–4 GHz BW with the assumption that it would experience the same channel as that derived from frequency chirp sounding.

Algorithm Enhancements

The first major enhancement of CLEAN was proposed by [43]. This modification, called Sensor-CLEAN, processes measurements with a minimum of *a priori* information, except the received signal comprises of impulse-type waveforms, and that they

have a finite time support. The main advantage of Sensor-CLEAN is its ability to estimate the ToA, as well as angle-of-arrival (AoA). Unfortunately, it requires an array of measurements to produce the beamformer output, and is much more complicated to implement than the basic CLEAN. The Sensor-CLEAN was further modified in [44] to include polarization estimation of each resolvable MPC from the received signal. Similarly to Sensor-CLEAN, this modification requires an extensive array measurements, including a set of 3-D array measurements per antenna orientation.

In [14], both the dirty and the clean maps are processed with an amplitude scaled and delayed version of the *a priori*. Furthermore, the cross-correlation between the dirty map and the *a priori* is formed on each iteration. To speed up this process, [38] computes the cross-correlation in the initialization, and cleans the dirty map with autocorrelation of the *a priori* as in Table 2.2. Although computation speed is seldom a major issue in channel characterization and testing, this enhancement has been used on many of the subsequent UWB channel characterization, such as [40, 41], and faulty cable detection with UWB in [47], to name just a few.

1.	initialize normalized cross-correlation between $y(t)$ and $p(t)$, and normalized autocorrelation of $p(t)$ as $R_{yp}(\tau) = y(t) \odot p(t)$ and $R_{pp}(\tau)$, respectively, and define the dirty and clean map as $d_0(\tau) = R_{yp}(\tau)$ and $c_0(\tau) = 0$;
2.	compute $\hat{\tau}_n = \arg\max_\tau \lvert R_{yp}(\tau) \rvert$ and $\hat{\alpha}_n = R_{yp}(\hat{\tau}_n)$;
3.	if $\hat{\alpha}_n <$ threshold, go to 7;
4.	clean the dirty map by $d_n(\tau) = d_{n-1}(\tau) - \hat{\alpha}_n R_{pp}(\tau - \hat{\tau}_n)$;
5.	update the clean map by $c_n(\tau) = c_{n-1}(\tau) + \hat{\alpha}_n \delta(\tau - \hat{\tau}_n)$;
6.	go to step 2;
7.	the CIR is then $\hat{h}(t) = c_n(t)$.

Table 2.2: Enhanced CLEAN deconvolution algorithm.

In [42], modification was made to combine inverse filtering technique and CLEAN; however, inverse filtering can be problematic since there is a wide range of filters

[14, 39], each would give a different result. A multi-template approach was introduced in [39], where, instead of using a single LOS template as the *a priori*, it uses more than one template. The templates are received waveforms at different receiver angle-of-elevation (AoE) which acts as non-orthogonal basis functions for CIR estimation. For k different templates $\hat{p}^j(t)$ for $j = 1, 2, \ldots, k$, the channel model for multi-template approach is defined as [39]

$$h(\tau) = \sum_i \alpha_i \hat{h}^j(\tau - \tau_i)\,, \tag{2.2}$$

where $\hat{h}^j(\tau)$ denotes the impulse response experienced by the j-th template $\hat{p}^j(\tau)$, and equals $\delta(\tau)$ for LOS. Hence, $\hat{p}^j(\tau) = \hat{h}^j(\tau) \otimes \hat{p}^1(\tau)$, assuming $\hat{p}^1(\tau)$ is the LOS pulse at 0° AoE. Table 2.3 lists the multi-template algorithm.

1.	initialize the dirty map $d_0(t)$ as $d_0(t) = y(t)$ and the clean map with $c_0(t) = 0$;
2.	form the normalized cross-correlation functions $R_{d\hat{p}^j}(\tau) = d_n(t) \odot \hat{p}^j(t)$, for $j = 1, 2, \ldots, k$;
3.	compute $\hat{\tau}_n^j = \arg\max_\tau \lvert R_{d\hat{p}^j}(\tau)\rvert$ and $\hat{\alpha}_n^j = R_{d\hat{p}^j}(\hat{\tau}_n^j)$, $j = 1, 2, \ldots, k$;
4.	if all $\hat{\alpha}_n^j <$ threshold, go to step 8;
5.	clean the dirty map by inserting zeros in place of the detected MPC;
6.	update the clean map as $c_n(\tau) = c_{n-1}(\tau) + \hat{\alpha}_n^j \hat{h}^j(\tau - \hat{\tau}_n^j)$;
7.	go to step 2;
8.	the impulse response is then $\hat{h}(t) = c_n(t)$.

Table 2.3: The multi-template CLEAN deconvolution algorithm.

Unfortunately, this algorithm computes correlation at each iteration, assumes non-overlapping MPC's because of the dispersive environment, and, instead of subtractions, it zeros the dirty map. Because of this zeroing, not all of the received signal energy can be captured by the algorithm [39]. In [46], a modification to the multi-

template algorithm was proposed; however, it defeats the purpose of the autocorrelation by computing the cross-correlation for each iteration. Furthermore, the *a priori* templates were extracted manually from a single 0° AoE LOS measurement. Hence, the pulse distortions were subjective and can be quite different depending on interpretation.

The above algorithms assume $\hat{h}(\tau)$ to be independent of generator output, the measurement system, and the antennas used. Despite accurate estimation, the aforementioned algorithms are still based on a modeled approach; therefore, their outputs (i.e., the CIR) must be carefully interpreted.

Performance Measures

Performance for CLEAN are often categorized by the mean-squared error (MSE), correlation coefficient ρ, energy capture ratio, relative error, and least squares condition [14]. Although the reconstruction from CIR estimation may closely resemble the measurement, it does not necessary mean the CIR is correct. An incorrect estimation to per-path distortion would often produce "phantom paths" as the real MPC [6], [41]. In Chapter 3, we will address these issues of the CLEAN algorithm and propose an enhancement to the multi-template algorithm listed in Table 2.3.

2.1.2 Pulse Distortion

Although UWB allows the rich collection of multipath, operating with ultra-wide BW can cause performance degradation due to pulse distortion [6, 11]. Because of the wide spectral occupancy of these pulses, and a significant number of objects in the channel, the received signal is always severely distorted due to the frequency selectivity of the radio wave propagation mechanism [6, 11], which often arise due to object's material [12], orientation and shape [10], especially in non-LOS (NLOS) and

long-range LOS applications. In signal processing and, likewise, the CLEAN deconvolution, the pronounced effect of pulse distortion can significantly lowers the output SNR of a matched filter (MF) based system by mismatching with the stored template, thus degrades the system performance [26]. As an example, Fig. 2.1 illustrates the pulse distortion due to diffraction. We consider the transmission of a single Gaussian pulse, i.e., $t\exp(-2\pi(t/\tau_m)^2)$ with $\tau_m = 0.5$ ns, convolving with the generalized channel $h(t) = t^{-(1+p)}U(t)$ [11], where $U(t)$ is the unit step function, $p \in [-1, 0)$ is a parameter which characterizes the scattering center, and the receiving antenna acts as a differentiator [5]. Due to diffraction and depending on p, the received pulses shown hardly resembles the unit-energy second derivation Gaussian pulse, drawn in thin red line.

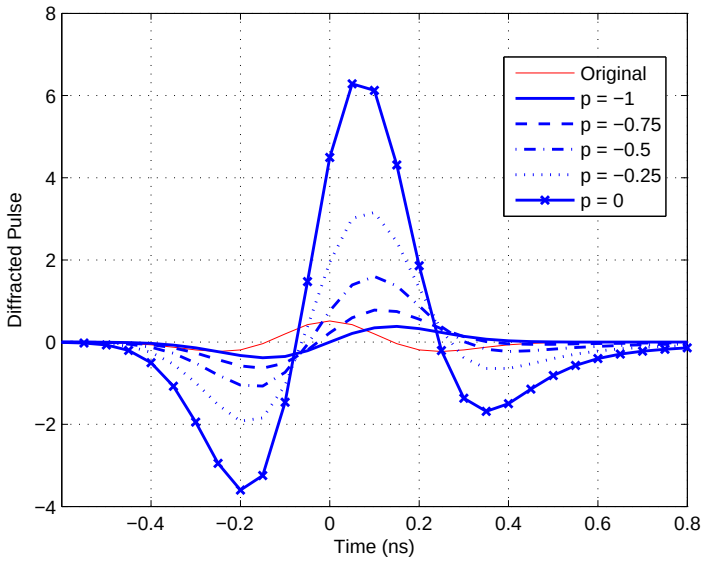

Figure 2.1: Typical UWB pulse after distortion by diffraction for different values of p. The transmitted pulse is a unit-energy first derivative Gaussian.

2.2 ToA Estimation with UWB-IR

The U.S. FCC spectrum mandate for UWB communications in 2002 has brought forth many potential applications. Particularly in ranging and localization, UWB-IR has shown to be a promising candidate that can enable centimeter accuracy with minimal cost on the SNR [7]. The robustness of UWB-IR in ranging can be demonstrated as a special case of (2.1) when $N = 1$, as

$$y(t) = \alpha_1 p(t - \tau_1) + n(t)\,, \tag{2.3}$$

where $p(t)$ is the received pulse of duration T_p, $n(t)$ is the additive white Gaussian noise (AWGN) with double-sided power spectral density (PSD) $N_0/2$, and we have assumed a pure single-tap AWGN channel. The unbiased delay estimate $\hat{\tau}_1$ to τ_1 in (2.3) can be achieved by the ML estimator [49, 50], one which finds the maximum cross-correlation between $y(t)$ and $p(t)$. The CRLB measures the accuracy of the unbiased estimator, and for the unbiased range estimate between the TX and RX, i.e., $\hat{d} = c\hat{\tau}_1$, to $d = c\tau_1$ in (2.3), the variance of $\hat{d}$ is bounded as [7, 49, 50]

$$\sigma_{\hat{d}}^2 = \mathbb{E}\{(\hat{d} - d)^2\} \geq \text{CRLB} = \frac{c}{8\pi^2\beta^2\text{SNR}}\,, \tag{2.4}$$

where $\beta^2 = \int_{-\infty}^{\infty} f^2|P(f)|^2\,\mathrm{d}f / \int_{-\infty}^{\infty} |P(f)|^2\,\mathrm{d}f$ is the second moment of spectrum $P(f)$ of $p(t)$, i.e., the BW of $p(t)$, and c is the speed of light. From (2.4), it is obvious that to improve the ranging accuracy one can either increasing the SNR or the effective signal BW. Hence, the inherent wideband characteristic of UWB-IR is advantageous for precision asset localization and ranging.

Locating a node in a WSN involves obtaining the range information between a TN and a group of RN's [7]. When the positions of the RN's are known, the whereabouts

of the TN can be estimated by obtaining the range information from radio signals traveling between the nodes. Then, combining these range estimates to produce the position estimate of the TN within the network [7, 15]. For a real-time application which demands the instantaneous tracking of the TN position, the processing of information must be on the order of a fraction of a second, so a good estimator not only has to guarantee ranging accuracy but also low in complexity to enable real-time signal processing.

The range information that is often embedded in the direct path (DP) signal can be retrieved by techniques such as the ToA estimation [15, 16]. By operating with pulses having a wide spectral support, UWB-IR enables fine time resolution that complements the time-based positioning technique as the viable solution for cost-effective, high-resolution ranging and localization. However, the wide spectrum can have a pronounced impact on estimation since the incurred MPC's are often stronger than the DP [5], and due to the complexity of the UWB wave propagation mechanisms [6], any devised estimator which seems to work in simulation must also be tested with realistic range measurements.

To address these, Lee and Scholtz [17] first considered impulse based ranging technique in dense multipath with the generalized maximum likelihood estimator which detects the DP arrival while treating other MPC's as nuisance parameters. However, it is an iterative algorithm that operates on Nyquist rate samples. To reduce the sampling rate, [19] proposed an energy detector (ED) based ToA estimator which captures the ToA as the first energy level to exceed a threshold in a single frame. The frame in [19] is decomposed into a number of energy blocks so that the high resolution capability of the ED hinges on having a small block size. Moreover, because of a square-law device its performance degrades at low SNR. To improve the ED performance and reduce search complexity, [18] introduced a two-stage ToA

algorithm which combines the ED as an initial coarse estimate followed by correlation over chip delays in the estimated time bin of the first stage. In [7], a dirty-template reference based scheme for symbol-rate samples was proposed. An inverse problem approach to ToA estimation was proposed by [51], where the authors estimate the ToA by treating it as a by-product of the large scale least squares (LS) solution. Although this algorithm is simple, due to a combination of both the noisy signal and the modeling of closely-spaced MPC's in the construction of the LS channel matrix, the problem is *ill-conditioned* and suffers from output instability when taking the pseudo-inverse. Additionally, its performance is not well documented and the relationship on delay models is not examined.

In all of the above literatures except [17], the performance was mostly evaluated via the computer simulation of certain UWB channel model, such as the IEEE 802.15.3a [8] or 4a models, with no results pertaining to the actual ranging measurements, which can be quite different given the intricacy of the wave propagation mechanisms of pulses having a wide spectral support [52]. In contrast, Low *et al.* [53] experimentally demonstrated a UWB ranging scheme in the LOS environment, and Falsi *et al.* [20] illustrated a set of ToA estimators based on the indoor measurement data from [5]. Both employ the peak-detection-based (PDB) algorithms which estimate the ToA from a number of peaks in the MF output. In [53], the first arriving peak after one MF computation which exceeds a threshold is declared the ToA, whereas, [20] requires multiple MF computations to achieve the high-resolution[1]. In [20], the PDB algorithms are shown capable of estimating the ToA while being efficient at energy capture in both LOS and NLOS environments. In Chapter 4, we will propose and evaluate a simple ToA estimator to address these issues.

[1]The high-resolution algorithms can be viewed as a special case of the single-template CLEAN deconvolution algorithm outlined in Section 2.1.

2.3 Channel Estimation for UWB-IR

The rich multipath characteristic of a wireless communication system operating with sub-nanosecond pulses is one of the most attractive features of UWB-IR [2]. Coupled with the fine time resolution and low-power implementation, UWB-IR is an emerging candidate for both localization and ranging applications. The rich multipath diversity of an impulsive wideband channel calls for the use of Rake receivers [22] for significant energy capture, higher performance and flexibility, despite its complexity over sub-optimal counterparts [26], e.g., autocorrelation receivers and non-coherent detectors. In addition, accurate multipath delay (and amplitude) estimates are indispensable for precision asset localization and tracking with UWB-IR [7]. Especially when the distribution of NLOS path delays are known *a priori*, accurate channel estimates can dramatically boost the ToA positioning accuracy [36]. The ML channel estimator for UWB was first proposed in [5] for the transmission of an isolated pulse. Its DA alternative was later suggested in [23] to enhance the estimator accuracy, especially in a noisy environment. Although the ML scheme is shown to be a superior estimator, the tremendous BW of UWB signal renders its implementation difficult because of the Nyquist criterion.

Most existing literatures on ML complexity reduction tackle the issue by redefining the problem, relying on the imminent arrival of advanced DSP, or eliminating the use of ML altogether. Refs. [24] and [25] approached the complexity issue by way of formulating it as a synchronization or timing recovery problem, respectively. A frame synchronization approach to complexity reduction was addressed in [24], where a search over possible frame delays was performed to maximize the log-likelihood function. In contrast, [25] eliminated the ML formulation and concentrated on timing recovery with LS signal model. In [26], the ML estimator was simplified by recognizing multipaths do arrive in clusters, and executing search only for rays falling into

the highest energy clusters. Although they are of low-complexity, their performance implicitly depends on acquiring high-rate samples. Ref. [27] proposed a *finite rate of innovation* approach which projects a signal into lower dimensional subspace. Unfortunately, due to the closely spaced path arrivals inherent in UWB-IR, the solution to rate of innovation is often ill-conditioned. Despite these attempts, the most critical issue - Nyquist sampling rate reduction - of the ML channel estimator has yet to be addressed.

New receivers have also been proposed to preclude the use of channel estimating Rake. Suboptimal receivers such as the energy detectors [29] and autocorrelation receivers [28, 31] generally take a SNR penalty in order to achieve similar performance to the coherent counterpart [32]. Recently, there has been a renewed interest in the use of Rake in UWB communications, e.g., MIMO systems [33], BAN [34], cooperative BAN [35], and the prerake systems [30]. In essence, the design or enhancement of accurate channel estimator must not be overlooked for UWB-IR technology.

The emerging theory of compressed sensing (CS) outlines a novel strategy to jointly compress and detect a sparse signal with fewer sampling resources than the traditional method. For a signal $\mathbf{x} \in \mathbb{R}^N$ which is Y-sparse, with $Y \ll N$ being an integer, compressed sensing shows that with high probability $\mathbf{x}$ can be reconstructed from M compressive measurements when $M \geq CY \log(N/Y) \ll N$, where $C \geq 1$ is the oversampling factor [54, 55]. Compressed sensing for UWB was first proposed in [56] as a generalized likelihood ratio test receiver taking advantage of the signal structure by incorporating pilot assisted modulation. It was later discussed in [57] as an alternative for UWB channel estimation. Both cases estimate the signal structure via the matching pursuit (MP) ℓ_1-norm minimization algorithm. Unfortunately, how well MP estimates ties directly to the design parameters, such as the number of iterations and residual error for convergence [56, 57], which are subject to change

depending on the environment. In addition, MP requires a complete $N \times N$ basis as the dictionary for accurate estimation and its performance degrades when there is noise present. We will address the sampling issue in Chapter 5 by incorporating the channel estimator with compressive measurements to produce a low-complexity, i.e., acquiring low-rate samples, version of the conventional ML channel estimator.

2.3.1 ML Channel Estimator

To perform DA channel estimation, the ML-type channel estimator first transmits K pilot symbols, and the received signal can be modeled as [23, 26]

$$y(t) = \sum_{k=0}^{K-1} \sum_{l=1}^{L} \alpha_l p(t - \tau_l - kT_s) + n(t)\,, \tag{2.5}$$

where we have assumed similar channel structure as in (2.1) with arbitrary tap gain α_l and delay τ_l, for $l = 1, \ldots, L$, and similar variable definitions as (2.3), except T_s denotes the symbol period with total observation time $T_0 = KT_s$, and one pulse is sent per symbol. Then the ML estimator estimates the path delay and gain as

$$\hat{\tau}_i = \arg\max_{\tilde{\tau}_i} \left(\sum_{k=0}^{K-1} v_k(\tilde{\tau}_i) \right)^2, \quad i = 1, \ldots, L_c\,, \tag{2.6}$$

$$\hat{\alpha}_i = \frac{\sum_{k=0}^{K-1} v_k(\hat{\tau}_i)}{KE_s}\,, \quad i = 1, \ldots, L_c\,, \tag{2.7}$$

where $v_k(\tilde{\tau}_i) = \int_{T_0} y(t) p(t - \tilde{\tau}_i - kT_s)\,\mathrm{d}t$, $\hat{x}$ and $\tilde{x}$ denote the estimate to and a trial value of the variable x, respectively, $E_s := \int_{T_s} p^2(t)\,\mathrm{d}t$ is the symbol energy, and L_c is the number of taps to estimate. Non-DA version of the estimator is also available [23, 24] with slight modification. As mentioned in Lottici *et al.* [23], the template $p(t)$ used in (2.6) and (2.7) requires construction by oversampling at the Nyquist-rate, which exacerbates the power requirement and limits the digital implementation of

the channel estimator when having to search through all possible $\tilde{\tau}_l$. Variants of the ML-type estimator exists, e.g., [26, 30], but all require the oversampling of $p(t)$ to produce reliable estimates.

2.3.2 MRC Rake Receiver

The MRC Rake receiver produces the optimal decision statistic by the construction of and the correlation with a stored-reference template according to the CSI [22]. In Chapter 5, we will consider antipodal pulse amplitude modulation (A-PAM) with a Rake receiver in a single-user scenario. For that, the received signal after propagation through a fading channel can be modeled as

$$y(t) = \sum_i b_i \sum_{l=1}^{L} \alpha_l s(t - \tau_l - iT_s) + n(t)\,, \tag{2.8}$$

where $\{b_i\}$ are the data symbols taking on the values of ± 1 with equal probability. Upon reception, the Rake receiver performs the MRC on the decision statistic as [23]

$$\nu_i = \sum_{l=1}^{L_c} \hat{\alpha}_l \int_{iT_s}^{iT_s+T_{prj}} y(t) p(t - iT_s - \hat{\tau}_l)\,\mathrm{d}t\,, \tag{2.9}$$

where the sequences $\{\hat{\alpha}_l\}$ and $\{\hat{\tau}_l\}$ are the CSI estimates, and $T_{prj} \in [0, T_s)$ denotes the integration interval for the i-th symbol. One may use the estimators described in Section 2.3.1 to obtain $\{\hat{\alpha}_l\}$ and $\{\hat{\tau}_l\}$. Eqs. (2.5)–(2.9) can be easily extended to multiple frames per symbol case [23, 26].

2.4 Summary

In this chapter, we have reviewed background information and existing literatures on different aspects of UWB-IR, namely, channel characterization, ToA estimation,

and channel estimation. We noticed that due to the frequency-selective pulse distortion, the *a priori* assumption on CLEAN-type deconvolution must be considered with care. Although UWB-IR is a promising candidate in centimeter-accuracy positioning system, a simple estimator that can provide real-time range information is still yet to be devised. Finally, the MRC Rake can provide significant energy capture, high performance and flexibility over the suboptimal receivers, but one must address the issue of acquiring low-rate samples in CSI estimation. The following 3 chapters will attempt to address these issues.

Chapter 3

A High-Resolution, Multi-Template Deconvolution Algorithm for Time-Domain UWB Channel Characterization

3.1 Background

In this chapter, we examine the *a priori* dependence of the CLEAN algorithm and devise an enhanced multi-template CLEAN algorithm. We first examine the effect of the deconvolution performance, in terms of the MSE and correlation coefficient, on both LOS and NLOS measurements with imperfect LOS templates, an ideal Gaussian monocycle, and several noise templates. Then, continuing from the work of [39], we propose a high-resolution, multi-template deconvolution algorithm which utilizes realistic frequency-dependent pulse distortions to further enhance the channel impulse response (CIR) estimation accuracy. We view the CLEAN algorithm as using

templates which are non-orthogonal basis functions, and the algorithm here offers improvements over its predecessor. However, the resulting CIR must be interpreted with great caution for frequency-selective, NLOS channels.

The rest of this chapter is organized as follows: Section 3.2 presents a system model for the time-domain channel measurement. To examine the *a priori* assumption on the CIR, Section 3.3 describes our approach to obtain the realistic measurement, and a study on the *a priori* dependence of CLEAN is given in Section 3.4. Finally, we propose an enhanced multi-template deconvolution algorithm in Section 3.4, and compare its performance against the previous algorithm in Section 3.5. A summary is given in Section 3.6.

3.2 Time-Domain Channel Characterization

3.2.1 Channel Measurement

Time-domain channel sounding involves the use of a pulse generator, a pair of antennas, a low-noise amplifier (LNA), and a digital sampling oscilloscope (DSO), which acts as the receiver (RX), to measure the channel [6, 13]. For simplicity, assuming the UWB channel to be wide-sense stationary (WSS), the CIR can be modeled as a summation of frequency-dependent MPC's from N effective scatterer sources as [6]

$$h(\tau) = \sum_{i=1}^{N} \alpha_i \chi_i(\tau) \otimes \delta(\tau - \tau_i)\,, \tag{3.1}$$

where $\chi_i(\tau)$ is the frequency dependent distortion on the i-th echo after interaction with the environment. Here, the MPC's are not necessarily resolvable. Considering antenna filtering effects, for a free space impulse transmission $p(\tau)$ which is sent to the channel in (3.1), the received signal $y(\tau)$ after propagation and ignoring the noise

effect[1] becomes [43]

$$y(\tau) = p(\tau) \otimes h(\tau) = \sum_{i=1}^{N} \alpha_i \chi_i(\tau) \otimes p(\tau - \tau_i) \\ = \sum_{i} \alpha_i p_i(\tau - \tau_i)\,. \tag{3.2}$$

The pulse shape corresponding to the i-th MPC is now strongly dependent on the propagation path. For indoor channel sounding, this pulse distortion is more pronounced so the impact of assuming negligible pulse distortion on the received signal must be considered with care. For time-domain measurement, (3.2) is readily observable at the DSO output. If high-resolution CIR is required, $y(\tau)$ can be further processed with the CLEAN algorithm [14].

3.3 Measurement and Processing

To show the impact of *a priori* assumption on CLEAN, a time-domain UWB measurement campaign was conducted at the Wireless Communications Research Laboratory of Simon Fraser University. The laboratory is a combination of research facilities and offices. Fig. 3.1 illustrates the measurement setup.

A pulse generator periodically sends a 300 ps-wide Gaussian monocycle to the antenna. The excitation pulse has a 10-dB BW of 4.7 GHz. On the RX, a 26 dB gain, 12 GHz 3-dB BW LNA is used to amplify the signal before it is being sampled by the DSO at 20 ps per sample. The antennas are a matched pair of omni-directional wideband bicones with an impedance BW of 2–18 GHz. A separate signal generator is used to trigger both the pulse generator and the DSO. To minimize the channel disturbance, measurements were automated by a laptop through a GPIB interface. Both LOS and NLOS measurements were taken with a varying RX distance.

[1] We will consider the noise effect in measurement post-processing.

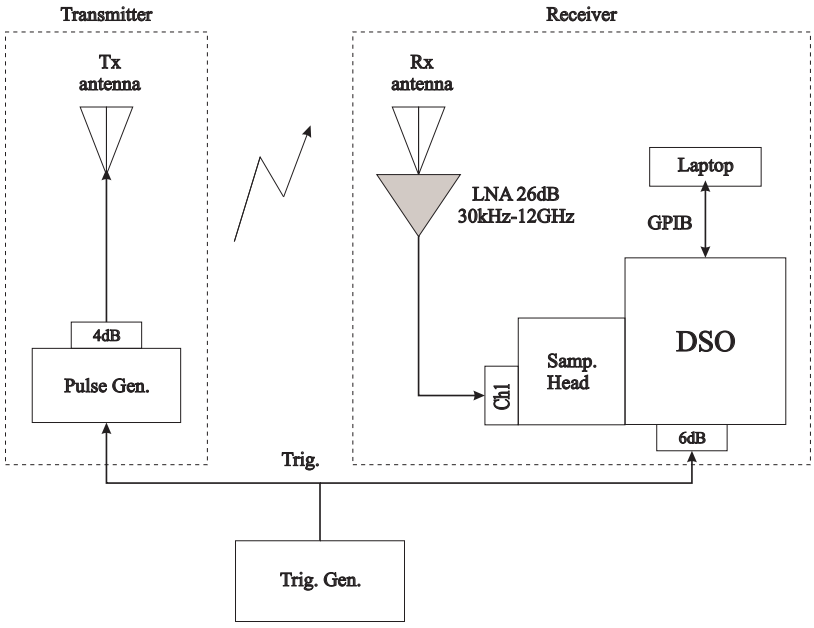

Figure 3.1: Time domain measurement setup.

Moreover, 180 profiles of 5 profiles per grid point were recorded on a 6-by-6 grid of size 0.56 m^2 at each distance to foster accurate statistics. The grid separation is 0.15 m, and a profile length of 400 ns was used. To eliminate both the out-of-band noise and the DC bias, the waveforms were first digitally filtered with a 0.1–12 GHz bandpass filter, followed by a moving window average of length 3 samples before being processed by the CLEAN algorithm.

3.4 Subtractive Deconvolution

Different types of template are used to demonstrate the *a priori* dependence of the CLEAN algorithm, they are: 1 m LOS templates of different angle-of-elevation (AoE), an ideal Gaussian doublet, and filtered noise template of both short and long durations. The durations are determined by the finite time support of either the AoE template or the measurement.

3.4.1 Single-Template CLEAN

The CLEAN algorithm of [38] is implemented to process measurements with other *a priori* assumptions. The process exits when either $1,000$ iterations expire or MPC's of 20 dB below peak are detected. Once CLEAN exits, the resultant clean map is the channel estimation $\hat{h}(\tau)$, and a convolution between the estimation and the *a priori* gives the reconstructed signal $\hat{y}(\tau)$. Table 3.1 lists the deconvolution accuracies, and Fig. 3.2 plots the accuracies with different AoE templates as the *a priori* for sets of LOS and NLOS data. As shown, the channel estimation and its waveform reconstruction clearly depend on the *a priori* model. It is also interesting to note that the accuracy improves with a $-60°$ template than a $0°$ one. However, it is difficult to draw conclusions about the channel from this information. Even with

MSE and correlation coefficient between $y(\tau)$ and $\hat{y}(\tau)$	MSE		Correlation Coefficient	
	LOS	NLOS	LOS	NLOS
0° AoE template	0.0610	0.0147	0.8037	0.8851
Gaussian doublet, $\tau_m = 0.334$[2]	0.0552	0.0143	0.8240	0.8889
Filtered noise, short duration	0.0534	0.0254	0.8318	0.8027
Filtered noise, long duration	0.1593	0.0604	0.2828	0.3431

1. Gaussian doublet as described in [5].

Table 3.1: Single-Template Deconvolution Accuracies.

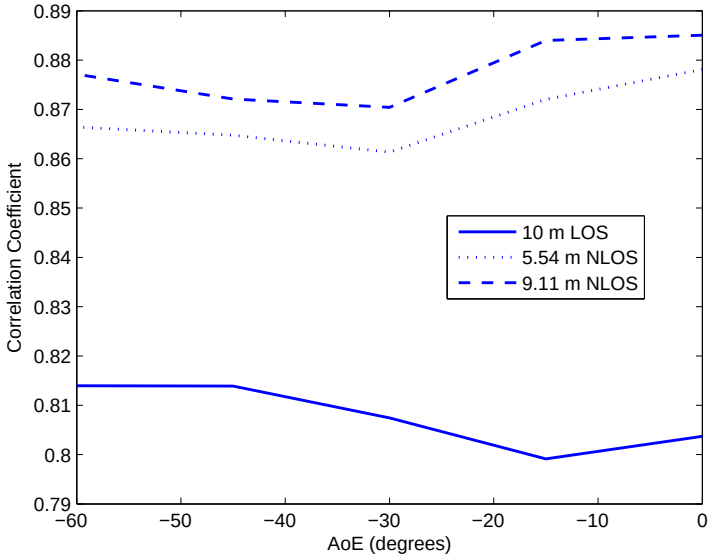

Figure 3.2: Correlation coefficient vs. 1 m LOS *a priori* template of varying AoE.

templates which have no relationship to the sounding pulse, the signal can still be reproduced with apparent accuracy! For example, Fig. 3.3 demonstrates one instance

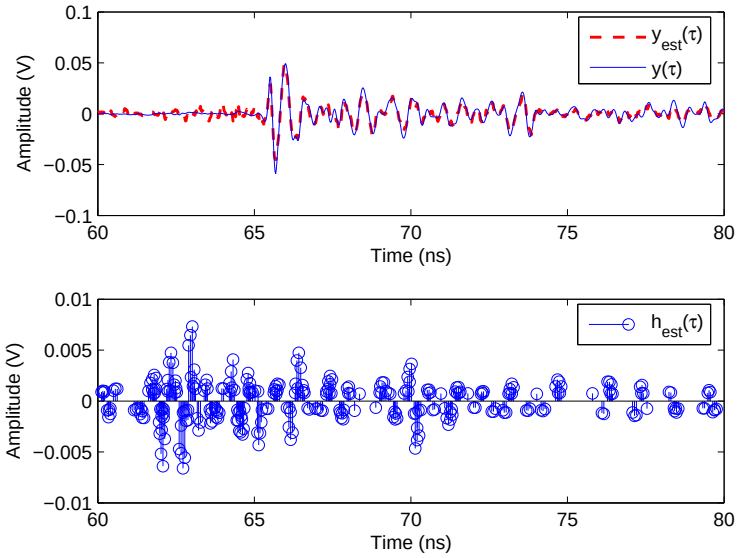

Figure 3.3: A transient response comparison between a 10 m LOS measurement $y(\tau)$ and CLEAN reconstruction $\hat{y}(\tau)$. The bottom figure shows the estimated CIR $\hat{h}(\tau)$ with short duration, filtered noise as the *a priori*.

of LOS $y(\tau)$, $\hat{y}(\tau)$, and $\hat{h}(\tau)$ with short duration, filtered noise as the *a priori*. In this case, $\rho = 0.8143$ even though the template is simply random noise.

3.4.2 Multi-Template CLEAN

The assumption that a received profile is simply the summation of delayed and scaled versions of the *a priori* template seems unlikely to be valid. As described in [39], one approach to circumvent this problem is to deconvolve with more than one template. Although this modification still involves *a priori* models, it at least *attempts* to address the issue of frequency selective pulse distortion. Unfortunately, this algorithm is more complicated in that it requires the cross-correlation calculation for each iteration, and

further degrades any resolution accuracy by assuming none overlapping MPC's due to a dispersive environment. Because of this assumption, not all the energy can be captured in the deconvolution algorithm. To overcome these problems, we propose an enhancement to the work of [39] to effectively increase its estimation accuracy while attaining computational efficiency.

Continuing from (2.2), the multi-template deconvolution algorithm is modified as in Table 3.2, where we let $\hat{p}^j(t)$ be the 1 m LOS measurement at different AoE. The advantages of this algorithm are: channel estimation accuracy, since it no longer

1.	initialize normalized cross-correlation between $y(t)$ and $\hat{p}^j(t)$ as $R_{y\hat{p}^j}(\tau) = y(t) \odot \hat{p}^j(t)$, for $j = 1, 2, \ldots, k$, and define the dirty and clean map as $d_0^j(\tau) = R_{y\hat{p}^j}(\tau)$ and $c_0(\tau) = 0$;
2.	compute $\hat{\tau}_n^j = \arg\max_\tau \lvert R_{y\hat{p}^j}(\tau)\rvert$ and $\hat{\alpha}_n^j = R_{y\hat{p}^j}(\hat{\tau}_n^j)$, for $j = 1, 2, \ldots, k$;
3.	if all $\hat{\alpha}_n^j <$ threshold, go to 7;
4.	clean the dirty map by inserting zeros in place of detected MPC as $d_n^j(\tau_p) = 0$, where τ_p spans the same duration as $\hat{p}^j(t)$, for $j = 1, 2, \ldots, k$;
5.	update the clean map by $c_n(\tau) = c_{n-1}(\tau) + \hat{\alpha}_n^j \hat{h}^j(\tau - \hat{\tau}_n^j)$;
6.	go to step 2;
7.	the CIR is then $\hat{h}(t) = c_n(t)$.

Table 3.2: Enhanced multi-template CLEAN deconvolution algorithm.

works on received signal zero padding, rather on cross-correlations to permit better peak detection and retain finer resolution; computational efficiency, since it no longer requires correlation on every loop (although, as noted above, this is normally not a major issue), and it does not require the use of subjective templates as in [46]. Furthermore, this algorithm is also simple to implement and works on point-to-point measurements, unlike the Sensor-CLEAN and its variant. It is also less susceptible to output instability caused by sample misalignment during the deconvolution process, which often occurs when there is significant pulse distortion on the *a priori* templates.

Hence, it is possible to incorporate templates such as a through-wall measurement. Finally, the channel estimation can be further improved by varying the size of τ_p; this is *not possible* for both [39] and [46].

3.5 Results and Analysis

To illustrate the gain over the previous multi-template approach, a set of LOS and NLOS measurements are processed with the algorithms. Fig. 3.4 plots the improvement in correlation coefficient at a fixed τ_p. For the case of one to five reference

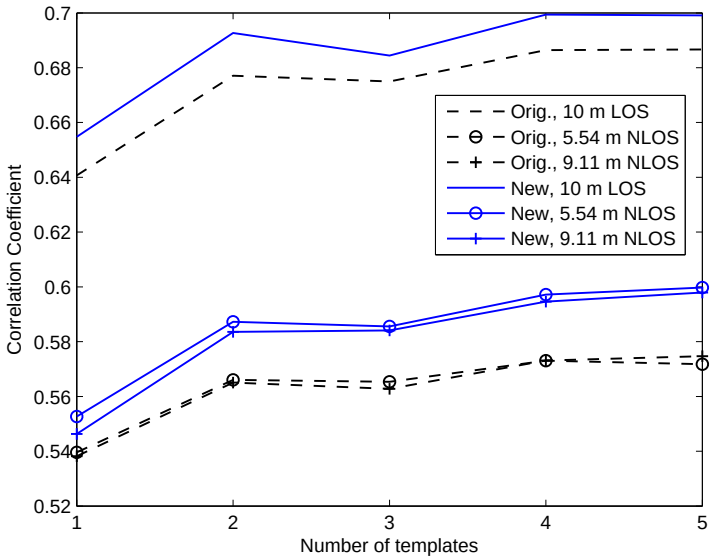

Figure 3.4: Improvement in correlation coefficient vs. number of multi-template between the the original algorithm from [39] and the newly proposed algorithm. Here, τ_p equals the sample length of the *a priori* templates.

templates $\hat{p}^j(t)$ for $j = 1, \ldots, 5$, the combinations are: $0°$, $(0°, -45°)$, $(0°, -45°, -60°)$, $(0°, -30°, -45°, -60°)$, $(0°, -15°, -30°, -45°, -60°)$, respectively. By working with correlations, we see a consistent, albeit small, increase in the apparent estimation accuracy as compared to the previous approach, especially in NLOS

scenario where the pulse distortion dominates. For example, the improvement, i.e., change in ρ between our proposed algorithm and the original CLEAN from [39], for LOS case ranges from $\Delta\rho = 0.0141$ to 0.0124 for single to up to five templates. For NLOS, the improvement from single to five templates ranges from $\Delta\rho = 0.0131$ to 0.0280, and from $\Delta\rho = 0.0081$ to 0.0233 for 5.54 m and 9.11 m measurements, respectively. These improvements would not have been possible if we were to update the dirty map, as opposed to the correlation functions, on the CLEAN algorithm. Similar improvements are also observed when compared by the MSE. As was observed in [39], by increasing the number of templates, the estimation can be further improved due to the inclusion of more pulse distortions on the *a priori*.

Fig. 3.5 illustrates the apparent improvement in estimation accuracy as τ_p varies for both LOS and NLOS measurements. As shown, the correlation coefficient improves as τ_p decreases; hence, it is possible to find an optimum τ_p which maximizes ρ for a set of measurements. For the best τ_p in the example above, i.e., $\tau_p = 75$, the improvement for LOS ranges from $\Delta\rho = 0.0938$ to 0.1184 for single to up to five templates. For NLOS, the improvement ranges from $\Delta\rho = 0.1559$ to 0.1817, and from $\Delta\rho = 0.1598$ to 0.1797 for 5.54 m and 9.11 m measurements, respectively. These improvements are small in the context of the uncertainty of correlation analysis. However, they are consistent and exist since a smaller τ_p results in more resolvable MPC's, thus a higher MPC resolution. This is especially important for the NLOS case where the channel often contains significant number of MPC's, all of which must be properly identified in order to improve the estimation performance. Unfortunately, the high-resolution capability cannot be realized for the algorithms in [39, 46] since both sacrifice the energy capture by operating on the dirty map.

To illustrate this, Figs. 3.6 and 3.7 compare the energy capture ratio and relative error versus number of single-path correlators between the modified and the original

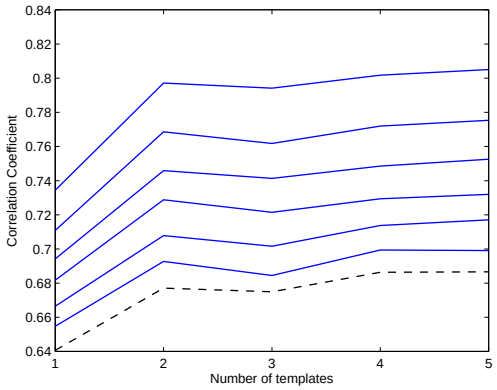

(a) 10 m LOS

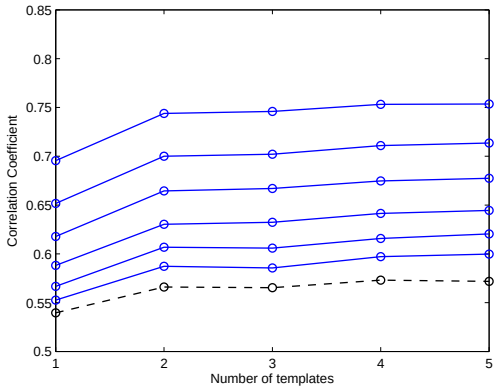

(b) 5.54 m NLOS

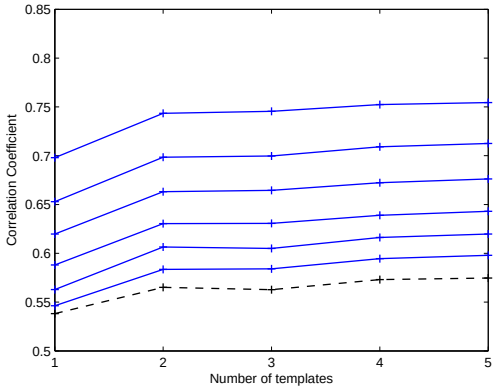

(c) 9.11 m NLOS

Figure 3.5: Improvement of correlation coefficient vs. number of multi-template for a varying τ_p of 75, 100, 125, 150, 175, and 200 samples, from top to bottom, respectively. The solid lines are proposed algorithm, and the dashed lines are the original algorithm.

multi-template CLEAN. For $\tau_p = 75$ with five templates, the modified algorithm can capture up to 83.97%, 62.75%, and 56.55% of energy with 50 single-path correlators, as compared to 46.10%, 31.20%, and 30.70% from the original algorithm for 10 m LOS, 5.54 m and 9.11 m NLOS, respectively. For relative error under similar conditions, the numbers are 44.93%, 58.80%, and 62.24%, as compared to 53.48%, 68.42%, and 68.98%, for 10 m LOS, 5.54 m and 9.11 m NLOS, respectively. Furthermore, the energy capture capability of the original algorithm saturates owing to the assumption of none overlapping MPC's. In contrast, our approach does not have this limitation and captures more energy as the number of correlators increases.

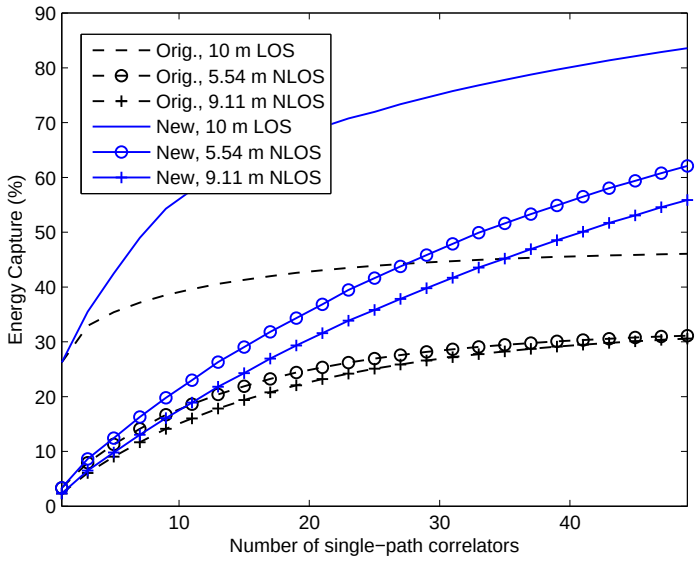

Figure 3.6: Comparison of energy capture ratio vs. number of single-path correlators for $\tau_p = 75$ and five multi-template between the original and new CLEAN algorithms.

Apart from the improvements in estimation, the main advantage of working with cross-correlation functions is an increase in computational efficiency. To demonstrate this, we processed the data under identical computer environments. Fig. 3.8 shows the gain for $\tau_p = 75$ and five *a priori* templates. The improvement on LOS is 1.3993

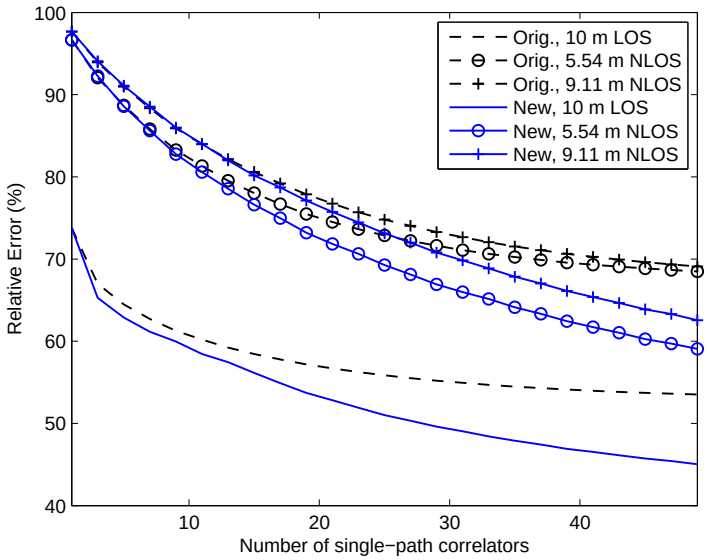

Figure 3.7: Comparison of relative error vs. number of single-path correlators for $\tau_p = 75$ and five multi-template between the original and new CLEAN algorithms.

s, and, for NLOS, the gains range from 1.2720 s to 1.7670 s for 5.54 m and 9.11 m measurements, respectively. Improving the computational efficiency may become significant in large-scale NLOS post-processing where the identification of a large number of MPC's is mandatory for accurate estimation.

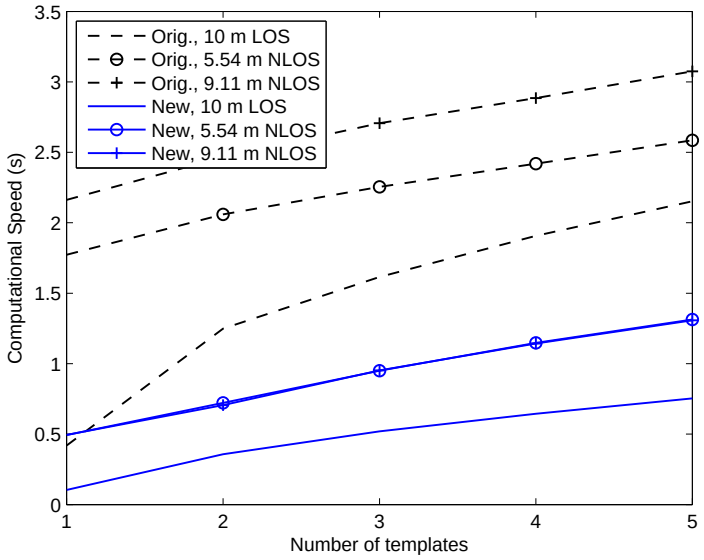

Figure 3.8: Computational speed vs. number of multi-template with $\tau_p = 75$ between the original and new CLEAN algorithms.

3.6 Summary

In this chapter, we have studied the *a priori* dependency of CLEAN with real-world measurements under several *a priori* models. It was shown that even with templates which are unrelated to the sounding pulse, the signal can still be reproduced with good accuracy. Hence, modification must be made to account for the frequency-selective pulse distortion, which is an important characteristic of an impulsive ultra-wide bandwidth propagation channel. For that, we have proposed an enhanced multi-template CLEAN algorithm which considers the wideband radio wave propagation

mechanisms, and was shown to supersede its predecessor by being computationally efficient, simple, accurate, and deployable for point-to-point measurements. However, the results produced by these modeled deconvolution must be interpreted with great care for frequency-selective NLOS channels.

Chapter 4

Multiresolution Wavelet Denoising for Ultra-Wideband Time-of-Arrival Estimation with Regularized Least Squares

4.1 Background

As discussed in Section 2.2, a low-complexity ToA estimator that is capable of ranging in low SNR is crucial to the design of real-time positioning systems. To improve the estimator accuracy at low SNR and attain low complexity for the ease of real-time positioning, we propose a *regularized* LS (RLS) approach with wavelet denoising (WD) to the problem of ToA estimation. Pioneered by Donoho and Johnstone [58], WD has been successfully applied to boost the low SNR performance of time-delay estimator [59] and several direction-of-arrival algorithms, e.g., [60, 61]. Our technique utilizes the discrete wavelet transform (DWT), and hyperbolic shrinkage of [62]

with the threshold developed by Donoho [63] to effectively enhance the SNR prior to RLS channel estimation; thereafter, the final retrieval of accurate ToA information via a thresholding technique. Our approach is simple and enables fast, on-the-fly, high-resolution ToA estimation applicable to real-time ranging system. We devise a threshold selection strategy based on the Neyman-Pearson (NP) criterion of constant false alarm (CFA), and demonstrate the superior performance of our estimator in both computer simulation and with realistic UWB ranging measurements. When Nyquist sampling rate is available, our estimator is shown to outperform the ED [19] in ToA estimation, and the high-resolution PDB algorithms [20] in both ToA estimation and computational complexity. In addition, the performance of our estimator can be improved when adapting the CFA criterion for threshold selection. To the best of authors' knowledge, this approach has yet to be adopted for UWB-IR ToA estimation. Note that higher resolution can be achieved by interpolating from the Nyquist rate samples.

The rest of this chapter is organized as follows: Section 4.2 presents the overall system model, including a description of both LS and RLS channel estimators. To examine the benefits of denoising, Section 4.3 describes the critical components of WD and how they contribute to the SNR enhancement. Then, we propose our ToA estimator in Section 4.4, outline the threshold selection criterion in Section 4.4, and compare its performance in both computer simulation and realistic UWB range measurements in Section 4.6. Finally, a summary is given in Section 4.7.

4.2 System Model

The position of a sensor node is directly related to the ToA of the first multipath component. To estimate the ToA, a UWB ranging system periodically transmits

sub-nanosecond pulses between the RN's and a TN of unknown distance. For a single pulse transmitted through free-space, the received signal at the RN under multipath can be modeled as

$$r(t) = \sum_{l=0}^{L-1} \alpha_l w(t - \tau_l) + n(t)\,, \tag{4.1}$$

where $w(t)$ is the received pulse template of duration T_p, α_l and τ_l are the amplitude and time delay of the l-th multipath, L is an unknown *a priori* which presents the number of propagation paths, and $n(t)$ is the additive white Gaussian noise (AWGN) with variance σ^2 to account for thermal noise. In (4.1), we model the channel as a tapped delay line where $\tau_l = \tau_0 + \widetilde{\Delta} l$, $\widetilde{\Delta}$ is the width of a time bin [18], and $\widetilde{\Delta}(L-1)$ is the dispersion of the channel. The purpose of ToA estimation is to accurately estimate the DP, i.e., τ_0, over an observation interval $[0, T)$, where $T \in [0, \widetilde{\Delta}(L-1))$. For the ease of analysis and simulation, we assume there are two channel conditions, with $\widetilde{\Delta} \geq T_p$ denoting a resolvable channel and $\widetilde{\Delta} < T_p$ indicating an unresolvable dense multipath channel with overlapping MPC's. Similar to [17, 20, 51, 53], we assume the transmission of an isolated pulse in (4.1), and the extension to multiple pulses is straightforward which can be done by averaging over multiple pulses, e.g., [18, 19].

Assuming T can be divided into K equally spaced delays for $k = 0, 1, \ldots, K-1$, each associating with a channel tap a_k. We can then simplify (4.1) by associating the set $\{a_k\}_{k=0}^{K-1}$ of channel coefficients with uniformly delayed received pulse template $w(t - k\Delta)$ for $k = 0, 1, \ldots, K-1$, as

$$r(t) = \sum_{k=0}^{K-1} a_k w(t - k\Delta) + n(t)\,. \tag{4.2}$$

Suppose the received signal is sampled at sampling time T_s. Given time instant

samples $t_i = (i-1)T_s$ for $i = 1, 2, \ldots, M$, (4.2) can be written as

$$r(t_i) = \sum_{k=0}^{K-1} a_k w(t_i - k\Delta) + n(t_i)\,, \quad i = 1, 2, \ldots, M\,, \tag{4.3}$$

which in matrix notation is given by

$$\mathbf{r} = \mathbf{W}\mathbf{a} + \mathbf{n} = \mathbf{s} + \mathbf{n}\,, \tag{4.4}$$

where $\mathbf{a} = [a_0, a_1, \ldots, a_{K-1}]^T$ and $\mathbf{n} = [n(t_1), n(t_2), \ldots, n(t_M)]^T$ are vectors of channel coefficients and the noise samples, respectively, $\mathbf{s} = \mathbf{W}\mathbf{a}$ is the signal portion of $\mathbf{r}$, and

$$\mathbf{W} = \begin{bmatrix} w(t_1) & w(t_1-\Delta) & \ldots & w(t_1-(K-1)\Delta) \\ w(t_2) & w(t_2-\Delta) & \ldots & w(t_2-(K-1)\Delta) \\ \vdots & \vdots & \ddots & \vdots \\ w(t_M) & w(t_M-\Delta) & \ldots & w(t_M-(K-1)\Delta) \end{bmatrix}, \tag{4.5}$$

represents a $M \times K$ matrix which comprises of delayed and sampled version of $w(t)$. In contrast to the matrix representations of [51] and [20], the step-size in (4.5) can be varied for the sake of estimation accuracy. Consequently, depending on Δ, the linear system in (4.4) can be either over or underdetermined.

4.2.1 LS Solution

We treat the ToA estimation as a by-product of the LS channel estimator by solving the solution to (4.4). For an overdetermined noiseless system there exists a unique solution which solves the problem

$$\min ||\mathbf{W}\mathbf{a} - \mathbf{r}||^2\,, \tag{4.6}$$

which yields the LS solution given by

$$\hat{\mathbf{a}}_{\mathrm{LS}} = (\mathbf{W}^T\mathbf{W})^{-1}\mathbf{W}^T\mathbf{r} = \mathbf{W}^{\perp}\mathbf{r}\,, \tag{4.7}$$

where $||\cdot||^2$ is the Euclidean norm, $(\cdot)^T$ denotes matrix transpose, $(\cdot)^{-1}$ is the matrix inverse, $\hat{\mathbf{a}}$ denotes an estimate of $\mathbf{a}$ and $\mathbf{W}^{\perp}$ is the Moore-Penrose inverse of $\mathbf{W}$. Unlike [20], $\mathbf{W}^{\perp}$ can be *pre-computed* and *stored* when a desired resolution Δ is given. For resolvable channels, i.e., $\widetilde{\Delta} \geq T_p$, the columns in $\mathbf{W}$ are independent, thus $\mathbf{W}$ is *well-conditioned* and (4.7) gives the maximum likelihood estimate (MLE) of $\mathbf{a}$. Unfortunately, (4.7) is often sensitive to noise in the received signal and can be quite unstable when $\mathbf{W}$ is *ill-conditioned*, e.g., in a dense multipath channel where $\widetilde{\Delta} < T_p$.

4.2.2 Regularized LS Solution

To find a meaningful result when the solution to (4.6) becomes unstable, we apply the technique of *regularization*. *Regularization* is a well-known technique for dealing with instability in the inverse problem [64] by forcing an ill-conditioned problem into a well-conditioned one with some *a priori* information. The RLS solution solves the problem

$$\min\{||\mathbf{W}\mathbf{a} - \mathbf{r}||^2 + \lambda||\mathbf{a}||^2\}\,, \tag{4.8}$$

where $\lambda \geq 0$ is the *regularization parameter* which controls the solution's energy. Note that with $\lambda = 0$ the solution to (4.8) reduces to the LS one. With $\lambda > 0$, it is straightforward to show that the unique global solution to (4.8) is given by

$$\hat{\mathbf{a}}_{\mathrm{RLS}} = (\mathbf{W}^T\mathbf{W} + \lambda\mathbf{I})^{-1}\mathbf{W}^T\mathbf{r} = \mathbf{W}_{\lambda}^{\perp}\mathbf{r}\,, \tag{4.9}$$

where $\mathbf{W}_{\lambda}^{\perp}$ is called the regularized pseudo-inverse, which can also be *pre-calculated* and *stored* for fast, on-the-fly processing. We note that in both (4.7) and (4.9), the resolution of $\hat{\mathbf{a}}$ depends entirely on parameter Δ in (4.5), with a smaller Δ incurring a higher resolution. More on the selection of parameters in Section 4.4.

We do not consider pulse distortion in modeling $w(t)$ for (4.7) and (4.9). However, calibration can be done in the system design and testing stage to find out $w(t)$ after going through the antennas. Nevertheless, the possible frequency dependent distortion on $w(t)$ caused by the wireless propagation environment will be hard to characterize [52]. The severity of the distortion depends on the frequency range of the pulse and the physical environment. In the case of slight mismatch between the template and the pulse shape, the effect on ToA estimation will not be substantial. Investigation on this issue is beyond the scope of the thesis.

4.3 Wavelet Denoising

To realize a stable LS solution for accurate ToA estimation, we apply the well-established technique of WD. Since its introduction in [58], denoising with DWT has become a powerful tool to recover noise corrupted data. To recover M samples of a known data sequence $\mathbf{s}$ from the noise-corrupted observation $\mathbf{r} = \mathbf{s} + \mathbf{n}$, where $\mathbf{n}$ denotes a $M \times 1$ vector samples of AWGN with variance σ^2, the purpose of WD is to differentiate the wavelet coefficients of $\mathbf{s}$ from those of $\mathbf{n}$, assuming the coefficients of $\mathbf{s}$ resides mostly in the low frequency region and can be compressed into a few large values in the wavelet domain. The wavelet denoising block of Fig. 4.1 illustrates this process. First, the compression is carried out with DWT by multiplying $\mathbf{r}$ with a

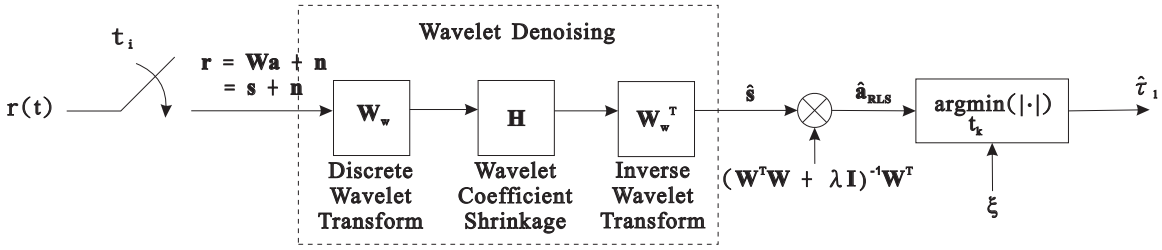

Figure 4.1: The RLS-WD ToA estimator and the WD processing block.

$M \times M$ orthonormal wavelet matrix $\mathbf{W}_W$, as

$$\begin{aligned} \mathbf{r}_W &= \mathbf{W}_W \mathbf{r} = \mathbf{W}_W \mathbf{s} + \mathbf{W}_W \mathbf{n} \\ &= \mathbf{s}_W + \mathbf{n}_W \,, \end{aligned} \tag{4.10}$$

where the matrix $\mathbf{W}_W$ can be *pre-determined* given the wavelet filter order F and decomposition level J [51, 59]. Due to the orthonormal property of $\mathbf{W}_W$, the noise is similarly mapped to $\mathbf{n}_W$ with identical statistics. However, because of the wideband nature of noise, the noise coefficients are usually small and can be discarded; whereas, the large coefficients of the desired signal are retained [58, 63].

Differentiating amongst these coefficients is identical to the filtering operation, where (4.10) is multiplied in the second stage by a matrix $\mathbf{H}$ modeled as

$$\mathbf{H} = \mathrm{diag}[h(1), h(2), \ldots, h(M)] \,. \tag{4.11}$$

The elements of $\mathbf{H}$ are set according to the thresholding criterion, with hard and soft thresholds from [63] being the most common, or the hyperbolic shrinkage proposed by Vidakovic [62] defined as

$$h(i) = \begin{cases} \sqrt{\left(1 - \frac{\delta^2}{|r_W(i)|^2}\right)} \,, & \text{if } |r_W(i)| > \delta \\ 0 \,, & \text{otherwise} \end{cases} \tag{4.12}$$

where $r_W(i)$ denotes the i-th element of $\mathbf{r}_W$, $|\cdot|$ is the absolute value operation, and δ is the threshold from [58, 63] given by

$$\delta = \sqrt{2\sigma^2 \log(M)} \,. \tag{4.13}$$

Finally, the recovery of the desired signal $\mathbf{s}$ is now given by

$$\hat{\mathbf{s}} = \mathbf{W}_W^T \tilde{\mathbf{r}}_W = \mathbf{W}_W^T \mathbf{H} \mathbf{W}_W \mathbf{r}\,, \tag{4.14}$$

which is the inverse DWT operation to the denoised wavelet coefficients $\tilde{\mathbf{r}}_W = \mathbf{H}\mathbf{r}_W$, where $\hat{\mathbf{s}}$ represents an estimate of $\mathbf{s}$, but with the noise significantly reduced. The process of discarding and retaining the wavelet coefficients results in the overall SNR enhancement.

4.4 RLS-WD ToA Estimator

The distinct advantage of UWB in ranging is its high precision with minimal penalty on SNR. Many existing ToA estimators, however, do not work well at the low SNR region, thus are limited to only short distance ranging. To improve the estimator accuracy under low SNR, we adopt wavelet denoising with RLS channel estimation as shown in Fig. 4.1 for a simple, yet accurate, ToA estimation. We name this the RLS-WD ToA estimator.

One drawback of denoising with DWT is the requirement of noise information, where its ability to remove noise depends entirely on how accurate the noise variance can be estimated. For narrowband signals and images which map to a few large, low-frequency coefficients in the wavelet domain, noise variance can be estimated from the finest scale wavelet coefficients [63]. However, due to the wideband characteristic of UWB, estimating variance from the first level decomposition is often incorrect. For that, assuming a large distance between nodes and a large sample size M, the variance can be estimated from the first few hundred noise samples as

$$\hat{\sigma}^2 = \frac{1}{N-1} \sum_{i=1}^{N} (r(t_i) - \hat{\mu})^2\,, \tag{4.15}$$

where $\hat{\mu}$ is the sample mean and N a subset of M. The noise only region for estimating the noise variance by (4.15) can be double checked after a range estimate is obtained. Table 4.1 outlines the RLS-WD ToA estimator. To summarize, the RLS-WD algorithm has three parameters to determine: threshold ξ, estimation resolution Δ, and the regularization parameter λ. The parameter Δ is a system design parameter that determines the trade-off between accuracy and complexity. The system requirements mandate the selection of Δ. The parameter λ can be selected according to the cross-validation method [65] or the Miller criterion [66], whereas in our simulation we find its choice rather robust to channel conditions, the Δ values and the constant ξ. The threshold ξ will be studied in the next section.

1.	receive M samples of observation $\mathbf{r}$ at sampling rate T_s over the interval $[0, T)$;
2.	estimate the noise variance $\hat{\sigma}^2$ according to (4.15);
3.	select the wavelet filter order F and WD decomposition level J, apply Daubechies DWT and Vidakovic hyperbolic shrinkage to $\mathbf{r}$, and estimate the desired signal according to (4.14);
4.	choose the channel estimator resolution Δ, and $K = T/\Delta$, construct $\mathbf{W}$ according to (4.5);
5.	estimate the channel $\hat{\mathbf{a}}$ using either LS solution in (4.7), or RLS algorithm in (4.9), with a pre-determined λ;
6.	estimate the ToA as $$\hat{\tau}_0 = \arg\min_{t_k} |\hat{\mathbf{a}}| > \xi \,, \qquad (4.16)$$ where $\xi = \eta \hat{a}_{max}$ is the threshold, $\eta \in (0, 1)$ is the normalized threshold relating to a percentage of $\hat{a}_{max} = \max\{|\hat{\mathbf{a}}|\}$, the maximum estimated amplitude.

Table 4.1: The RLS-WD ToA estimator.

4.5 Threshold Selection for RLS-WD Estimator

The threshold selection plays a crucial role in the overall estimator performance. Especially in a dense multipath channel, a threshold too low can increase the chance that the noise samples prior to the true ToA being falsely identified as the ToA [17], i.e., the early false alarm probability P_{FA}. Conversely, it is possible to miss the true ToA and detect the later arriving MPC's as the ToA when a threshold is set too high, thus increasing the probability of a missed detection P_M [17].

In this section, we devise a framework for threshold selection according to the NP criterion [67], one which selects a threshold according to a constant false alarm probability. For the tractability of analysis, we assume: 1) the noise samples are independent and identically distributed (i.i.d.) Gaussian random variables (r.v.'s) with zero mean and variance σ^2, and 2) the columns of $\mathbf{W}$ in (4.5) are orthonormal basis functions, i.e., $\mathbf{w}_{i'}^T\mathbf{w}_{j'} = 0, i' \neq j'$, and $\mathbf{w}_{i'}^T\mathbf{w}_{i'} = 1, \forall i' = 0, 1, \ldots, K-1$, where $\mathbf{w}_{i'}$ denotes the i'-th column of $\mathbf{W}$, implying resolvable MPC's, i.e., $\widetilde{\Delta} \geq T_p$ in (4.1), and unit energy pulses. Fig. 4.2 illustrates the concept of P_{FA} and P_M, where the uncertainty region T is divided into K equally spaced slots prior to LS estimation. We further assume that the DP to arrive uniformly within the first half of T at index $j \in [0, J'-1]$ where $J' = K/2$, there is no signal present for $0 \leq i' \leq j-1$ and both signal and noise exist thereafter. As shown in Fig. 4.2, if $\xi = \xi_1$ then it is possible to erroneously declare noise samples prior to j as the ToA when (4.16) is used as the estimator, thus causing a false alarm. On the contrary, if $\xi = \xi_2$ then a missed detection of DP is probable since we would declare later arriving MPC's as the ToA. In what follows, we will derive both P_{FA} and P_M and show how they can be used to determine an appropriate ξ.

With the orthonormal columns in $\mathbf{W}$, the i'-th sample output $\hat{a}_{i'}$ of the LS channel

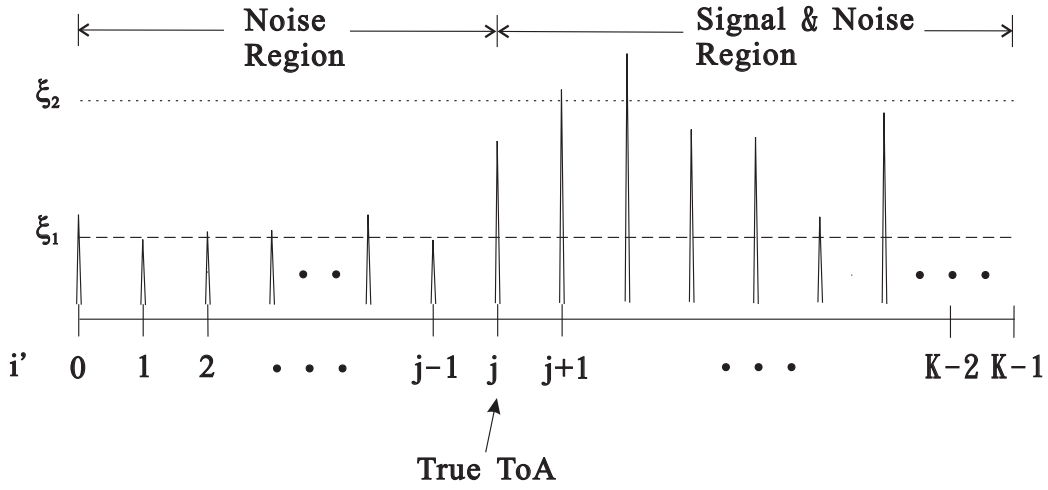

Figure 4.2: An illustration on the impact of threshold selection for the RLS-WD ToA estimator.

estimator[1] can be written as

$$\hat{a}_{i'} = \mathbf{w}_{i'}^T \mathbf{w}_{i'} a_{i'} + \mathbf{w}_{i'}^T \mathbf{n} = a_{i'} + \sum_{i=1}^{M} w(t_i - i'\Delta') n(t_i) = a_{i'} + n_{i'} \,, \tag{4.17}$$

where $\hat{a}_{i'}$ is the MLE of $a_{i'}$, $\Delta' = \lfloor T_p/T_s \rfloor$ is the number of delay samples in between pulses to achieve orthogonality, and $\lfloor \cdot \rfloor$ denotes the floor function. Clearly, $\hat{a}_{i'} \sim \mathcal{N}(a_{i'}, \sigma^2), \forall i' = 0, 1, \ldots, K-1$, is a set of independent but non-identically distributed Gaussian r.v.'s[2]. When the sample $\hat{a}_{i'}$ undergoes the absolute value operation in (4.16), the probability density function (p.d.f.) of $y_{i'} = |\hat{a}_{i'}|$ can be written as [68]

$$f_{Y_{i'}}(y_{i'}) = \begin{cases} 0 \,, & \text{if } y_{i'} < 0 \\ \frac{1}{\sqrt{2\pi\sigma^2}} \left[\exp\left(-\frac{(y_{i'} - a_{i'})^2}{2\sigma^2} \right) + \exp\left(-\frac{(-y_{i'} - a_{i'})^2}{2\sigma^2} \right) \right] \,. & \text{if } y_{i'} \geq 0 \end{cases} \tag{4.18}$$

Therefore, following (4.18), the threshold of (4.16) with $y_{max} := \hat{a}_{max} = \max\{y_{i'}\}$, for $i' = 0, 1, \ldots, K-1$, can be formulated as the order statistics [68] with the p.d.f. given as

$$\begin{aligned} f_{Y_{max}}(y_{max}) &= \sum_{i''=0}^{K-1} f_{Y_{i''}}(y_{max}) \prod_{j'' \neq i'', \, j''=0}^{K-1} F_{Y_{i''}}(y_{max}) \\ &= \sum_{i''=0}^{K-1} \frac{1}{\sqrt{2\pi\sigma^2}} \times \\ &\quad \left[\exp\left(-\frac{(y_{max} - a_{i''})^2}{2\sigma^2} \right) + \exp\left(-\frac{(-y_{max} - a_{i''})^2}{2\sigma^2} \right) \right] \times \\ &\quad \prod_{j'' \neq i'', \, j''=0}^{K-1} \left(Q\left(\frac{a_{i''} - y_{max}}{\sigma} \right) - Q\left(\frac{a_{i''} + y_{max}}{\sigma} \right) \right) \,, \end{aligned} \tag{4.19}$$

[1]The RLS channel estimator output can be treated as a special case of LS channel estimator, where $\lambda \neq 0$ in (4.9). The use of RLS is only necessary when the columns of $\mathbf{W}$ are not orthonormal.

[2]In the case when columns of $\mathbf{W}$ are not necessary orthonormal, i.e., $\mathbf{w}_{i'}^T \mathbf{w}_{j'} \neq 0, i' \neq j'$, we can stack the K elements of $\hat{a}_{i'}$ into vector $\hat{\mathbf{a}} = [\hat{a}_0, \hat{a}_1, \ldots, \hat{a}_{K-1}]^T$. The elements of $\hat{\mathbf{a}}$ is then correlated and non-identically distributed Gaussian random variable with mean $\mathbb{E}\{\hat{\mathbf{a}}\} = \mathbf{a}$ and covariance $\mathrm{Cov}(\hat{\mathbf{a}}) = \sigma^2(\mathbf{W}^T\mathbf{W})^{-1}$, assuming $\mathbf{W}^T\mathbf{W}$ has a full-rank.

where $f_{Y_{i''}}(y_{max})$ and $F_{Y_{i''}}(y_{max})$ are the p.d.f. and cumulative distribution function (c.d.f.) of $y_{i''}$ evaluated at y_{max}, respectively, and $Q(x) \triangleq \int_x^{+\infty} \frac{1}{\sqrt{2\pi}} e^{-t^2/2}\,\mathrm{d}t$ is the Gaussian tail Q-function. We define P_{FA} conditioned on j, $P_{FA}(j)$, as the probability that the i'-th sample of the LS channel estimator output crossing threshold ξ for i' smaller than a given j, which can be written as

$$\begin{aligned}
P_{FA}(j) &= \Pr\{y_{i'} > \xi, \text{ for any } i' = 0, 1, \ldots, j-1\} \\
&= 1 - \Pr\{y_{i'} < \eta y_{max},\, \forall i' = 0, 1, \ldots, j-1\} \\
&= 1 - \prod_{i'=0}^{j-1} \left(1 - \int_0^{+\infty} \int_{\eta y_{max}}^{+\infty} f_{Y_{i'}, Y_{max}}(y_{i'}, y_{max})\,\mathrm{d}y_{i'}\,\mathrm{d}y_{max}\right) \\
&= 1 - \prod_{i'=0}^{j-1} \times \\
&\left(1 - \int_0^{+\infty} \int_{\eta y_{max}}^{+\infty} f_{Y_{i'}|Y_{max}}(y_{i'}|y_{max}) f_{Y_{max}}(y_{max})\,\mathrm{d}y_{i'}\,\mathrm{d}y_{max}\right),
\end{aligned} \tag{4.20}$$

where $f_{Y_{i'}, Y_{max}}(y_{i'}, y_{max})$ and $f_{Y_{i'}|Y_{max}}(y_{i'}|y_{max})$ are the joint and conditional p.d.f.'s, respectively, of the r.v.'s $y_{i'}$ and y_{max}, and we have applied the Bayes' Theorem in the last step of (4.20). Substituting (4.18) into (4.20) gives

$$P_{FA}(j) = 1 - \prod_{i'=0}^{j-1} \left(1 - \int_0^{+\infty} g(a_{i'}, \eta y_{max}) f_{Y_{max}}(y_{max})\,\mathrm{d}y_{max}\right), \tag{4.21}$$

$$g(a, b) = \left(1 - Q\left(\frac{a-b}{\sigma}\right) + Q\left(\frac{a+b}{\sigma}\right)\right). \tag{4.22}$$

For the ToA which arrives at the j-th index, i.e., $a_{i'} = 0$ for $0 \le i' \le j-1$, (4.21) simplifies to

$$P_{FA}(j) \cong 1 - \left(1 - 2\int_0^{+\infty} Q\left(\frac{\eta y_{max}}{\sigma}\right) f_{Y_{max}}(y_{max})\,\mathrm{d}y_{max}\right)^j, \tag{4.23}$$

which can be averaged over $f_J(j)$ to obtain P_{FA}. According to the CFA criterion,

we can set P_{FA} to a constant and look for η by inverting the averaged expression. This is not pursued here due to the complexity of inverting averaged (4.23) with the evaluation of (4.19). Instead, we consider a simplified scenario where ξ is set as a fixed threshold, then following the above formulation $P_{FA}(j)$ can be written as

$$P_{FA}(j) = 1 - \prod_{i'=0}^{j-1} \left(Q\left(\frac{a_{i'} - \xi}{\sigma}\right) - Q\left(\frac{a_{i'} + \xi}{\sigma}\right)\right) \cong 1 - \left(1 - 2Q\left(\frac{\xi}{\sigma}\right)\right)^{j}, \quad (4.24)$$

which can be averaged over the uniformly distributed j to obtain P_{FA} as

$$P_{FA} = \mathbb{E}\{P_{FA}(j)\} = 1 - \left[\frac{1 - (1 - 2Q\left(\frac{\xi}{\sigma}\right))^{J'}}{2J'Q\left(\frac{\xi}{\sigma}\right)}\right]. \quad (4.25)$$

Following the CFA, we can obtain ξ by inverting the right-hand side of (4.25) according to a target P_{FA}. Alternatively, we may set a specific P_{FA} range then find a threshold which gives a satisfactory P_M, or look for a threshold which minimizes the sum of P_{FA} and P_M [17]. For these threshold selection strategies, we define $P_M(j, \mathbf{a})$ as the probability that the true ToA is missed and a false detection on any of the later $K - j - 2$ samples conditioned on j and a particular channel realization $\mathbf{a}$, as

$$\begin{aligned} P_M(j, \mathbf{a}) &= \Pr\{y_{i'} < \eta y_{max},\, \forall i' = 0, 1, \ldots, j \cap \\ &\qquad y_{i'} > \eta y_{max}, \text{ for any } i' = j+1, j+2, \ldots, K-1\} \\ &= \prod_{i'=0}^{j} \Pr\{y_{i'} < \eta y_{max}\}(1 - \Pr\{y_{i'} < \eta y_{max},\, \forall i' = j+1, j+2, \ldots, K-1\}). \end{aligned} \quad (4.26)$$

And continuing in a manner similar to the derivations of (4.20), we get

$$
\begin{aligned}
P_M(j,\mathbf{a}) = &\prod_{i'=0}^{j}\left(1-\int_0^{+\infty} g(a_{i'},\eta y_{max}) f_{Y_{max}}(y_{max})\,\mathrm{d}y_{max}\right)\times \\
&\left[1-\prod_{i'=j+1}^{K-1}\left(1-\int_0^{+\infty} g(a_{i'},\eta y_{max}) f_{Y_{max}}(y_{max})\,\mathrm{d}y_{max}\right)\right] \\
&\cong \left(1-2\int_0^{+\infty} Q\left(\frac{\eta y_{max}}{\sigma}\right) f_{Y_{max}}(y_{max})\,\mathrm{d}y_{max}\right)^{j}\times \\
&\left(1-\int_0^{+\infty} g(a_j,\eta y_{max}) f_{Y_{max}}(y_{max})\,\mathrm{d}y_{max}\right)\times \\
&\left[1-\prod_{i'=j+1}^{K-1}\left(1-\int_0^{+\infty} g(a_{i'},\eta y_{max}) f_{Y_{max}}(y_{max})\,\mathrm{d}y_{max}\right)\right], \qquad (4.27)
\end{aligned}
$$

where the last step stems from the assumption that there exists no signal for $0 \le i' < j$. Likewise to the evaluation of (4.21) or (4.23), looking for η which minimizes (4.27) has no closed form solution due to the p.d.f. of y_{max}. However, one can easily resort to numerical integration of (4.27), which involves products of the single integrals with elementary Q-functions as integrand. Next, we consider a fixed threshold ξ so that the $P_M(j,\mathbf{a})$ can be simplified to

$$
\begin{aligned}
P_M(j,\mathbf{a}) &= \prod_{i'=0}^{j}\Pr\{y_{i'}<\xi\}\times\left(1-\prod_{i'=j+1}^{K-1}\left(1-\Pr\{y_{i'}>\xi\}\right)\right) \\
&\cong \left(1-2Q\left(\frac{\xi}{\sigma}\right)\right)^{j}\times\left(Q\left(\frac{a_j-\xi}{\sigma}\right)-Q\left(\frac{a_j+\xi}{\sigma}\right)\right)\times \\
&\quad\left(1-\prod_{i'=j+1}^{K-1}\left(Q\left(\frac{a_{i'}-\xi}{\sigma}\right)-Q\left(\frac{a_{i'}+\xi}{\sigma}\right)\right)\right). \qquad (4.28)
\end{aligned}
$$

After averaging over both j and $\mathbf{a}$, (4.28) can be evaluated with ξ from (4.25) when a particular P_{FA} is chosen, or minimizing the sum of P_{FA} and P_M for a specific ξ. Table 4.2 outlines our threshold selection framework that is based on the CFA criterion [67]. The performance of this framework will be quantified by simulation in

Section 4.6.1.

1.	set P_{FA} to a predefined value;
2.	compute ξ from (4.25) with $\hat{\sigma}$ according to (4.15);
3.	use ξ to estimate the ToA in (4.16);
4.	if both $\hat{j}$ and $\hat{\mathbf{a}}$ are known, compute P_M according to (4.28).

Table 4.2: A threshold selection framework based on the constant P_{FA} criterion.

4.6 Results

We compare the performance of the RLS-WD with both the ED [19], and the high-resolution PDB estimators [20]. Brief descriptions of the estimators are as follows. The ToA estimator in [19] confines τ_0 to within $0 \leq \tau_0 < T$. This interval is divided into segments of size Δ_{ed}, i.e., $[(n-1)\Delta_{\text{ed}}, n\Delta_{\text{ed}})$ for $n = 1, 2, \ldots, \lfloor T/\Delta_{\text{ed}} \rfloor$, where $\lfloor \cdot \rfloor$ is the floor function, and the energy of on each segment is measured. The energy from the n-th interval is given by

$$z[n] = \int_{(n-1)\Delta_{\text{ed}}}^{n\Delta_{\text{ed}}} r^2(t)\,\mathrm{d}t\,.$$

Now, $z[n]$ is compared to a threshold θ and the index $\hat{n}$ of first crossing is chosen as the ToA estimate, i.e., $\hat{\tau}_0 = (\hat{n} - 0.5)\Delta_{\text{ed}}$, where the threshold θ is defined a function of the minimum and maximum values of $z[n]$ as

$$\theta = \min\{z[n]\} + K_{\text{ed}}[\max\{z[n]\} - \min\{z[n]\}]\,. \tag{4.29}$$

The PDB estimators in [20] has three types, namely, single search (SS1), search and subtract (SS2), search subtract and readjust (SSR). These estimators first compute the discrete MF output between $\mathbf{r}$ and a sampled $w(t)$; thereafter, the selection

of the maximum peaks from the output according to a threshold criterion, usually a fixed threshold [20]. For SS1, up to Z peaks are selected simultaneously; whereas, both SS2 and SSR select up to Z peaks over Z MF computations with previously selections being removed from $\mathbf{r}$ prior to the z-th MF calculation. Moreover, SSR differs from SS2 in that the estimated channel gains are readjusted according to the previous estimates. Details of the PDB algorithms can be found in [20]. Performance is examined in three ways, i.e., via simulation, with realistic indoor measurement data, and via a complexity analysis.

4.6.1 Simulation

We evaluate the performance by computer simulation in MATLAB$^{\text{TM}}$ with the Uvi Wave software package [69] for Daubechies DWT. To accurately examine the performance under multipath, we use the CM3 channel model from IEEE 802.15.3a [8], which models an office NLOS environment. The received template $w(t)$ is assumed to be a Gaussian doublet [5] with pulse parameter $\tau_m = 0.6$ ns, which has a zero-to-zero pulse width of 2 ns, and $T_s = 0.1$ ns.

To determine the most suitable F for WD, we plot the output SNR as F varies for a fixed input SNR[3] of 0 dB in Fig. 4.3. As shown, by applying WD to the received signal we can have close to 4 dB gain across all F. Since increasing F has no effect on the output SNR, we may further reduce the denoising complexity by selecting the smallest F before performance tapers off. For $F = 8$, Fig. 4.3 illustrates the effectiveness of WD[4] as the input SNR varies. We see that WD results in substantial gain at low SNR before diminishing return at high SNR. However, when considering long distance ranging, the performance at low SNR is often of great interest. For the

[3]The output and input SNR are defined as $\text{SNR}_{\text{out}} = 20\log_{10}(||\mathbf{s}||/||\hat{\mathbf{s}} - \mathbf{s}||)$ and $\text{SNR}_{\text{in}} = 20\log_{10}(||\mathbf{s}||/||\mathbf{n}||)$, respectively, where $||\cdot||$ denotes the Frobenius matrix norm [60]. In all of the later simulations, we set the SNR according to this SNR_{in} definition.

[4]The effectiveness of WD can be measured from the gain in SNR, i.e., $\text{SNR}_{\text{out}} - \text{SNR}_{\text{in}}$.

ease of simulation, σ^2 in (4.13) is assumed to be perfectly known, hence the results shown act as a lower bound. However, in the next section we show that even when the noise variance is estimated with (4.15), the gain of denoising at low SNR is still substantial.

We demonstrate the threshold selection framework described in Table 4.2 for $P_{FA} = 10^{-3}$ and 10^{-4}. We let $T = 160$ ns so τ_0 is uniformly distributed from 0 to 80 ns, and assume $\widetilde{\Delta} \geq T_p$ such that $\Delta = T_p$ and $\lambda = 0$. The simulation is performed over 100 channel realizations with a thousand independent noise trials per realization. Fig. 4.4 shows the root mean-squared error (RMSE) as SNR varies for different threshold settings. Clearly, threshold selection according to CFA criterion outperforms that of the fixed threshold when $\xi = 0.05 y_{max}$. The figure also shows the robustness of WD when combined with RLS to outperform that of the plain RLS, irrespective of the threshold selection strategy. We would like to stress that comparing between CFA (lines marked with $\triangle$) and fixed threshold selection (lines marked with $\bigcirc$) on the RLS-WD, the use of CFA framework may not be necessary if a minor performance loss can be tolerated. The adaptation of CFA framework requires solving (4.25), thus in the event of a simple estimator one may resort to a simple fixed threshold. In Fig. 4.4, we plot the average P_M as a function of the SNR for the simulation of Fig. 4.4. As shown, the average P_M decreases monotonically over the entire SNR region even when we use the CFA framework, and RLS exhibits lower P_M than RLS-WD. In contrast, the performance degradation of a fixed threshold is complemented by a small P_M at low SNR that increases and eventually saturates at a value close to the CFA case, and a small ξ tends to have a smaller P_M since it is less likely to miss a detection but more prone to a false alarm. We have confirmed these trends with the actual counting of misses. From the figures, we notice that although the CFA framework makes no attempt to minimize P_M, its averaged P_M is still low

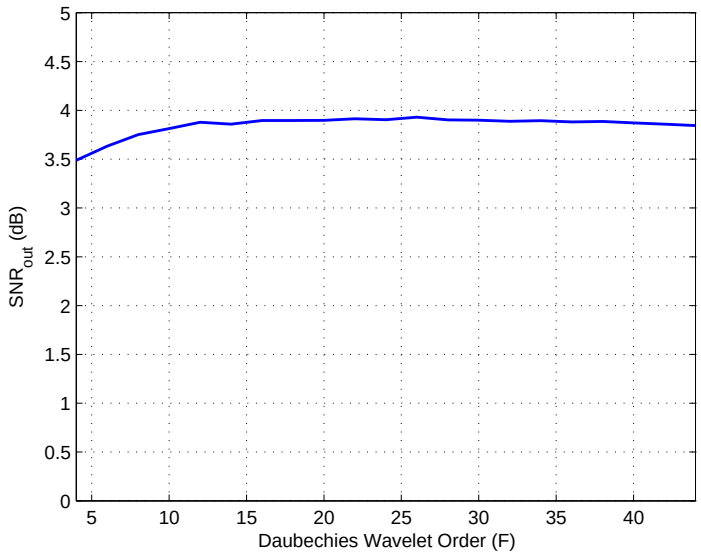

(a) SNR of denoised signal as F varies for 0 dB input SNR

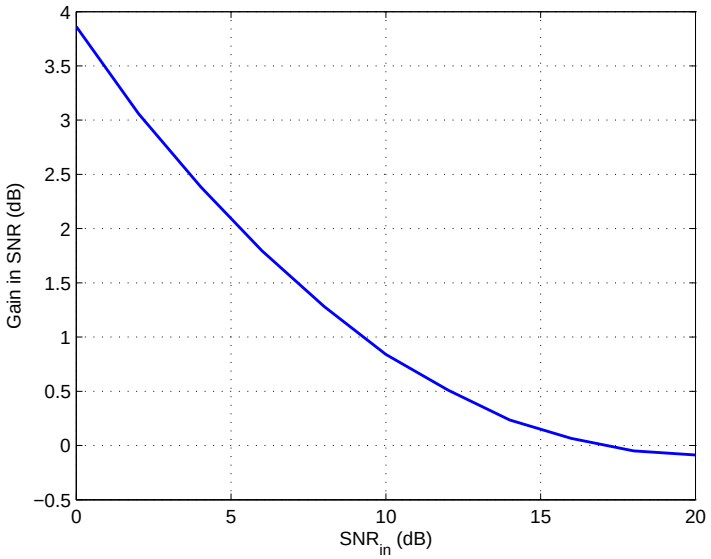

(b) Gain in SNR as a function of input SNR for $F = 8$

Figure 4.3: Denoising performance of Daubechies DWT for UWB-IR.

enough to be useful.

Upon the threshold selection according to CFA, we now compare the estimator performance to other estimators, as well as the CRLB for ToA estimation defined in [7]. Fig. 4.5 illustrates the RMSE as a function of SNR. For ED, we let K_{ed} in (4.29) vary until a satisfactory RMSE over the entire SNR range is obtained. For the ease of simulation runtime, the number of peaks to detect Z for PDB is set to 100, and we assume a fixed threshold selection criterion for the PDB algorithms since they have no known optimal threshold selection strategy [20]. As shown, RLS-WD with CFA framework at $P_{FA} = 10^{-3}$ clearly supersedes both the ED and PDB estimators over all SNR. Furthermore, since none are efficient estimator, their performance are quite far away from the CRLB. The investigation of efficient ToA estimator is beyond the scope of this research.

To examine the high-resolution capability of the RLS-WD, we compare it to other estimators while Δ is set as a multiple of T_s when constructing $\mathbf{W}$, and assume unresolvable dense multipath channel, i.e., $\widetilde{\Delta} < T_p$. We use a fixed threshold criterion for both PDB and RLS-WD algorithms, and let $T = 64$ ns. Fig. 4.6 shows the RMSE versus SNR when $\xi = 0.05 y_{max}$, with both RLS and RLS-WD evaluated at $\lambda = 2$, and $\Delta = 2T_s$, PDB at $Z = 100$, and ED with $\Delta_{\text{ed}} = T_p, K_{\text{ed}} = 0.0129$. Clearly, the RLS-WD algorithm outperforms the ED estimator under all SNR, and the gain in performance comparing to plain RLS is quite significant. At low SNR, RLS-WD performs better due to the input SNR enhancement from WD; whereas, at high SNR, the contribution from WD lessens. When comparing with the PDB algorithms, the RLS-WD performs better at low SNR with a diminishing return at high SNR. However, as we shall see in Section 4.6.3, the PDB algorithms necessitate high complexity, and when a simple estimator is desired the RLS-WD is often the best choice. In Fig. 4.6, we compare between RLS and RLS-WD with $\Delta = 2T_s, 4T_s, 8T_s$.

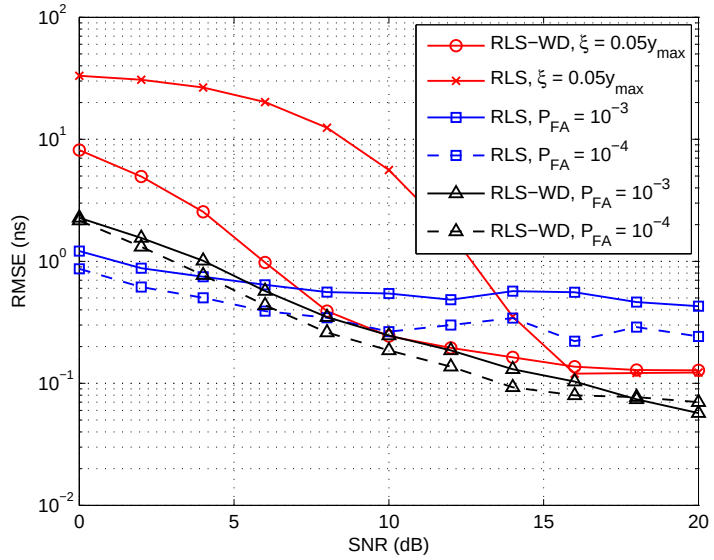

(a) RMSE as a function of SNR

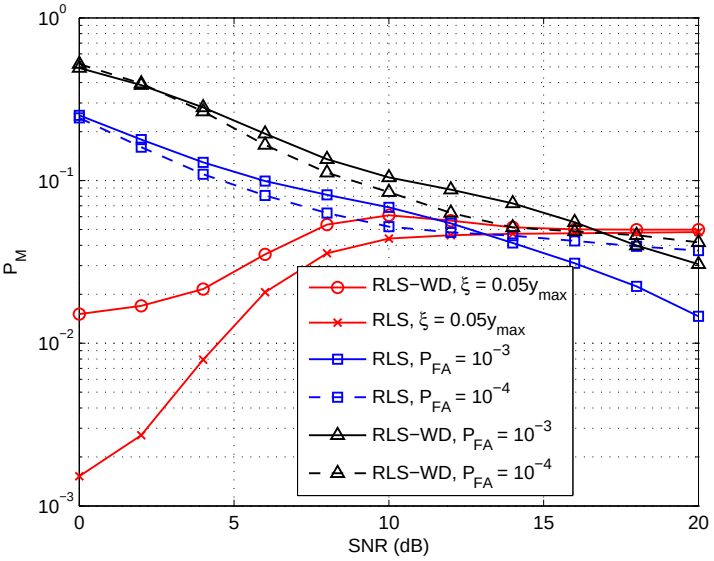

(b) Average P_M as SNR varies

Figure 4.4: RMSE and average P_M as a function of SNR for both CFA threshold selection framework and a simple fixed threshold in resolvable channel, i.e., $\widetilde{\Delta} \geq T_p$.

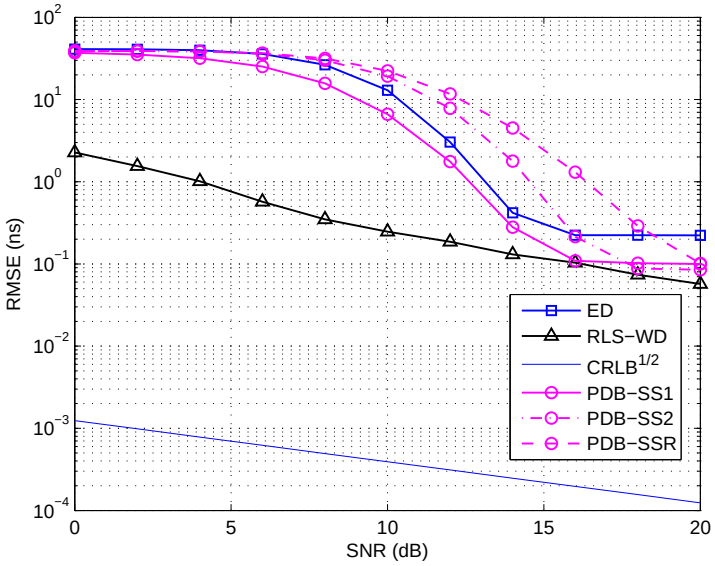

Figure 4.5: RMSE of ToA estimation as SNR varies for different algorithms in resolvable channel, i.e., $\widetilde{\Delta} \geq T_p$. The simulation parameters are: for ED, $\Delta_{\text{ed}} = T_p/2$ with $K_{\text{ed}} = 0.0077$, for the PDB estimators, $\zeta = 0.05 y_{max}$ and $Z = 100$, and, for RLS-WD with CFA, $P_{FA} = 10^{-3}$.

An interesting observation is the identical performance for $\Delta = 4T_s$ and $8T_s$, which depending on the storage requirement we may choose either one without sacrificing the overall performance. And, if a little degradation can be tolerated, one can simply let $\Delta > 2T_s$. Once again, we stress on the importance of performance gain at low SNR that is more crucial in ranging applications. Altogether, Figs. 4.5 and 4.6 demonstrate the robustness of our estimator for possible deployment in WSN applications.

4.6.2 Propagation Measurements

We evaluate the four algorithms under the realistic application of indoor ranging with the UWB measurements from [17]. A short description of the experiment and the application of WD to the measured data is given in Appendix A.

Fig. 4.7 compares the range estimation errors at each location of Fig. A.1 for a fixed $\xi = 0.1y_{max}$, between (a) the different PDB algorithms with an optimized Z, and (b) the RLS-WD with different Δ. The error is computed as the difference between the estimated and measured ToA, assuming there exists a clear LOS path between the TX and RX for the DP signal [17]. As shown, optimizing Z for the PDB algorithms significantly reduces the range estimation error at short distances. Despite the optimization, PDB-SS1 always produces the worst performance at long distances followed by the PDB-SS2 and the PDB-SSR, as in agreement with the simulation results of Section 4.6.2, which is due to the inaccuracy in delay estimation with the picking of Z largest peaks after only one MF correlation; whereas, both PDB-SS2 and PDB-SSR readjust their delays at each iteration for an improved accuracy. Altogether, we see that the RLS-WD performs better for most cases at long distances, and can perform better or equal to that of the PDB algorithms at short distances. We would like to stress that whereas one may need to switch between different PDB algorithms for the best performance under all circumstances, we would only need to

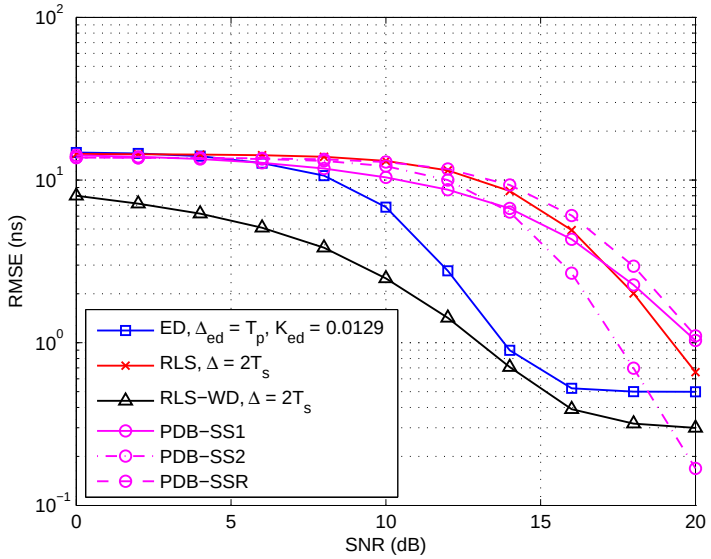

(a) Comparison between other algorithms

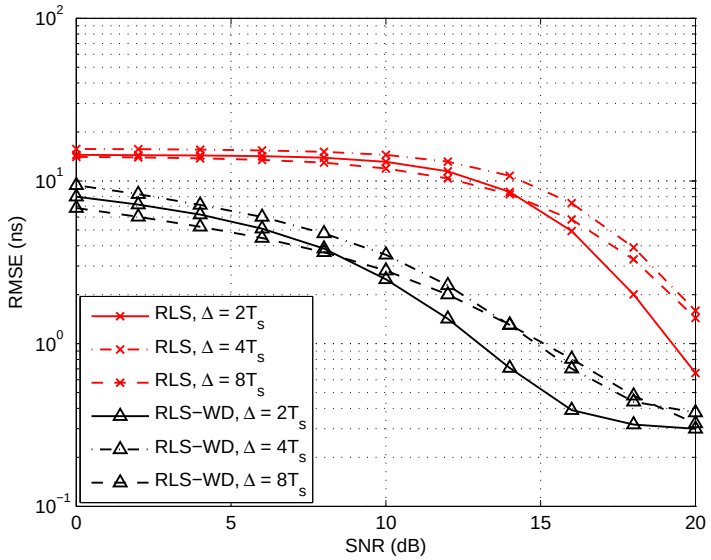

(b) Comparison with RLS only

Figure 4.6: RMSE of ToA estimation as SNR varies for different algorithms in unresolvable dense multipath channel, i.e., $\widetilde{\Delta} < T_p$. The simulation parameters are: all estimators except ED set $\xi = 0.05 y_{max}$, and $Z = 100$ for PDB type estimators.

store $\mathbf{W}$ in a memory bank for rapid signal processing. As noted in [17], the large errors at long distances are mostly caused by a combination of the complex LOS blockage and a systematic error in distance measurement, the investigation of which is beyond the scope of this thesis.

Finally, we illustrate the effect of a varying T has on the range estimation error in Fig. 4.8 for a fixed $\xi = 0.1y_{max}$ and measurement at location 15, depicting a severe NLOS environment, with $\tau_0 \approx 103.65$ ns. As we shall see in the next section, the observation window T plays a crucial role in determining the overall system complexity since it governs the number of samples to process in both the MF calculation and WD. With $Z = 100$, the PDB algorithms tend to produce significant errors when T is small such that the estimated channel taps fall into the noise region. In contrast, due to the linear model assumption, the RLS-WD does not have this problem and can better estimate the DP arrival even with a small T, e.g., $T < 150$ ns. This characteristic is similarly observed at all other locations. Therefore, comparing to its counterparts, the processing time of the RLS-WD can be dramatically reduced since we would only need to include the samples until the DP arrival, but nothing after.

4.6.3 Complexity Analysis

The computational load of the RLS-WD is fairly constant since most of the matrix operations in (4.5), (4.7), and (4.9) can be done beforehand. Specifically, the RLS is equivalent to LS over a sphere and its complexity is about $4M^2K+22K^3$ flops [70] with the remaining load in DWT, which is of $\mathcal{O}(M)$ per WD process [71]. However, when recognizing the WD as a series of matrix multiplications in (4.14) with *pre-computed* matrices further indicates a constant processing time for our approach. In contrast, the complexity of the PDB estimators depends entirely on the channel condition and the number of iterations Z. Table 4.3 compares the flop count amongst the algorithms.

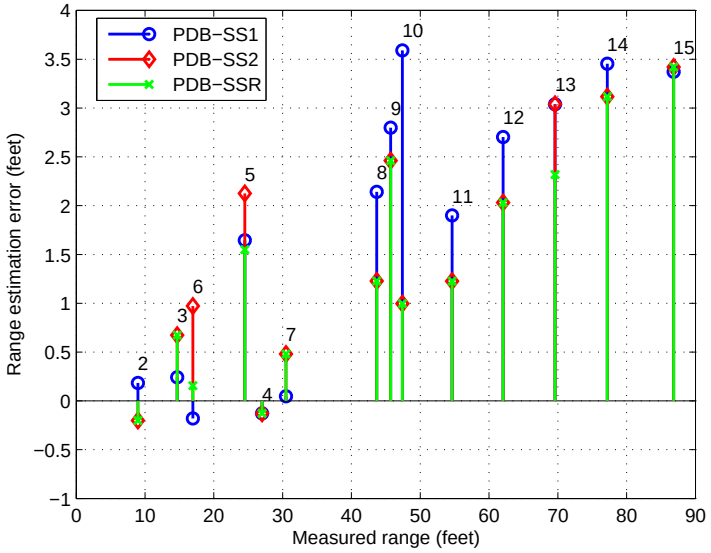

(a) PDB algorithms

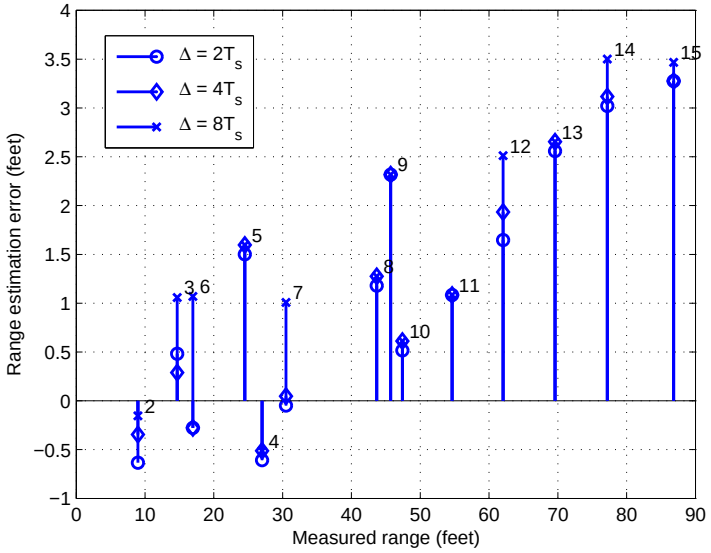

(b) RLS-WD algorithm with different Δ

Figure 4.7: Comparison of the range estimation errors between the different algorithms with a fixed $\xi = 0.1y_{max}$ at the locations in Fig. A.1. For the PDB algorithms, the minimum error has been optimized according to Z and the RLS-WD is evaluated with different Δ and $\lambda = 2$. The error is calculated as the difference between the estimated and measured ranges, assuming the direct-path signal arrives via a clear LOS path between the TX and RX.

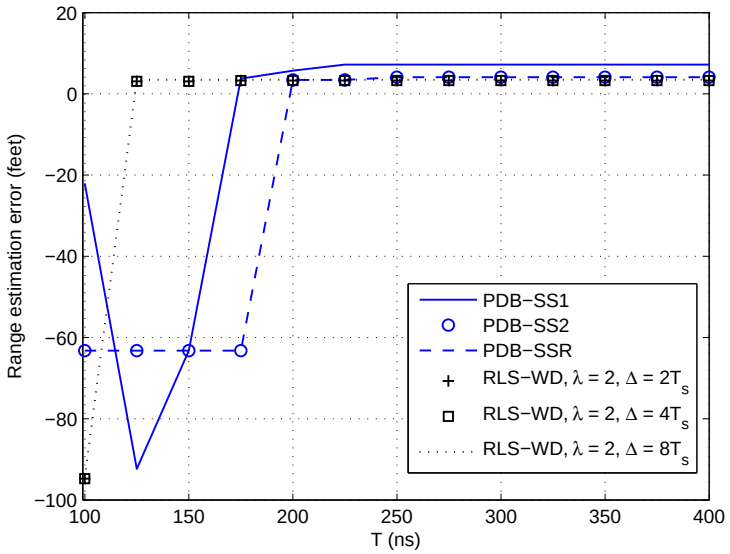

Figure 4.8: Comparison of range estimation error as observation window T varies in step of 25 ns from 100 ns to 400 ns between the algorithms for the measurement taken at location 15. The parameters are $\xi = 0.1y_{max}$, $\lambda = 2$, $F = 8$ and $Z = 100$.

For the PDB algorithms, ignoring the peak finding operations after the MF output, they require $4zM^2$ flops per MF computation, $5zM$ and $2z^2M + 2z^3/3 + 2zM$ flops to compute the channel gain per iteration for PDB-SS2 and PDB-SSR, respectively, where z denotes the iteration index. Hence, in a dense multipath channel, the RLS-WD would require less processing time than its counterparts.

	Flop Count
PDB-SS1	$4M^2$
PDB-SS2	$4ZM^2 + 5ZM$
PDB-SSR	$4ZM^2 + 4ZM + \mathcal{O}(Z^4)$
RLS-WD	$(4M^2K + 22K^3) + 4FJM$

Table 4.3: Comparison of computational complexity between different ToA algorithms.

4.7 Conclusion

In this chapter, we have proposed the RLS-WD ToA estimator, which estimates the ToA as a by-product of the RLS channel estimator based on a thresholding technique. Our approach is simple and can provide fast, on-the-fly, accurate ToA estimation applicable to real-time ranging system. Unlike the majority of the previous works, we have quantified the robustness of our algorithm by computer simulation and the processing of realistic indoor UWB ranging measurements. In both cases, when sampling rate is available, our approach is shown to outperform other algorithms in both ToA estimation and computational complexity, and its performance can be further improved with the selection of threshold according to the CFA criterion. We envision that the RLS-WD will be an indispensable part of a real-time system when the instantaneous position estimate of a TN in a WSN is in high demand.

Chapter 5

Low-Complexity Ultra-Wideband Maximum Likelihood Channel Estimation via Basis Projection

5.1 Background

In Chapter 2, we have outlined the pros and cons of the Rake receiver, which ultimately rests on obtaining accurate channel state information (CSI). Although there are other alternatives to estimate the CSI, the ML estimator is by far the only one which can produce unbiased estimates [49, 50]. Unfortunately, ML channel estimation for UWB-IR necessitates high-rate samples [23]. Similarly, the RLS-WD estimator introduced in Chapter 4 also operates on Nyquist-rate samples. To alleviate the burden of acquiring Nyquist-rate samples, we propose a low-complexity (LC)-ML channel estimator that adopts the compression framework of compressed sensing (CS) for sampling rate reduction while retaining the noise statistics formulation of ML to achieve a reliable performance. Our approach negates the subjective use of the matching

pursuit (MP) design parameters. We derive the CRLB for the estimator based on the resolvable channel assumption, and compare its performance to the MP and conventional ML in simulation. Numerical result indicates that the performance of the estimator attains to the CRLB as SNR increases, and it supersedes that of the MP in performance under a resolvable channel, especially in the low SNR region where the LC-ML can transmit multiple pilot symbols to boost the detection probability. Furthermore, the LC-ML can achieve performance equivalent to ML with far fewer measurements than what is required at the Nyquist-rate.

The rest of this chapter is organized as follows: Section 5.2 describes our system model, including the derivation of the LC-ML, Section 5.3 provides the CRLB derivation, Section 5.4 outlines the implementation issues, Section 5.5 presents the simulation results and a summary is given in Section 5.6.

5.2 System Model

We consider a single-user communication system that sends a series of K pilot symbols for channel estimation prior to data transmission. The received signal can be modeled as

$$y(t) = \sum_{k=0}^{K-1} b_k \sum_{j=0}^{N_f-1} \sum_{l=1}^{L} \alpha_l s(t - \tau_l - jT_f - kT_s) + n(t)\,, \tag{5.1}$$

where $\{b_k\}$ are the pilot symbols taking values ± 1, α_l and τ_l are the amplitude and delay of the l-th multipath, respectively, $s(t)$ is the received Gaussian pulse of duration T_p, and T_f is the frame time. There are N_f frames per symbol for a symbol period of $T_s = N_f T_f$ and $n(t)$ is the AWGN with double-sided PSD $N_0/2$. The pilot symbols are transmitted over an observation interval of $T_0 = KT_s$ seconds in which the dense multipath channel is assumed to be static. In (5.1), we model the channel as a L-tap tapped delay line of delay $\tau_l = \tau_1 + \Delta(l-1)$ and a maximum delay spread of T_{mds}

seconds. The parameter Δ denotes the resolvability[1] of the channel with $\Delta \geq T_p$ indicating a resolvable channel and $\Delta < T_p$ an unresolvable channel. We further assume $T_f > T_{mds}$ so there is no inter-frame interference. Without loss of generality and to simplify the notation, we let the polarity of all pilot symbols to be 1 and consider only a single frame, i.e., $N_f = 1$.

Given the signal in (5.1), we model the parameters $\boldsymbol{\alpha} = [\alpha_1, \ldots, \alpha_L]^T$ and $\boldsymbol{\tau} = [\tau_1, \ldots, \tau_L]^T$ as unknown but deterministic quantities. Let $\boldsymbol{\psi} = [\boldsymbol{\alpha}, \boldsymbol{\tau}]^T$ be the continuous-time channel parameter, we apply compressed sensing by expanding (5.1) with M orthonormal basis functions as

$$\begin{aligned} y(t) &= \sum_{k=0}^{K-1} \sum_{m=1}^{M} \breve{y}_{k,m} \phi_m(t - kT_s)\,, \\ \breve{y}_{k,m} &:= \int_{kT_s}^{(k+1)T_s} y(t)\phi_m(t)\,\mathrm{d}t\,, \quad m = 1, \ldots, M \\ &= \breve{s}_{k,m} + \breve{n}_{k,m}\,, \quad m = 1, \ldots, M\,, \end{aligned} \tag{5.2}$$

where $\breve{y}_{k,m}$ is the projection coefficient of the received signal to the m-th basis in the k-th symbol. Similarly, $\breve{s}_{k,m}$ and $\breve{n}_{k,m}$ are the projection coefficients for the signal and noise components, respectively. The basis function $\phi_m(t)$ is a symbol-long sequence with amplitude $\pm\sqrt{F_s'/N}$, pulse width $1/F_s'$ and sequence length $N = T_s F_s'$ drawn from i.i.d. Bernoulli distribution [55], where F_s' denotes the "virtual sampling frequency" [56]. Now, stacking the projection coefficients from the k-th symbol into vectors $\breve{\mathbf{y}}^{(k)} = [\breve{y}_{k,1}, \breve{y}_{k,2}, \ldots, \breve{y}_{k,M}]^T$, $\breve{\mathbf{s}} = [\breve{s}_{k,1}, \breve{s}_{k,2}, \ldots, \breve{s}_{k,M}]^T$ and $\breve{\mathbf{n}}^{(k)} = [\breve{n}_{k,1}, \breve{n}_{k,2}, \ldots, \breve{n}_{k,M}]^T$, in CS notation the received vector during the k-th symbol be-

[1] A resolvable channel is also a non-overlapping channel where the adjacent channel taps are T_p-spaced, i.e., $|\tau_i - \tau_j| \geq T_p$ for $i \neq j$, which is usually true given the tremendous pulse bandwidth [5]. In contrast, an unresolvable channel is an overlapping channel where the adjacent channel taps separation is less than T_p, i.e., $|\tau_i - \tau_j| < T_p$ for $i \neq j$.

comes

$$\breve{\mathbf{y}}^{(k)} = \breve{\mathbf{s}} + \breve{\mathbf{n}}^{(k)} = \mathbf{\Phi}\mathbf{y}^{(k)} = \mathbf{\Phi}(\mathbf{s}(\mathbf{\Psi}) + \mathbf{n}^{(k)}) \,, \tag{5.3}$$

where $\mathbf{y}^{(k)} \in \mathbb{R}^N$ is the vector of the received signal sampled at F_s', $\mathbf{\Phi} \in \mathbb{R}^{M \times N}$ is the measurement matrix with each row comprising of virtually sampled $\phi_m(t)$, $\mathbf{s} \in \mathbb{R}^N$ denotes samples of the desired signal, $\mathbf{n}^{(k)} \in \mathbb{R}^N$ is the vector of AWGN samples and $\mathbf{\Psi}$ represents the discrete time counterpart of $\boldsymbol{\psi}$. The goal here is to estimate the set of parameters by $M \leq N$ measurements. To continue the derivation, we stack $\breve{\mathbf{y}}^{(k)}$ into $\breve{\mathbf{y}} := [\breve{\mathbf{y}}^{(0)T}, \breve{\mathbf{y}}^{(1)T}, \ldots, \breve{\mathbf{y}}^{(K-1)T}]^T$ and write the conditional likelihood function as

$$\begin{aligned} \Lambda(\mathbf{\Psi}) = & \frac{1}{|\sigma_n^2 \mathbf{\Phi}\mathbf{\Phi}^T|^{K/2}(2\pi)^{KN/2}} \times \\ & \exp\left(-\sum_{k=0}^{K-1} (\breve{\mathbf{y}}^{(k)} - \mathbf{\Phi}\mathbf{s}(\mathbf{\Psi}))^T (2\sigma_n^2 \mathbf{\Phi}\mathbf{\Phi}^T)^{-1} (\breve{\mathbf{y}}^{(k)} - \mathbf{\Phi}\mathbf{s}(\mathbf{\Psi})) \right) , \end{aligned} \tag{5.4}$$

where $|\cdot|$ denotes the determinant, $(\cdot)^T$ is the matrix transpose, $(\cdot)^{-1}$ being the matrix inverse, and σ_n^2 is the noise sample variance. Because $\mathbf{\Phi}$ in (5.3) is an orthogonal projector, i.e., $\mathbf{\Phi}\mathbf{\Phi}^T = \mathbf{I}_M$ [55], (5.4) reduces to

$$\Lambda(\mathbf{\Psi}) = \frac{1}{\sigma_n^K (2\pi)^{KN/2}} \exp\left(-\frac{1}{2\sigma_n^2} \sum_{k=0}^{K-1} ||\breve{\mathbf{y}}^{(k)} - \mathbf{\Phi}\mathbf{s}(\mathbf{\Psi})||^2 \right) . \tag{5.5}$$

Ignoring the constant terms, the log-likelihood function can be written as

$$\ln(\Lambda(\mathbf{\Psi})) = \sum_{k=0}^{K-1} \left(2\mathbf{s}^T(\mathbf{\Psi}) \mathbf{\Phi}^T \breve{\mathbf{y}}^{(k)} - ||\mathbf{\Phi}\mathbf{s}(\mathbf{\Psi})||^2 \right) . \tag{5.6}$$

With $\tilde{\mathbf{x}}$ denoting a trial version of $\mathbf{x}$, the ML estimate to $\mathbf{\Psi}$ boils down to

$$\hat{\mathbf{\Psi}} = \arg\max_{\tilde{\mathbf{\Psi}}} \{\ln(\Lambda(\tilde{\mathbf{\Psi}}))\} = \arg\max_{\tilde{\mathbf{\Psi}}} \left\{ 2 \sum_{k=0}^{K-1} \tilde{\mathbf{\Phi}}^T \breve{\mathbf{y}}^{(k)} - \sum_{k=0}^{K-1} ||\mathbf{\Phi}\mathbf{s}(\tilde{\mathbf{\Psi}})||^2 \right\} , \tag{5.7}$$

where $\tilde{\mathbf{\Phi}} = [\mathbf{s}^T(\tilde{\mathbf{\Psi}})\mathbf{\Phi}_1^T, \mathbf{s}^T(\tilde{\mathbf{\Psi}})\mathbf{\Phi}_2^T, \ldots, \mathbf{s}^T(\tilde{\mathbf{\Psi}})\mathbf{\Phi}_M^T]^T \in \mathbb{R}^M$ is a vector of coefficients comprising of the inner product between a trial value of $\mathbf{\Psi}$ and the m-th row of $\mathbf{\Phi}$ denoted as $\mathbf{\Phi}_m$. In the limit as $N \to \infty$ [49], the argument of (5.7) becomes the log-likelihood function as

$$\ln(\Lambda(\tilde{\boldsymbol{\psi}})) = 2\sum_{k=0}^{K-1}\sum_{m=1}^{M} \breve{y}'_{k,m} \int_{kT_s}^{kT_s+T_{prj}} \phi_m(t)\hat{s}(t;\tilde{\boldsymbol{\psi}})\,\mathrm{d}t - \sum_{k=0}^{K-1}\sum_{m=1}^{M}\left(\int_{kT_s}^{kT_s+T_{prj}} \hat{s}(t;\tilde{\boldsymbol{\psi}})\phi_m(t)\,\mathrm{d}t\right)^2, \tag{5.8}$$

where the single-symbol trial value of the template is

$$\hat{s}(t;\tilde{\boldsymbol{\psi}}) = \sum_{l=1}^{L_c} \tilde{\alpha}_l s(t - \tilde{\tau}_l - kT_s)\,, \tag{5.9}$$

where L_c is the ML parameter denoting the number of strongest taps to be estimated. By the use of (5.9), we inherently assume the received signal $y(t)$ to be sparse[2] in certain basis within a single symbol, i.e., L_c sparse on basis $s(t)$ with arbitrary amplitude and delay in $\tilde{\alpha}_l$ and $\tilde{\tau}_l$, respectively, for $l = 1, 2, \ldots, L_c$. In (5.8), $\breve{y}'_{k,m}$ is defined as

$$\breve{y}'_{k,m} = \int_{kT_s}^{kT_s+T_{prj}} y(t)\phi_m(t)\,\mathrm{d}t\,, \quad m = 1, \ldots, M\,, \tag{5.10}$$

where the parameter T_{prj} indicates the integration length. Since our system has no inter-frame interference, i.e., $T_{mds} < T_f$, the majority of the received energy is confined within T_{mds}; therefore, we let $T_p < T_{prj} \leq T_{mds}$. The collection of compressive measurements can be implemented by M integrators, each with an integration interval T_{prj}. In that case, the sequence length becomes $N = T_{prj}F'_s$. Thus, the LC-ML channel estimator reduces to finding the pairs $(\tilde{\boldsymbol{\alpha}}, \tilde{\boldsymbol{\tau}})$ which maximizes (5.8). Specifi-

[2]Although the assumption of sparsity is typically dealt with in the digital domain, one can easily see the resemblance here with the Karhunen-Loéve expansion [49].

cally, it comprises of projecting the received signal onto orthornormal basis $\phi_m(t)$ for $m = 1, \ldots, M$. Hence, instead of sampling at Nyquist rate as in the conventional ML approach, we reduce the sampling rate by collecting fewer compressive measurements. We define the ratio $\rho = M/N$ as the compression ratio of the LC-ML.

To continue with the ML derivation, we recognize the compaction of distance[3], and assume that the spread of multipath energy is confined within the interval $T_{prj} = [0, T_{mds})$, we rewrite (5.8) as

$$\ln(\check{\Lambda}(\tilde{\boldsymbol{\psi}})) \cong 2 \sum_{k=0}^{K-1} \sum_{m=1}^{M} \breve{y}'_{k,m} \int_{T_{prj}} \phi_m(t) \hat{s}(t; \tilde{\boldsymbol{\psi}}) \, \mathrm{d}t - \rho \sum_{k=0}^{K-1} \int_{T_{prj}} \hat{s}^2(t; \tilde{\boldsymbol{\psi}}) \, \mathrm{d}t \,. \quad (5.11)$$

Now, substituting (5.9) into (5.11), we obtain

$$\ln(\check{\Lambda}(\tilde{\boldsymbol{\psi}})) = 2 \sum_{k=0}^{K-1} \sum_{l=1}^{L_c} \tilde{\alpha}_l z_k(\tilde{\tau}_l) - \rho \sum_{k=0}^{K-1} \sum_{l=1}^{L_c} \sum_{l'=1}^{L_c} \tilde{\alpha}_l \tilde{\alpha}_{l'} \int_{T_{prj}} s(t - \tilde{\tau}_l - kT_s) s(t - \tilde{\tau}_{l'} - kT_s) \, \mathrm{d}t \,, \quad (5.12)$$

where $\ln(\check{\Lambda}(\tilde{\boldsymbol{\psi}}))$ approximates $\ln(\Lambda(\tilde{\boldsymbol{\psi}}))$ after compensating for the compaction of distance, and $z_k(\tilde{\tau}_l)$ is defined as

$$z_k(\tilde{\tau}_l) = \sum_{m=1}^{M} \breve{y}'_{k,m} \int_{T_{prj}} \phi_m(t) s(t - \tilde{\tau}_l - kT_s) \, \mathrm{d}t \,. \quad (5.13)$$

Assuming there is no correlation between signal echoes within a symbol duration, i.e., $\int_{T_{prj}} s(t - \tilde{\tau}_l - kT_s) s(t - \tilde{\tau}_{l'} - kT_s) \, \mathrm{d}t = 0$ for $l' \neq l$, (5.12) reduces to

$$\ln(\check{\Lambda}(\tilde{\boldsymbol{\psi}})) = 2 \sum_{k=0}^{K-1} \sum_{l=1}^{L_c} \tilde{\alpha}_l z_k(\tilde{\tau}_l) - K \rho E_s \sum_{l=1}^{L_c} \tilde{\alpha}_l^2 \,, \quad (5.14)$$

[3]In CS theory, for any $\mathbf{x} \in \mathbb{R}^N$, the random variable $||\boldsymbol{\Phi}\mathbf{x}||^2$ has an expected value $\rho||\mathbf{x}||^2$ [55], where $\rho = M/N$. Likewise, in our case $||\boldsymbol{\Phi}\mathbf{s}(\boldsymbol{\Psi})||^2$ has an expected distance of $\rho||\mathbf{s}(\boldsymbol{\Psi})||^2$, then we can express (5.6) as $\ln(\check{\Lambda}(\boldsymbol{\Psi})) = 2\sum_{k=0}^{K-1} \mathbf{s}^T(\boldsymbol{\Psi}) \boldsymbol{\Phi}^T \breve{\mathbf{y}}^{(k)} - \rho \sum_{k=0}^{K-1} ||\mathbf{s}(\boldsymbol{\Psi})||^2$, where $\ln(\check{\Lambda}(\boldsymbol{\Psi}))$ approximates $\ln(\Lambda(\boldsymbol{\Psi}))$ after compression of distance, and take $N \to \infty$ gives (5.11).

where $E_s = \int_{T_{prj}} s^2(t)\,\mathrm{d}t$ is the symbol energy.

We can now estimate the parameter $\boldsymbol{\psi}$ by looking for the pair $(\boldsymbol{\alpha}, \boldsymbol{\tau})$ which minimizes (5.14). The minimization is carried out first by keeping $\boldsymbol{\tau}$ fixed and varying $\boldsymbol{\alpha}$. Specifically, differentiating (5.14) with respect to $\tilde{\alpha}_l$ and equating it to zero, we get

$$\tilde{\alpha}_l = \frac{1}{K\rho E_s} \sum_{k=0}^{K-1} z_k(\tilde{\tau}_l)\,. \tag{5.15}$$

Substituting (5.15) into (5.14), the optimization problem simplifies to

$$\hat{\tau}_l = \arg\max_{\tilde{\tau}_l} \left(\sum_{k=0}^{K-1} z_k(\tilde{\tau}_l) \right)^2, \quad l = 1, \ldots, L_c\,, \tag{5.16}$$

and, the gains are estimated as

$$\hat{\alpha}_l = \frac{1}{K\rho E_s} \sum_{k=0}^{K-1} z_k(\hat{\tau}_l)\,, \quad l = 1, \ldots, L_c\,. \tag{5.17}$$

Comparing to the conventional ML formulation of the path delays and gains [23], the LC-ML channel estimator takes on the extra step of projecting the received signal onto the M independent Bernoulli sequences for compression. Thereafter, the correlation between the compressed signal and the compressed pulse template at each possible path delay, c.f., Fig. 5.1 which shows the implementation of LC-ML with the Rake receiver when multiple pulses are transmitted per symbol, i.e., $T_s = N_f T_f$. Although the compression of a signal results in a reduction of the expected distance by $\sqrt{\rho}$ [55], it can be compensated by scaling the gain estimates accordingly, as shown in the derivation. Altogether, the effort in signal processing guarantees a reduced sampling rate, a necessity especially to alleviate the burden of acquiring fine-scaled samples in the ML scheme. Comparing to MP, which relies heavily on the selection of design parameters that are subject to change depending on the environment, our ap-

proach uses only the traditional ML parameters. Moreover, unlike the MP technique that requires a complete $N \times N$ basis set as the dictionary for ℓ_1-norm minimization [57], the resolution of the LC-ML depends entirely on how $\tilde{\tau}_l$ is chosen in the maximization of (5.16). Finally, we stress that whereas the MP algorithm strictly relies on the processing of the received multipaths from a symbol of single frame pilot for channel estimation [57], the LC-ML capitalizes on the ML formulation of processing multiple symbols to achieve a reliable performance.

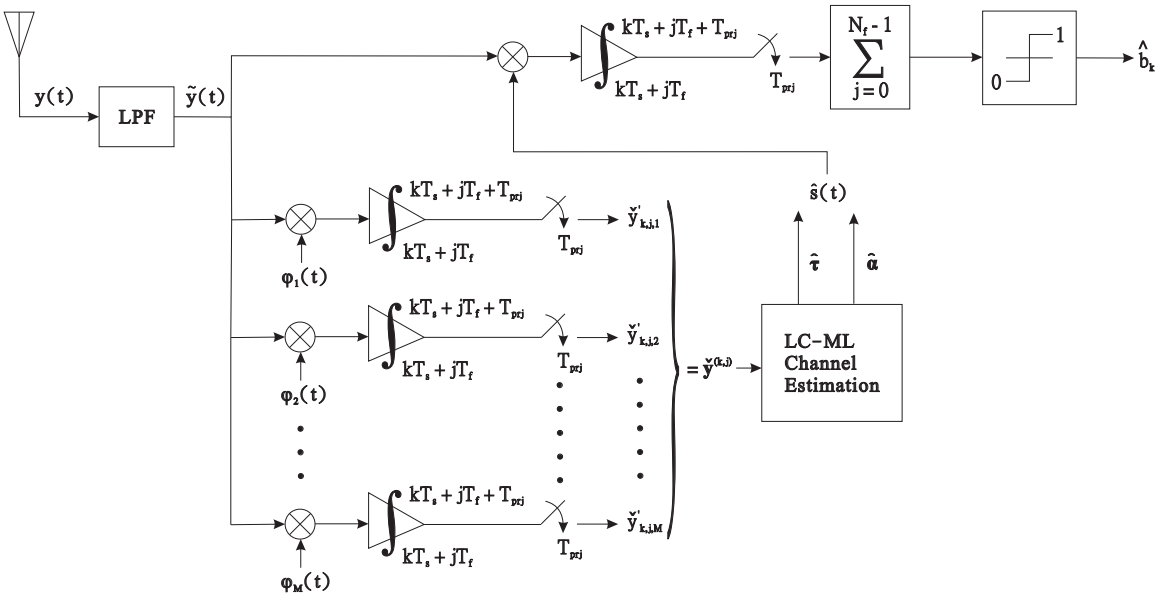

Figure 5.1: The LC-ML channel estimator and its implementation with the Rake receiver.

5.3 Cramér-Rao Lower Bound

Apart from the simulation assessment of the channel estimator proposed in the previous section, we are also interested in its analytical performance bound. For that, we derive the Cramér-Rao Lower Bound in this section. The CRLB provides the lowest possible performance bound an unbiased estimator can attain to [49, 50]. Specifically,

for a vector of unknown but deterministic parameters, e.g., $\boldsymbol{\theta} = [\theta_1, \theta_2, \ldots, \theta_N]^T$, the lowest possible bound on the variance of the unbiased estimates $\hat{\boldsymbol{\theta}}$ to $\boldsymbol{\theta}$ is given by

$$\sigma^2_{\boldsymbol{\theta}} = \mathbb{E}\{(\hat{\boldsymbol{\theta}} - \boldsymbol{\theta})(\hat{\boldsymbol{\theta}} - \boldsymbol{\theta})^T\} \geq \mathbf{J}^{-1}(\boldsymbol{\theta})\,, \tag{5.18}$$

where $\mathbb{E}\{\cdot\}$ is the expectation operation, and $\mathbf{J}(\boldsymbol{\theta}) \in \mathbb{R}^{N\times N}$ is the Fisher Information Matrix (FIM). The derivation of the CRLB for LC-ML parallels that of [72] except with the inclusion of the compressive measurements. Then, as derived in Appendix B, the CRLB on the amplitude and delay estimates based on the non-overlapping multipath assumption is given by

$$\mathrm{var}(\hat{\alpha}_l) := \mathbb{E}\{(\hat{\alpha}_l - \alpha_l)^2\} \geq \frac{\sigma^2}{KN_f\rho E_1}\left(\frac{E_3}{E_3 - E_2^2/E_1}\right)\,, \tag{5.19}$$

$$\mathrm{var}(\hat{\tau}_l) := \mathbb{E}\{(\hat{\tau}_l - \tau_l)^2\} \geq \frac{\sigma^2}{KN_f\alpha_l^2\rho E_1}\left(\frac{E_1}{E_3 - E_2^2/E_1}\right)\,, \tag{5.20}$$

for $l = 1, 2, \ldots, L$, σ^2 is the double-sided noise power spectral density, and the energy terms are

$$\begin{aligned} E_1 &= \int_{T_p} s^2(t)\,\mathrm{d}t\,, \\ E_2 &= \int_{T_p} \dot{s}(t)s(t)\,\mathrm{d}t\,, \\ E_3 &= \int_{T_p} \dot{s}^2(t)\,\mathrm{d}t\,, \end{aligned} \tag{5.21}$$

where $s(t)$ is the received pulse shape modeled as a Gaussian pulse as described in Section 5.2, and $\dot{s}(t)$ denotes the derivative of $s(t)$ with respect to t. For the non-overlapping performance bound, (5.19) and (5.20) differ from those in [72] by the multiplication of a compression ratio ρ, which raises the lower bound depending on the rate of compression. Intuitively, this makes sense since more compression, i.e., a

small ρ, would result in a higher bound due to a loss of information and vice versa.

5.4 Implementation Issues

To discuss the implementation issues of the LC-ML, we resort to the digital domain representation. Specifically, after passing $y(t)$ through a low-pass filter of bandwidth B and assuming no signal distortion, traditionally $N' = T_s/T_{sa}$ integer samples per symbol are collected at the Nyquist rate $1/T_{sa} = 2B$ from the filtered output $r(t)$. We digitize the delay trial value as $\lfloor \tilde{\tau}_l/T_{sa} \rfloor := (l_p Z + l_f)$, where $Z := \lfloor T_p/T_{sa} \rfloor$ denotes the integer number of samples per pulse, $\lfloor \cdot \rfloor$ being the flooring function, and l_p and l_f are the pulse delay and fine sample delay indexes, respectively. Then, $r[i] := r(iT_{sa})$ and $s[i - kN' - (l_p Z + l_f)] := s((i - kN' - (l_p Z + l_f))T_{sa})$, and with these notations, the delay estimates of the ML estimator operating digitally with l_p-space estimator (i.e., $l_f = 0$), on the l_p-th path can be written as

$$\hat{l}_p = \arg\max_{\tilde{l}_p} \left(\sum_{k=0}^{K-1} v_k[\tilde{l}_p] \right)^2 , \tag{5.22}$$

$$v_k[l_p] = \sum_{i=1}^{KN'} r[i] s[i - kN' - l_p Z] , \tag{5.23}$$

where we have approximated the integral by a summation. Similarly, the digital equivalent representation of LC-ML is

$$\hat{l}_p = \arg\max_{\tilde{l}_p} \left(\sum_{k=0}^{K-1} z_k[\tilde{l}_p] \right)^2 , \tag{5.24}$$

$$z_k[l_p] = \sum_{m=k}^{(k+1)M} \breve{r}'[m] \breve{s}'[m, l_p] , \tag{5.25}$$

where $\breve{s}'[m, l_p] := \sum_{i=k}^{(k+1)N'} \phi_m[i]s[i - kN' - l_pZ]$ is the coefficient of the discretized template after being projected onto the m-th basis for $m = 1, \ldots, M$. Therefore, comparing both (5.23) and (5.25), we see that compressive measurements essentially reduce the Nyquist rate by a factor of N'/M. This reduction amounts to extra savings in hardware and is indispensable if we are to implement the ML estimator. Detailed implementation of the LC-ML channel estimator with the Rake receiver is shown in Fig. 5.1.

5.5 Simulation Results

We examine the effectiveness of our LC-ML channel estimator by computer simulation in the MATLAB$^{\text{TM}}$ environment. Under the non-overlapping assumption, we first illustrate the asymptotic behavior of the ML estimator in an academic setting with a sparse channel. The asymptotic behavior of ML is characterized by its performance attaining to the CRLB as SNR increases [49, 50]. We then evaluate its performance in terms of the reconstruction MSE in a resolvable channel, and compare with both the ML and MP ℓ_1-norm minimization estimators. Finally, we compare the bit-error rate (BER) performance between the LC-ML and the ML estimators under a realistic dense multipath channel in which pulse overlapping can occur due to unresolvable channel taps.

5.5.1 Cramér-Rao Lower Bound

We conduct the simulation in an academic setting [23, 72] to evaluate the derived CRLB. The simulation environment contains a fixed 3-tap channel of amplitudes $\alpha_1 = 0.73$, $\alpha_2 = 0.67$ and $\alpha_3 = 0.35$, with spacings $\tau_l = 5lT_p$ for $l = 1, 2, 3$. The other simulation parameters are $T_f = 40$ ns, $K = 100$, $N_f = 20$, $s(t)$ is modeled as a

Gaussian doublet as

$$s(t) = \left[1 - 16\pi\left(\frac{t}{T_p} - 0.5\right)^2\right] \exp\left[-8\pi\left(\frac{t}{T_p} - 0.5\right)^2\right], \tag{5.26}$$

with $T_p = 2$ ns, and we consider only a single user. The simulation is performed over a thousand independent trials, and ρ is allowed to vary, signifying different compression ratio. The SNR here is defined as the ratio of the symbol energy to the noise variance as $E_b/2\sigma^2$, and for a double-sided noise PSD of $N_0/2$, the ratio becomes E_b/N_0, which is adjusted with respect to the symbol energy in the simulation. Fig. 5.2 illustrates the standard deviation of $\hat{\tau}_1$ and the corresponding CRLB as a function of SNR. The compression ratio ρ is implicitly embedded as a function of the design parameter M (viewed here as a percentage of N). As shown, the standard deviation of the estimates comes in close agreement with the CRLB for each M, especially as the SNR increases. Similar observation to the standard deviation of $\hat{\alpha}_1$ also occurs in Fig. 5.3. One thing to note is the deviation from CRLB for M of 15%, which can be explained by the drastic reduction of signal information due to the use of fewest number of projection coefficients in (5.10), thus exacerbates the error in estimation. However, as can be extrapolated from both figures, the error variance for $M = 15\%$ can eventually attain to the bound once the SNR is high enough.

5.5.2 MSE Performance

Although evaluating the CRLB in the last section showcases the unbiasedness of the LC-ML as both M and SNR increases, it provides no comparison in performance to other estimators. In this section, we compare all three channel estimators, i.e., the ML, MP, and LC-ML, under the assumption of a resolvable channel. In the case when pulse overlapping is allowed, we show in the next section that the LC-ML can still

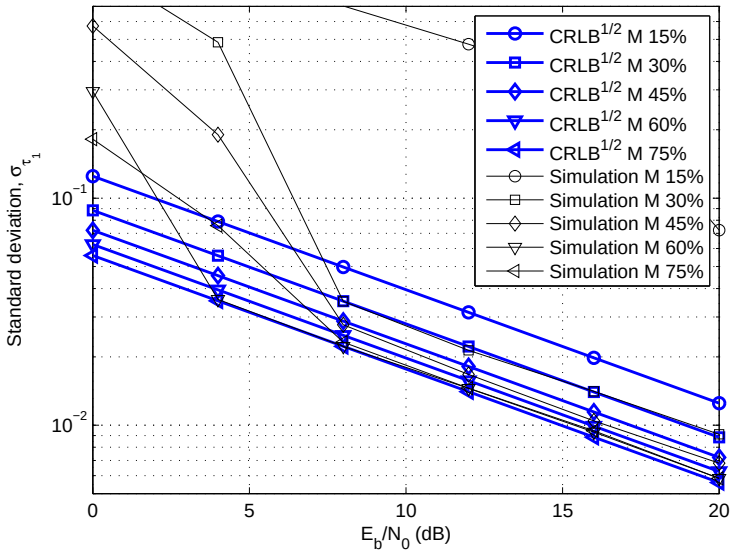

Figure 5.2: Standard deviation of $\hat{\tau}_1$ as a function of SNR with varying M (viewed here as a percentage of N) for a fixed, 3-tap channel.

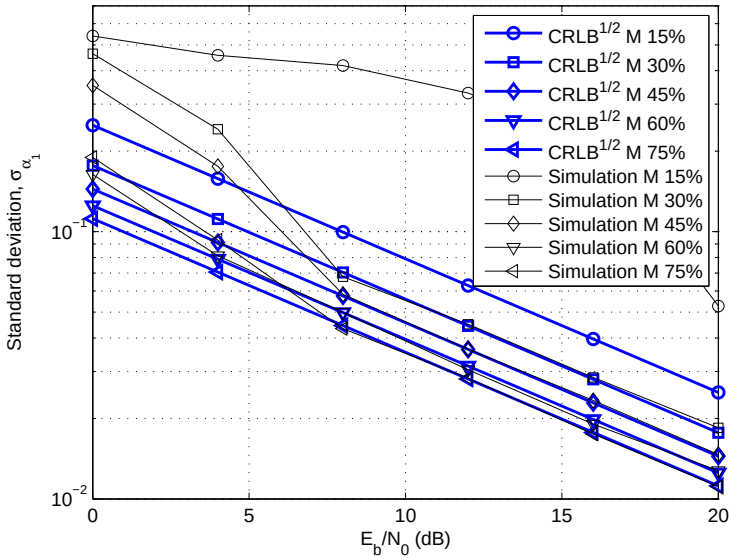

Figure 5.3: Standard deviation of $\hat{\alpha}_1$ as a function of SNR with varying M for a fixed, 3-tap channel.

achieve performance close to the ML with a reduction in complexity as described in Section 5.4.

Fig. 5.4 illustrates the MSE behavior as SNR varies for $K = 20$, and $L_c = 20$. As shown, MP results in the worst performance since its estimates are based on the multipath returns of an isolated pulse. In contrast, the gain of employing data-aided (DA) estimation is quite obvious with the conventional ML giving the best performance while the LC-ML falling in between ML and MP. Depending on the design parameter M, the performance of LC-ML varies due to a varying compression rate, with a small M indicating high compaction and lower complexity, but more error prone.

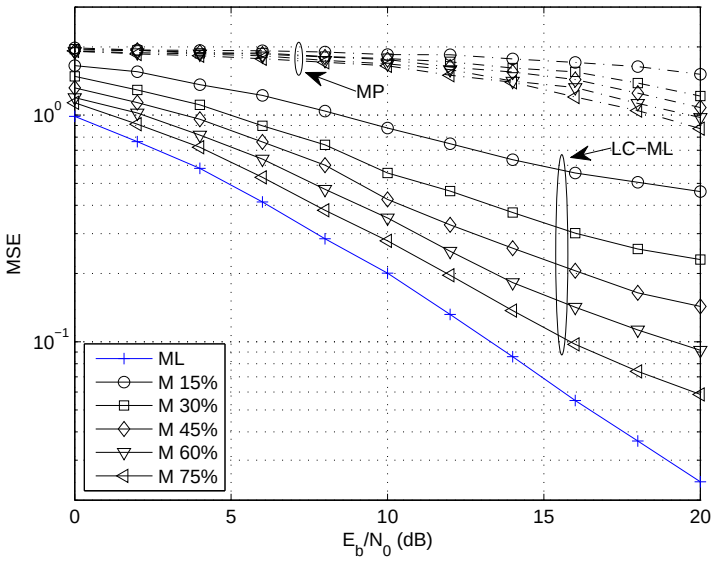

Figure 5.4: MSE as SNR varies for $K = 20$, $T_{prj} = T_f$ and $L_c = 20$. The design parameter M (viewed here as a percentage of N) is allowed to vary for the LC-ML. The solid and dash-dot lines represent LC-ML and MP channel estimators, respectively.

One of the advantages of the ML type estimators is to rely on an increasing number of pilot symbols to enhance the overall estimator performance. To demonstrate this, Fig. 5.5 plots MSE versus SNR for $K = 100$. Comparing to when $K = 20$, we

see an improvement for both ML and LC-ML estimators, especially at low SNR. Unfortunately, MP cannot take the advantage of elongating the observation window as it is based on the processing of an isolated pulse. The reduction in complexity

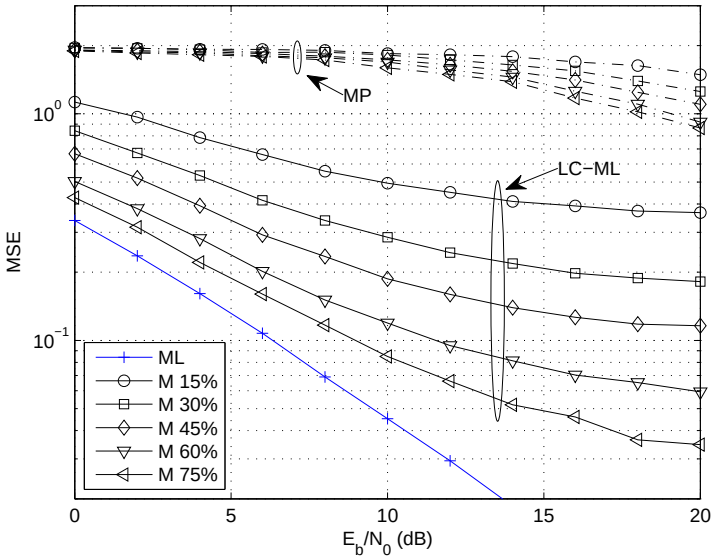

Figure 5.5: MSE as SNR varies for $K = 100$, $T_{prj} = T_f$ and $L_c = 20$. The LC-ML and MP channel estimators are denoted by solid and dash-dot lines, respectively.

can go even further for the LC-ML by reducing T_{prj} in (5.10). Whereas this has not been done for the conventional ML scheme, the gains with a varying T_{prj} in LC-ML are two-fold: first, by decreasing the integration region we are reducing the amount of noise in the system and, with a T_{prj} properly chosen, the performance may substantially improve. Secondly, reducing T_{prj} implicitly reduces the number of integrators necessary for compression, resulting in an overall reduction on the system complexity. We illustrate the effect of reducing T_{prj} in Fig. 5.6 which plots the MSE as SNR varies for $T_{prj} = 40$ ns. As expected, decreasing T_{prj} improves the performance at low SNR but hinders the accuracy at high SNR where a higher floor is clearly visible. Fortunately, this flooring behavior does not diminish the BER performance,

as is shown next.

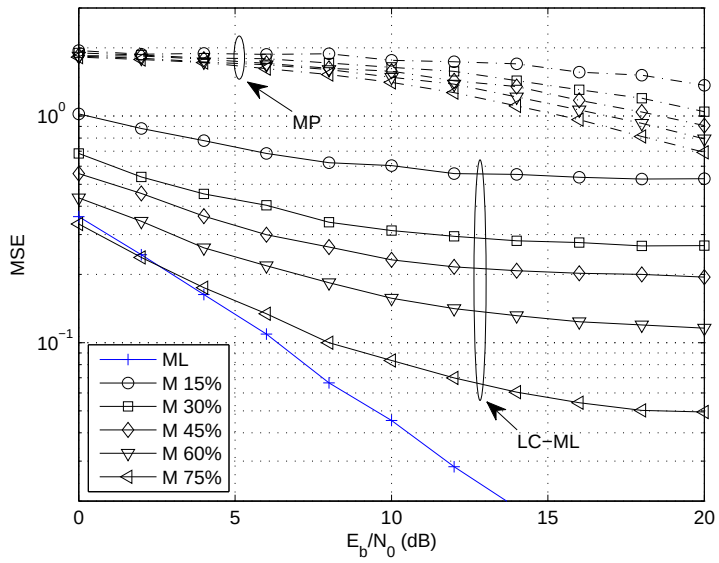

Figure 5.6: MSE as SNR varies for $K = 100$, $T_{prj} = 40$ ns and $L_c = 20$. The LC-ML and MP channel estimators are denoted by solid and dash-dot lines, respectively.

5.5.3 BER Performance

To evaluate the BER performance, we consider the reception of A-PAM with a Rake receiver in a single-user scenario with overlapping channel model. The system first sends K pilot symbols for DA channel estimation prior to the burst of data transmission. Based on the sequences of estimated multipath gains and delays, i.e., $\{\hat{\alpha}_l\}_{l=1}^{L_c}$ and $\{\hat{\tau}_l\}_{l=1}^{L_c}$, respectively, from either the LC-ML or ML estimators the Rake receiver then performs the maximum-ratio combining [23] with $T_{prj} \in [0, T_f)$ as the integration interval on the j-th frame to produce the decision statistic. Fig. 5.7 illustrates the BER performance of the two schemes with $K = 20$, $L_c = 20$ and $T_{prj} = 40$ ns. For the LC-ML, M is allowed to take on different values, representing different compression rate. The data burst is set to $1,000$ bits and a thousand channels are

averaged. As shown, the estimation capability of the LC-ML can be as good as the ML but at a reduced sampling rate, e.g., with $45\% \leq M \leq 75\%$ the performance is almost as good as and sometimes very close to the ML. Apart from varying M, the distinct advantage of ML is to rely on elongating the observation window to boost the performance in a noisy environment. To show that, Fig. 5.8 graphs the BER performance for $K = 100$. Comparing to when $K = 20$, we see an improvement at all values of M for LC-ML, and the performance of both estimators approaching that of the ideal Rake. In summary, although the LC-ML demonstrates a superior performance as M and K increase, one would still need to consider the complexity tradeoff and with a larger M incurring a higher complexity, i.e., a larger number of intergrators.

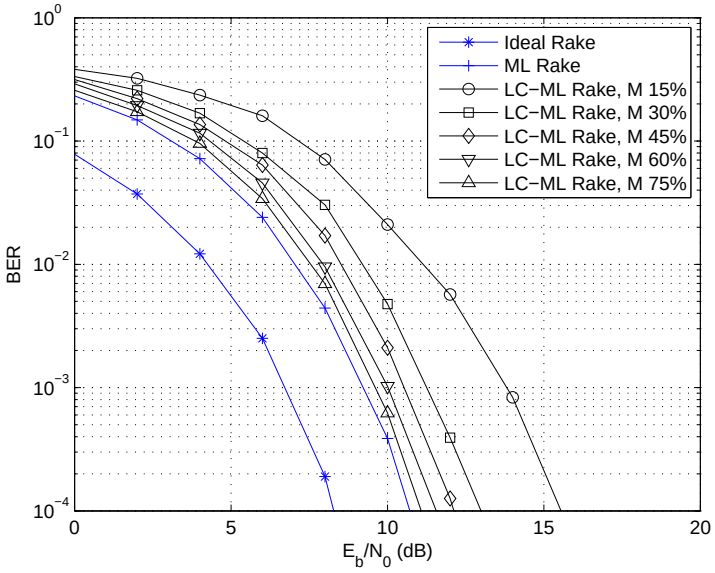

Figure 5.7: BER of A-PAM Rake receiver for $K = 20$ and $L_c = 20$. For the LC-ML, we let $T_{prj} = 40$ ns and M (viewed here as a percentage of N) is varied representing different compression rate.

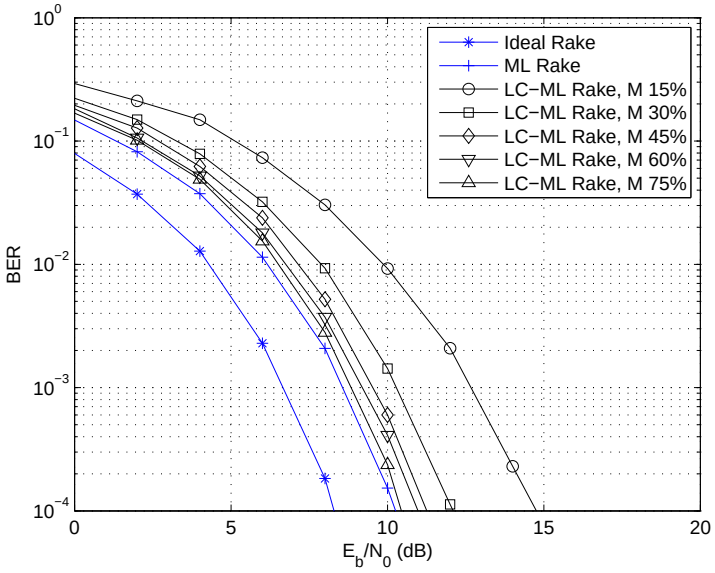

Figure 5.8: BER of A-PAM Rake receiver for $K = 100$, $L_c = 20$ and $T_{prj} = 40$ ns. The compression rate M is allowed to vary for the LC-ML estimator.

5.6 Summary

The rich multipath characteristic of an impulsive UWB channel motivates the use of Rake receivers. Although data-aided ML channel estimator shows a promising performance, the Nyquist criterion renders its implementation difficult. In this chapter, we have proposed the LC-ML channel estimator which combines the compression framework of compressed sensing for sampling rate reduction while retaining the noise statistics formulation of ML to achieve a reliable performance. Besides deriving the CRLB for the estimator based on the non-overlapping assumption, we demonstrate in simulation that, with far fewer measurements and under an overlapping channel, the performance of our scheme supersedes that of the MP-based estimator and can be as good as the conventional ML estimator with a reduction in complexity.

Chapter 6

Conclusion and Future Work

6.1 Conclusion and Summary of Contributions

The many features of the UWB are highly favorable in applications where the deployment of traditional narrowband system is simply insufficient. However, as application evolves toward a more realistic situation, wideband channel characteristics such as pulse distortion must be accounted for in the channel modeling, particularly with time-domain deconvolution techniques. Application-oriented services such as using UWB-IR in ranging and localization demand fast prototyping, real-time processing of measured data, and good low SNR performance, all of which are still currently under investigation. Despite the tremendous effort being invested in devising new receivers by the global research community, channel-estimating Rake receiver is still one of the most promising receivers that can offer better performance than the sub-optimal counterparts. However, acquiring Nyquist-rate samples must be bypassed to ensure the feasible implementation of the ML channel estimator. In this thesis, we have addressed all these aspects of the UWB-IR, namely, channel characterization, ToA estimation and channel estimation, in three separate contributions.

In Chapter 3, we have studied the *a priori* dependency of the single-template CLEAN deconvolution algorithm with real-world measurements. This is quite important since CLEAN is one of the most widely used algorithm in the processing of time-domain channel measurements. Additionally, we have proposed a high-resolution, multi-template deconvolution algorithm to enhance the channel estimation accuracy. This algorithm attempts to address the *a priori* dependency by incorporating realistic frequency-dependent pulse distortions. Our algorithm is shown to supersede its predecessors in terms of accuracy, energy capture and computational speed.

To improve the ranging accuracy when localizing with UWB-IR, we have proposed a *regularized* least squares estimator with wavelet denoising in Chapter 4. Our algorithm estimates the ToA as a by-product of the RLS channel estimation based on a thresholding technique, which is simple, effective at low SNR, and can enable fast online processing. Besides devising a threshold selection strategy based on the Neyman-Pearson criterion, we have shown the robustness of our algorithm by comparing with other algorithms in both computer simulation and UWB ranging measurements when advanced DSP is available.

As addressed in Chapter 5, to fully exploit the multipath diversity with Rake receiver without acquiring the formidable Nyquist-rate samples, we have proposed a low-complexity ML channel estimator which combines the compression framework of compressed sensing for sampling rate reduction while retaining the noise statistics formulation of ML to achieve a reliable performance. Furthermore, we have derived the Cramér-Rao Lower Bound for the LC-ML, and performed simulation to compare our estimator with both the ℓ_1-norm minimization technique and the conventional ML estimator.

We would like to stress that the contributions are novel in ways such that we have either improved upon and/or extended the work of recent literatures.

6.2 Limitations and Future Work

There are several limitations on the assumptions used in this thesis which can be investigated as possible future work.

1. Despite our best effort in devising new algorithms to address problems in channel characterization, ToA and channel estimation, these algorithms inherently are all model-based algorithms which rely on the correlation between the signal and a certain template, e.g., the *a priori* template in CLEAN, and the ML correlator. As discussed in Section 2.1.2, degradation in the estimator performance would occur even if there exists a small template mismatch. Thus, we must look into the possibility of mitigating these model-based assumptions in future research. One possibility is to use the template estimation algorithm, e.g., [73, 74].

2. Although we have reduced the Nyquist-rate sampling requirement of the conventional ML channel estimator with compressive measurements, the LC-ML described in Chapter 5 still requires the search over the $2L_c$-parameter space, which can be overwhelming given the rich multipath characteristic of the UWB channel. However, as shown in Section 5.5.3, even with overlapping MPC's the performance of MRC Rake receiver can still be quite substantial with a small L_c. Nevertheless, we must look into reducing the parameter space so that real-time channel estimation can be fulfilled.

3. The channel and range measurements used in Chapters 3 and 4 must be expanded to accommodate the possible deployment of UWB in other applications, e.g., in BAN and/or time-varying tracking operations. Especially as UWB technology becomes more mature, the robustness of any new algorithm must be tested on application-oriented measurements to ensure the full compliance to

the result obtained from computer simulation.

4. Albeit their high-resolution capability, the performance of both the CLEAN-based algorithms and RLS-WD estimator is strictly limited by the processing of an isolated pulse. The transmission of an isolated pulse not only violates the emission spectral mask imposed by the FCC, but also degrades the performance of the algorithm in processing low SNR measurements. Workaround such as averaging over multiple received pulses, e.g., [18, 19], is one way to address this issue.

5. A majority of the simulations are performed based on the IEEE 802.15.3a channel model. For the sake of completeness, performance can also be assessed with the IEEE 802.15.4a channel model.

Appendix A

Description of the UWB Ranging Experiment

This appendix describes the UWB ranging experiment conducted by Lee in [17] and demonstrates the application of WD to the measured data.

The measurements were taken in a laboratory environment where the interior walls are made of metal stud and dry wall with either cinder blocks or wooden constructions. Fig. A.1 shows the building floor plan where measurements of up to 93 feet were taken. Except the clear LOS reference at location 1, the remaining signals were recorded with a multitude of obstructions in between the TX and RX, resembling NLOS operation. The setup consisted of a pulser that periodically transmits a sub-nanosecond pulse to the RX side, which then amplifies the received signal before being sampled by a DSO for offline post-processing. A pair of vertically polarized diamond dipole antennas were used to radiate the signal. We apply WD in Fig. A.2 to the measured signal at location 13. Clearly, even with $\hat{\sigma}^2$ computed[1] according to (4.15), the noise can be

[1]In (4.15), the N samples of M are obtained from the first few nanoseconds of the measurements until the direct-path ToA, which is calculated relative to the true measured range assuming a clear LOS path between TX and RX. In reality, σ^2 can be estimated from the samples when there is no communication between the nodes.

mostly removed from the original signal.

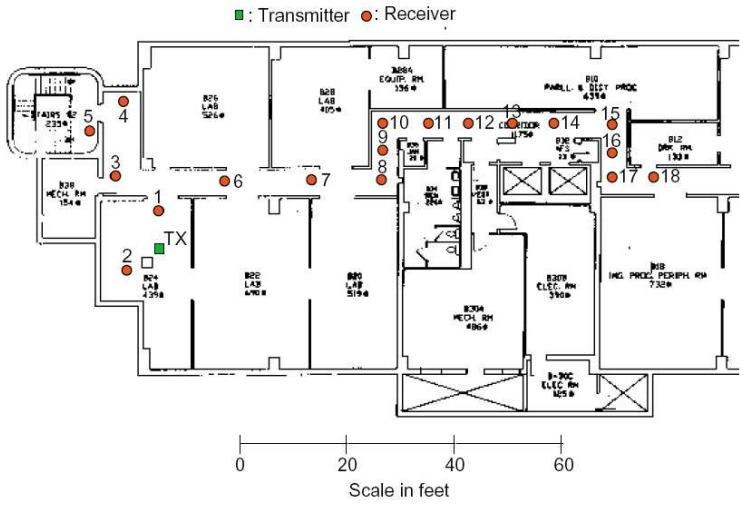

Figure A.1: The building floor plan for the range measurements [17]. The circular and square marks indicate the location of the RX antenna and that of the TX antenna, respectively.

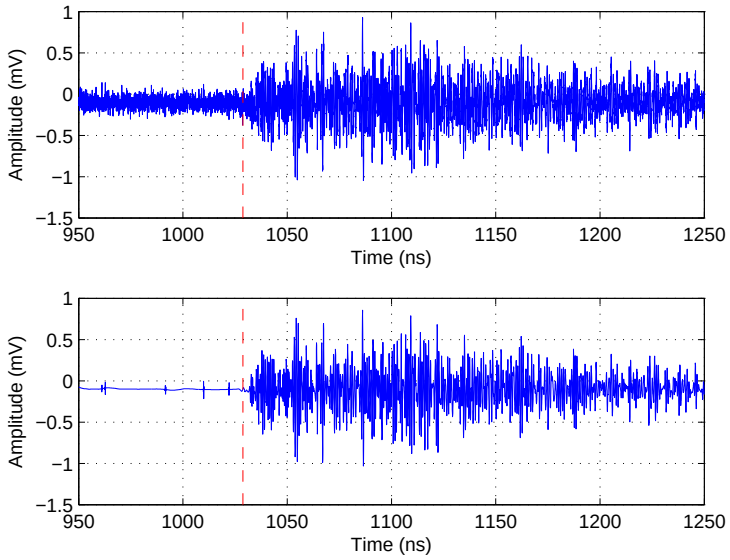

Figure A.2: The measured signal taken at location 13 (top) and its denoised version (bottom). The vertical line of each plot denotes the direct-path ToA, assuming a clear LOS path between TX and RX in the true measured range.

Appendix B

Derivation of the Cramér-Rao Lower Bound in (5.19) and (5.20)

This appendix outlines the derivation of the CRLB in (5.19) and (5.20). The derivation herein parallels that of [72].

From Section 5.2, the received signal in a single-user scenario can be expressed as

$$y(t) = \tilde{g}(t) + n(t)\,,$$

where $\tilde{g}(t) := \sum_{l=1}^{L} \alpha_l g(t-\tau_l)$ and $g(t) := \sum_{k=0}^{K-1}\sum_{j=0}^{N_f-1} s(t-jT_f-kT_s)$ represents the aggregated K symbol-long received signal and aggregated received symbol, respectively. The notations for the rest of the variables are given in Section 5.2 except $n(t)$ is AWGN but with double-sided PSD σ^2. When we transmit multiple frames per pilot, i.e., $N_f \geq 1$, the log-likelihood function from Section 5.1 can be extended as

$$\ln(\check{\Lambda}(\boldsymbol{\psi})) = \frac{1}{2\sigma^2}\left\{ 2\sum_{k=0}^{K-1}\sum_{j=0}^{N_f-1}\sum_{m=1}^{M} \breve{y}'_{k,j,m}\int_{T_f} \phi'_m(t)\tilde{g}(t)\,\mathrm{d}t - \rho\sum_{k=0}^{K-1}\sum_{j=0}^{N_f-1}\left(\int_{T_f}\tilde{g}(t)\,\mathrm{d}t\right)^2\right\}, \tag{B.1}$$

where $\phi'_m(t)$ is now a T_f-long orthonormal basis function which can be chosen from

a i.i.d. Bernoulli distribution, and the parameter $\breve{y}'_{k,j,m}$ is similarly extended as

$$\breve{y}'_{k,j,m} = \int_{T_f} y(t)\phi'_m(t)\,\mathrm{d}t\,, \quad m = 1, \ldots, M\,,$$

and, different from Section 5.1, we have included the $1/2\sigma^2$ factor that is indispensable in the CRLB derivation, but is usually ignored in the ML derivation [23]. For the sake of simplicity, the integration region in the above formulas is over T_f, but it can be restricted to T_{prj} as explained in Section 5.1.

Assuming $\phi'_m(t)$ to be a deterministic quantity, taking derivatives with respect to α_l and τ_l on (B.1) and rearrange gives

$$\frac{\partial \ln(\check{\Lambda}(\boldsymbol{\psi}))}{\partial \tau_l} = \frac{-\alpha_l}{\sigma^2}\left\{ \sum_k \sum_j \left[\sum_m \breve{y}'_{k,j,m} \int_{T_f} \phi'_m(t)\dot{g}(t-\tau_l)\,\mathrm{d}t - \rho \int_{T_f} \tilde{g}(t)\dot{g}(t-\tau_l)\,\mathrm{d}t \right] \right\}, \tag{B.2}$$

$$\frac{\partial \ln(\check{\Lambda}(\boldsymbol{\psi}))}{\partial \alpha_l} = \frac{1}{\sigma^2}\left\{ \sum_k \sum_j \left[\sum_m \breve{y}'_{k,j,m} \int_{T_f} \phi'_m(t)g(t-\tau_l)\,\mathrm{d}t - \rho \int_{T_f} \tilde{g}(t)g(t-\tau_l)\,\mathrm{d}t \right] \right\}, \tag{B.3}$$

for $l = 1, \ldots, L$, where $\dot{g}(t) := \sum_{k=0}^{K-1} \sum_{j=0}^{N_f-1} \dot{s}(t - jT_f - kT_s)$ is the symbol-long received pulse comprising of the first derivative of $s(t)$. Continuing the derivation by differentiating (B.2) with respect to τ_i and (B.3) with respect to α_i and τ_i, we obtain

$$\begin{aligned}
-\mathbb{E}\left\{ \frac{\partial^2 \ln(\check{\Lambda}(\boldsymbol{\psi}))}{\partial \tau_l \partial \tau_i} \right\} &= \frac{\alpha_l \alpha_i \rho}{\sigma^2} \left\{ \sum_k \sum_j \left(\int_{T_f} \dot{g}(t-\tau_l)\dot{g}(t-\tau_i)\,\mathrm{d}t \right) \right\}, \\
-\mathbb{E}\left\{ \frac{\partial^2 \ln(\check{\Lambda}(\boldsymbol{\psi}))}{\partial \alpha_l \partial \tau_i} \right\} &= \frac{-\alpha_i \rho}{\sigma^2} \left\{ \sum_k \sum_j \left(\int_{T_f} \dot{g}(t-\tau_i)g(t-\tau_l)\,\mathrm{d}t \right) \right\}, \\
-\mathbb{E}\left\{ \frac{\partial^2 \ln(\check{\Lambda}(\boldsymbol{\psi}))}{\partial \alpha_l \partial \alpha_i} \right\} &= \frac{\rho}{\sigma^2} \left\{ \sum_k \sum_j \left(\int_{T_f} g(t-\tau_l)g(t-\tau_i)\,\mathrm{d}t \right) \right\},
\end{aligned} \tag{B.4}$$

where $\mathbb{E}\{\cdot\}$ is the expectation operator taking with respect to the parameters of

interest. For the simplicity, we assume that there is no correlation between signal echoes within a single frame [72], then B.4) can be simplified to

$$
\begin{aligned}
-\mathbb{E}\left\{\frac{\partial^2 \ln(\check{\Lambda}(\boldsymbol{\psi}))}{\partial\tau_l\partial\tau_i}\right\} &= \begin{cases} \frac{KN_f\alpha_l^2\rho}{\sigma^2}\left(\int_{T_f}\dot{s}^2(t)\,\mathrm{d}t\right), & i=l\,, \\ 0\,, & i\neq l\,, \end{cases} \\
-\mathbb{E}\left\{\frac{\partial^2 \ln(\check{\Lambda}(\boldsymbol{\psi}))}{\partial\alpha_l\partial\tau_i}\right\} &= \begin{cases} \frac{-KN_f\alpha_i\rho}{\sigma^2}\left(\int_{T_f}\dot{s}(t)s(t)\,\mathrm{d}t\right), & i=l\,, \\ 0\,, & i\neq l\,, \end{cases} \\
-\mathbb{E}\left\{\frac{\partial^2 \ln(\check{\Lambda}(\boldsymbol{\psi}))}{\partial\alpha_l\partial\alpha_i}\right\} &= \begin{cases} \frac{KN_f\rho}{\sigma^2}\left(\int_{T_f}s^2(t)\,\mathrm{d}t\right), & i=l\,, \\ 0\,, & i\neq l\,. \end{cases}
\end{aligned} \tag{B.5}
$$

The individual element of the FIM[1] can be written according to (B.5) as

$$\mathbf{J}_{\boldsymbol{\alpha}\boldsymbol{\alpha}} = \mathrm{diag}\left\{\frac{KN_f\rho}{\sigma^2}E_1,\ldots,\frac{KN_f\rho}{\sigma^2}E_1\right\}, \tag{B.6}$$

$$\mathbf{J}_{\boldsymbol{\alpha}\boldsymbol{\tau}} = \mathbf{J}_{\boldsymbol{\tau}\boldsymbol{\alpha}} = \mathrm{diag}\left\{\frac{-KN_f\alpha_1\rho}{\sigma^2}E_2,\ldots,\frac{-KN_f\alpha_L\rho}{\sigma^2}E_2\right\}, \tag{B.7}$$

$$\mathbf{J}_{\boldsymbol{\tau}\boldsymbol{\tau}} = \mathrm{diag}\left\{\frac{KN_f\alpha_1^2\rho}{\sigma^2}E_3,\ldots,\frac{KN_f\alpha_L^2\rho}{\sigma^2}E_3\right\}, \tag{B.8}$$

where E_i for $i = 1, 2, 3$ are the energy terms defined in (5.21). Consequently, the CRLB's are given by

$$\mathrm{var}(\hat{\alpha}_l) \geq [\mathbf{J}^{-1}(\theta)]_{l,l} = [(\mathbf{J}_{\boldsymbol{\alpha}\boldsymbol{\alpha}} - \mathbf{J}_{\boldsymbol{\alpha}\boldsymbol{\tau}}\mathbf{J}_{\boldsymbol{\tau}\boldsymbol{\tau}}^{-1}\mathbf{J}_{\boldsymbol{\tau}\boldsymbol{\alpha}})^{-1}]_{l,l}\,, \tag{B.9}$$

$$\mathrm{var}(\hat{\tau}_l) \geq [\mathbf{J}^{-1}(\theta)]_{L+l,L+l} = [(\mathbf{J}_{\boldsymbol{\tau}\boldsymbol{\tau}} - \mathbf{J}_{\boldsymbol{\alpha}\boldsymbol{\tau}}\mathbf{J}_{\boldsymbol{\alpha}\boldsymbol{\alpha}}^{-1}\mathbf{J}_{\boldsymbol{\tau}\boldsymbol{\alpha}})^{-1}]_{l,l}\,. \tag{B.10}$$

Substituting (B.6)–(B.8) into (B.9) and (B.10) results in (5.19) and (5.20).

[1]The FIM is defined as $\mathbf{J}(\boldsymbol{\psi}) = \begin{bmatrix} \mathbf{J}_{\boldsymbol{\alpha}\boldsymbol{\alpha}} & \mathbf{J}_{\boldsymbol{\alpha}\boldsymbol{\tau}} \\ \mathbf{J}_{\boldsymbol{\tau}\boldsymbol{\alpha}} & \mathbf{J}_{\boldsymbol{\tau}\boldsymbol{\tau}} \end{bmatrix}$ [49, 50, 72].

Bibliography

[1] "First report and order: In the matter of revision of part 15 of the commission's rules regarding ultra-wideband transmission systems," Tech. Rep. 02-48, FCC, April 2002. 1

[2] L. Yang and G. Giannakis, "Ultra-wideband communications: an idea whose time has come," *IEEE Signal Process. Mag.*, vol. 21, no. 6, pp. 26–54, 2004. 1, 4, 9, 10, 20

[3] J. Reed, *An introduction to ultra wideband communication systems*. Upper Saddle River, NJ: Prentice–Hall, 2005. 1, 3

[4] M. Win and R. Scholtz, "Ultra-wide bandwidth time-hopping spread-spectrum impulse radio for wireless multiple-access communications," *IEEE Trans. Commun.*, vol. 48, no. 4, pp. 679–689, 2000. 4

[5] M. Win and R. Scholtz, "Characterization of ultra-wide bandwidth wireless indoor channels: a communication-theoretic view," *IEEE J. Sel. Areas Commun.*, vol. 20, no. 9, pp. 1613–1627, 2002. 4, 5, 6, 10, 16, 18, 19, 20, 30, 57, 71

[6] A. Molisch, "Ultra-wide-band propagation channels," *Proc. IEEE*, vol. 97, no. 2, pp. 353–371, 2009. 1, 3, 5, 9, 10, 11, 15, 18, 26

[7] S. Gezici, Z. Tian, G. Giannakis, H. Kobayashi, A. Molisch, H. Poor, and

Z. Sahinoglu, "Localization via ultra-wideband radios: a look at positioning aspects for future sensor networks," *IEEE Signal Process. Mag.*, vol. 22, no. 4, pp. 70–84, 2005. 2, 3, 6, 17, 18, 19, 20, 60

[8] A. Molisch, J. Foerster, and M. Pendergrass, "Channel models for ultrawideband personal area networks," *IEEE Wireless Commun. Mag.*, vol. 10, no. 6, pp. 14–21, 2003. 3, 19, 57

[9] A. Molisch, D. Cassioli, C.-C. Chong, S. Emami, A. Fort, B. Kannan, J. Karedal, J. Kunisch, H. Schantz, K. Siwiak, and M. Win, "A comprehensive standardized model for ultrawideband propagation channels," *IEEE Trans. Antennas Propag.*, vol. 54, no. 11, pp. 3151–3166, 2006. 3

[10] A. Morgan, "Ultra-wideband impulse scattering measurements," *IEEE Trans. Antennas Propag.*, vol. 42, no. 6, pp. 840–846, 1994. 3, 15

[11] R. Qiu, "A study of the ultra-wideband wireless propagation channel and optimum UWB receiver design," *IEEE J. Sel. Areas Commun.*, vol. 20, no. 9, pp. 1628–1637, 2002. 15, 16

[12] A. Muqaibel, A. Safaai-Jazi, A. Bayram, A. Attiya, and S. Riad, "Ultrawideband through-the-wall propagation," *Proc. of IEE Microwaves, Antennas and Propagation*, pp. 581–588, Dec. 2005. 3, 10, 15

[13] T. Rappaport, *Wireless communications: principles and practice*. Upper Saddle River, NJ: Prentice–Hall, second ed., 2002. 3, 4, 10, 26

[14] R. Vaughan and N. Scott, "Super-resolution of pulsed multipath channels for delay spreadcharacterization," *IEEE Trans. Commun.*, vol. 47, no. 3, pp. 343–347, 1999. 3, 10, 11, 13, 14, 15, 27

[15] K. Pahlavan, X. Li, and J. Makela, "Indoor geolocation science and technology," *IEEE Commun. Mag.*, vol. 40, no. 2, pp. 112–118, 2002. 3, 18

[16] N. Patwari, J. Ash, S. Kyperountas, I. Hero, A.O., R. Moses, and N. Correal, "Locating the nodes: cooperative localization in wireless sensor networks," *IEEE Signal Process. Mag.*, vol. 22, pp. 54–69, 2005. 4, 18

[17] J. Lee and R. Scholtz, "Ranging in a dense multipath environment using an UWB radio link," *IEEE J. Sel. Areas Commun.*, vol. 20, no. 9, pp. 1677–1683, 2002. 4, 18, 19, 42, 50, 54, 63, 65, 92, 93

[18] S. Gezici, Z. Sahinoglu, A. Molisch, H. Kobayashi, and H. Poor, "A Two-Step Time of Arrival Estimation Algorithm for Impulse Radio Ultra Wideband Systems," in *Proc. of European Signal Processing Conference (EUSIPCO)*, (Antalya, Turkey), Sept. 2005. 4, 18, 42, 91

[19] I. Guvenc and Z. Sahinoglu, "Threshold-based TOA estimation for impulse radio UWB systems," in *Proc. of IEEE International Conference on Ultra-Wideband (ICUWB)*, (Zurich, Switzerland), pp. 420–425, Sept. 2005. 4, 18, 41, 42, 56, 91

[20] C. Falsi, D. Dardari, L. Mucchi, and M. Win, "Time of Arrival Estimation for UWB Localizers in Realistic Environments," *EURASIP J. Appl. Signal Processing (Special Issue on Wireless Location Technologies and Applications)*, vol. 2006, 2006. Article ID 32082, 13 pages. 4, 19, 41, 42, 43, 44, 56, 57, 60

[21] R. Scholtz, R. Cramer, and M. Win, "Evaluation of the propagation characteristics of ultra-widebandcommunication channels," in *Proc. of IEEE Antennas and Propagation Society International Symposium (APS)*, vol. 2, pp. 626–630, June 1998. 4, 10, 12

[22] J. Proakis, *Digital communications*. New York: McGraw–Hill, fourth ed., 2001. 4, 20, 23

[23] V. Lottici, A. D'Andrea, and U. Mengali, "Channel Estimation for Ultra-Wideband Communications," *IEEE J. Sel. Areas Commun.*, vol. 20, no. 9, pp. 1638–1644, 2002. 6, 20, 22, 23, 69, 75, 79, 84, 96

[24] Z. Tian and V. Lottici, "Low-complexity ML timing acquisition for UWB communications in dense multipath channels," *IEEE Trans. Wireless Commun.*, vol. 4, no. 6, pp. 3031–3038, 2005. 6, 20, 22

[25] C. Carbonelli and U. Mengali, "Synchronization Algorithms for UWB Signals," *IEEE Trans. Commun.*, vol. 54, no. 2, pp. 329–338, 2006. 20

[26] C. Carbonelli and U. Mitra, "Clustered ML Channel Estimation for Ultra-Wideband Signals," *IEEE Trans. Wireless Commun.*, vol. 6, no. 7, pp. 2412–2416, 2007. 16, 20, 22, 23

[27] J. Kusuma, I. Maravic, and M. Vetterli, "Sampling with finite rate of innovation: channel and timing estimation for UWB and GPS," in *Proc. of IEEE ICC*, vol. 5, pp. 3540–3544, May 2003. 6, 21

[28] Y. Chao and R. Scholtz, "Ultra-wideband transmitted reference systems," *IEEE Trans. Veh. Technol.*, vol. 54, no. 5, pp. 1556–1569, 2005. 6, 21

[29] C. Carbonelli and U. Mengali, "M-PPM noncoherent receivers for UWB applications," *IEEE Trans. Wireless Commun.*, vol. 5, no. 8, pp. 2285–2294, 2006. 21

[30] W. Cao, A. Nallanathan, and C. Chai, "Performance Analysis of Prerake DS UWB Multiple Access System Under Imperfect Channel Estimation," *IEEE Trans. Wireless Commun.*, vol. 6, no. 11, pp. 3892–3896, 2007. 6, 21, 23

[31] X. Dong, L. Jin, and P. Orlik, "A New Transmitted Reference Pulse Cluster System for UWB Communications," *IEEE Trans. Veh. Technol.*, vol. 57, no. 5, pp. 3217–3224, 2008. 6, 21

[32] M. Chung and R. Scholtz, "Comparison of transmitted-and stored-reference systems for ultra-wideband communications," in *Proc. of IEEE Military Communication Conference (MILCOM)*, pp. 521–527, Nov. 2004. 6, 21

[33] L. Yang and G. Giannakis, "Analog space-time coding for multiantenna ultra-wideband transmissions," *IEEE Trans. Commun.*, vol. 52, no. 3, pp. 507–517, 2004. 6, 21

[34] A. Fort, C. Desset, P. Wambacq, and L. Van Biesen, "Body area UWB RAKE receiver communication," in *Proc. of IEEE International Conference on Communications (ICC)*, vol. 10, pp. 4682–4687, June 2006. 6, 21

[35] Y. Chen, J. Teo, J. Lai, E. Gunawan, K. Low, C. Soh, and P. Rapajic, "Cooperative Communications in Ultra-Wideband Wireless Body Area Networks: Channel Modeling and System Diversity Analysis," *IEEE J. Sel. Areas Commun.*, vol. 27, no. 1, pp. 5–16, 2009. 6, 10, 21

[36] Y. Qi, H. Kobayashi, and H. Suda, "On time-of-arrival positioning in a multipath environment," *IEEE Trans. Veh. Technol.*, vol. 55, no. 5, pp. 1516–1526, 2006. 6, 20

[37] "Part 15.4: wireless medium access control (mac) and physical layer (phy) specifications for low-rate wireless personal area networks (wpans), amendment 1: add alternate phys," Tech. Rep. 802.15.4a-2007, IEEE std, Aug. 2007. 7

[38] S. Yano, "Investigating the ultra-wideband indoor wireless channel," in *Proc. of*

IEEE Vehicular Technology Conference (VTC), vol. 3, pp. 1200–1204, May 2002. 10, 11, 12, 13, 29

[39] A. Muqaibel, A. Safaai-Jazi, B. Woerner, and S. Riad, "UWB channel impulse response characterization using deconvolution techniques," in *Proc. of IEEE Midwest Symposium on Circuits and Systems*, vol. 45, pp. III – 605–8, Aug. 2002. 14, 25, 31, 32, 33, 34

[40] P. Richardson, W. Xiang, and W. Stark, "Modeling of ultra-wideband channels within vehicles," *IEEE J. Sel. Areas Commun.*, vol. 24, no. 4, pp. 906–912, 2006. 13

[41] B. Donlan, D. McKinstry, and R. Buehrer, "The UWB indoor channel: large and small scale modeling," *IEEE Trans. Wireless Commun.*, vol. 5, no. 10, pp. 2863–2873, 2006. 11, 13, 15

[42] Z. Irahhauten, G. Janssen, H. Nikookar, A. Yarovoy, and L. Ligthart, "UWB channel measurements and results for office and industrial environments," in *Proc. of IEEE International Conference on Ultra-Wideband (ICUWB)*, pp. 225–230, Sept. 2006. 10, 13

[43] R. Cramer, R. Scholtz, and M. Win, "Evaluation of an ultra-wide-band propagation channel," *IEEE Trans. Antennas Propag.*, vol. 50, no. 5, pp. 561–570, 2002. 12, 27

[44] S. Chang and R. Scholtz, "Polarization measurements in a UWB multipath channel," in *Proc. of IEEE Military Communication Conference (MILCOM)*, vol. 1, pp. 192–196, Oct. 2005. 13

[45] K. Heidary, "A physical scattering model for the ultra-wideband (UWB) prop-

agation channel," in *Proc. of IEEE Antennas and Propagation Society International Symposium (APS)*, vol. 1, pp. 682–685, July 2005. 12

[46] W. Yang and Z. Naitong, "A new multi-template CLEAN algorithm for UWB channel impulse response characterization," in *Proc. of International Conference on Communication Technology*, pp. 1–4, Nov. 2006. 10, 12, 14, 32, 33, 34

[47] C. Buccella, M. Feliziani, and G. Manzi, "Detection and localization of defects in shielded cables by time-domain measurements with UWB pulse injection and clean algorithm postprocessing," *IEEE Trans. Electromagn. Compat.*, vol. 46, no. 4, pp. 597–605, 2004. 10, 13

[48] Y. Chen, E. Gunawan, Y. Kim, K. Low, and C. Soh, "UWB microwave imaging for breast cancer detection: Tumor/clutter identification using a time of arrival data fusion method," in *Proc. of IEEE Antennas and Propagation Society International Symposium (APS)*, pp. 255–258, July 2006. 10

[49] H. Van Trees, *Detection, Estimation, and Modulation Theory. Part I.* New York: John Wiley & Sons, 1968. 17, 69, 73, 76, 79, 97

[50] S. Kay, *Fundamentals of Statistical Signal Processing: Estimation Theory.* Upper Saddle River, NJ: Prentice–Hall, first ed., 1993. 17, 69, 76, 79, 97

[51] R. Balakrishnan, T. Gyawali, and H. Kwon, "An inverse problem based approach for channel parameters estimation in UWB systems," in *Proc. of IEEE Vehicular Technology Conference (VTC)*, vol. 2, (Milan, Italy), pp. 1073–1077, May 2004. 19, 42, 43, 47

[52] A. Molisch, "Ultrawideband propagation channels-theory, measurement, and modeling," *IEEE Trans. Veh. Technol.*, vol. 54, no. 5, pp. 1528–1545, 2005. 19, 45

[53] Z. Low, J. Cheong, C. Law, W. Ng, and Y. Lee, "Pulse detection algorithm for line-of-sight (LOS) UWB ranging applications," *IEEE Antennas Wireless Propag. Lett.*, vol. 4, pp. 63–67, 2005. 19, 42

[54] E. Candes, J. Romberg, and T. Tao, "Robust uncertainty principles: exact signal reconstruction from highly incomplete frequency information," *IEEE Trans. Inf. Theory*, vol. 52, no. 2, pp. 489–509, 2006. 21

[55] M. Davenport, M. Wakin, and R. Baraniuk, "Detection and estimation with compressive measurements," tech. rep., Dept. of ECE, Rice University, 2006. 21, 71, 72, 74, 75

[56] Z. Wang, G. Arce, B. Sadler, J. Paredes, and X. Ma, "Compressed Detection for Pilot Assisted Ultra-Wideband Impulse Radio," in *Proc. of IEEE ICUWB*, pp. 393–398, Sept. 2007. 21, 71

[57] J. Paredes, G. Arce, and Z. Wang, "Ultra-Wideband Compressed Sensing: Channel Estimation," *IEEE J. Sel. Topics Signal Process.*, vol. 1, no. 3, pp. 383–395, 2007. 21, 76

[58] D. Donoho and J. Johnstone, "Ideal spatial adaptation by wavelet shrinkage," *Biometrika*, vol. 81, no. 3, pp. 425–455, 1994. 40, 45, 47

[59] P. Ching, H. So, and S. Wu, "On wavelet denoising and its applications to time delay estimation," *IEEE Trans. Signal Process.*, vol. 47, no. 10, pp. 2879–2882, 1999. 40, 47

[60] R. Sathish and G. Anand, "Wavelet Denoising for Plane Wave DOA Estimation By MUSIC," in *Proc. of IEEE TENCON '03*, vol. 1, (Bangalore, India), pp. 104–108, Oct. 2003. 40, 57

[61] Y. Xue, J. Wang, and Z. Liu, "Application of Wavelet Array Denoising to ESPRIT Algorithm," in *Proc. of IEEE TENCON '05*, (Melbourne, Australia), pp. 1–4, Nov. 2005. 40

[62] B. Vidakovic, "Wavelets and Bayesian statistics," *Interface '94*, pp. 15–18, June 1994. 40, 47

[63] D. Donoho, "Denoising by soft-thresholding," *IEEE Trans. Inf. Theory*, vol. 41, no. 3, pp. 613–627, 1995. 41, 47, 48

[64] A. Tikhonov and V. Arsenin, *Solutions of ill-posed problems*. New York: John Wiley & Sons, 1977. 44

[65] G. Golub, M. Heath, and G. Wahba, "Generalized cross-validation as a method for choosing a good ridge parameter," *Technometrics*, vol. 21, no. 2, pp. 215–223, 1979. 49

[66] K. Miller, "Least squares methods for ill-posed problems with a prescribed bound," *SIAM J. Math. Anal.*, vol. 1, pp. 52–74, Feb. 1970. 49

[67] S. Kay, *Fundamentals of Statistical Signal Processing: Detection Theory*. Upper Saddle River, NJ: Prentice–Hall, 1998. 50, 55

[68] A. Papoulis, *Probability, random variables, and stochastic processes*. New York: McGraw–Hill, 1991. 52

[69] S. Sanchez, N. Prelcic, and S. Galan, "Uvi_Wave," *Grupo de Teoria de la Senal, Universidad de Vigo*, 1996. 57

[70] G. Golub and C. Van Loan, *Matrix computations*. The Johns Hopkins University Press, third ed., 1996. 65

[71] M. Vetterli and J. Kovačević, *Wavelets and subband coding*. Englewood Cliffs, NJ: Prentice–Hall, 1995. 65

[72] L. Huang and C. Ko, "Performance of maximum-likelihood channel estimator for UWB communications," *IEEE Commun. Lett.*, vol. 8, no. 6, pp. 356–358, 2004. 77, 79, 95, 97

[73] L. Ma, A. Duel-Hallen, and H. Hallen, "Physical modeling and template design for UWB channels with per-path distortion," in *Proc. of IEEE Military Communication Conference (MILCOM)*, (Orlando, Florida), pp. 1–7, Oct. 2007. 90

[74] R. Wilson and R. Scholtz, "Template estimation in ultra-wideband radio," in *Proc. of Asilomar Conference on Signals, Systems, and Computers (ACSSC)*, vol. 2, (Monterey, California), pp. 1244–1248, Nov. 2003. 90